离子阱系统中量子门与量子算法的实现

（申请清华大学理学博士学位论文）

培养单位：交叉信息研究院
学　　科：物理学
研 究 生：张宽
指导教师：金奇奂副教授

二〇一八年十二月

Implementing Quantum Gates and Quantum Algorithms in a Trapped-Ion System

Thesis Submitted to
Tsinghua University
in partial fulfillment of the requirement
for the professional degree of
Doctor of Philosophy

by

Zhang Kuan
(Physics)

Thesis Supervisor : Associate Professor Kim Kihwan

December, 2018

关于学位论文使用授权的说明

本人完全了解清华大学有关保留、使用学位论文的规定，即：

清华大学拥有在著作权法规定范围内学位论文的使用权，其中包括：（1）已获学位的研究生必须按学校规定提交学位论文，学校可以采用影印、缩印或其他复制手段保存研究生上交的学位论文；（2）为教学和科研目的，学校可以将公开的学位论文作为资料在图书馆、资料室等场所供校内师生阅读，或在校园网上供校内师生浏览部分内容。

本人保证遵守上述规定。

（保密的论文在解密后应遵守此规定）

作者签名：______________　　　导师签名：______________

日　　期：______________　　　日　　期：______________

摘　要

条条大路通量子计算机，有的路已经堵了，有的路还在修。离子阱作为历史悠久的一条，无疑有着巨大潜力。离子阱系统用电场将离子囚禁在阱中，用离子能级编码量子比特，有着相对长的 T_1 和 T_2。离子阱系统还能以高保真度制备初态和测量末态。然而对所有的量子计算机备选方案来说，最难实现的还是通用的幺正操作，尤其是多量子比特门。

在我们的离子阱系统中，我们在实现量子门与量子算法方面展开了一系列工作。在“万向非门对经典和量子关联的操作效果”的项目中，我们实现了万向非门，并从理论和实验上探究了万向非门对两量子比特间的经典关联和量子关联的影响。在“模块化 DQC1 在离子阱系统中的实现”的项目中，我们实现了受控于离子比特的声子比特交换门，并用此实现了模块化 DQC1 算法。在“通过玻色子交换的费米子-反费米子散射在离子阱系统中的实验量子模拟”的项目中，我们进一步开发声子的潜力，并对一个量子场论模型实现了量子模拟（模拟门）。在“通过离子链中的多个横向模式纠缠离子”的项目中，我们实现了真正意义上的多量子比特门（用离子编码量子比特），并用它纠缠了多个离子。

为了服务于量子门与量子算法的实现，我们用 Mathematica 编写了一整套软件。它可以对量子门进行代数计算和数值模拟，并在实验上实现它。通过对各个量子门的模块化调用，软件能计算、模拟或实现量子算法。

关键词：量子计算；离子阱；量子门；量子算法；量子模拟

Abstract

All roads lead to quantum computers, some roads have been blocked, and others are still being constructed. As a long-established scheme, the trapped-ion system undoubtedly has great potential. The trapped-ion system traps ions by an electric field, encodes each qubit into the energy levels of each ion, and possesses relatively long T_1 and T_2. The trapped-ion system also prepares initial state and measures final state with high fidelity. For all alternative schemes of quantum computers, the hardest part is the implementation of universal unitary operations, especially multi-qubit gates.

In our trapped-ion system, we have been working on a series of projects for implementing quantum gates and quantum algorithms. In project of "operational effects of the UNOT gate on classical and quantum correlations", we realize the universal NOT gate, and explore the effects of universal NOT gate on classical and quantum correlations between two qubits theoretically and experimentally. In project of "implementation of modular DQC1 in a trapped-ion system", we realize a controlled-SWAP gate that swaps 2 phonon qubits controlled by a ion qubit, and use it to implement the modular DQC1 algorithm. In project of "experimental quantum simulation of fermion-antifermion scattering via boson exchange in a trapped ion", we further explore the potential of phonons, and conduct quantum simulation of a quantum field model (analog gate). In project of "entangling ions through multiple transverse modes in an ion-chain", we implement a genuine multi-qubit gate (each qubit is encoded in each ion), and use it to entangle multiple ions.

To serve the implementation of quantum gates and quantum algorithms, we have developed softwares in Mathematica. They can perform algebraic calculation and numerical simulation for a quantum gate, and implement it experimentally. By invoking each quantum gate modularly, the softwares can calculate, simulate, or implement quantum algorithms.

Key words: quantum computation; trapped-ion system; quantum gate; quantum algorithm; quantum simulation

目 录

第 1 章 Introduction 1

1.1 Quantum computation 1

1.1.1 Qubits and quantum gates 1

1.1.2 Quantum parallelism and quantum algorithms 2

1.2 Trapped $^{171}\mathrm{Yb}^{+}$ system 3

1.2.1 Robustness 4

1.2.2 Initialization 4

1.2.3 Measurement 5

1.2.4 Gate 5

1.3 Thesis structure 6

第 2 章 Physics in trapped ions 7

2.1 Ionization 7

2.2 Ion trap 7

2.2.1 Radio frequency (RF) trap 7

2.2.2 Quantum dynamics of ion-chain 8

2.3 Magnetic coupling 9

2.3.1 Zeeman effect 9

2.3.2 Microwave operations 11

2.4 Electric coupling 12

2.4.1 Detection 14

2.4.2 Doppler cooling 15

2.4.3 Optical pumping 17

2.5 Re-pumping 17

2.6 Raman transition 17

2.6.1 Polarization and Rabi frequency 18

2.6.2 Single-ion Raman operations 18

2.6.3 Sideband cooling 20

2.7 Optics 22

2.7.1 Gaussian beam 22

2.7.2 ABCD rule 23

第 3 章 Softwares in Mathematica 25
3.0.1 Quantum system 28
3.1 Module for theory 30
3.1.1 Transition and theoretical Hamiltonian 30
3.1.2 Definition and theoretical operation 31
3.2 Module for simulation 32
3.2.1 Field and interaction Hamiltonian 32
3.2.2 Waves and simulative operation 33
3.2.3 Initialization and reorganization of parameters 35
3.3 Module for experiment 36
3.3.1 Signals 36
3.3.2 Experimental control 37
3.3.3 Data collection 38
3.4 Module for data analysis 39
3.4.1 Data processing 39
3.4.2 Data fitting 41
第 4 章 Operational consequences of the UNOT gate 42
4.1 Introduction 42
4.2 Theory 44
4.2.1 Technical framework 44
4.2.2 Theoretical results 45
4.3 Experiment 46
4.3.1 Protocol 46
4.3.2 Experimental methods 47
4.3.3 Experimental results 53
4.4 Discussion 55
4.5 Conclusion 56
第 5 章 Implementation of modular DQC1 in a trapped ion system 58
5.1 Introduction 58
5.2 Results 60
5.2.1 Framework 60
5.2.2 Implementation 61
5.2.3 Performance of CSWAP gate 72

5.2.4 Experimental Benchmarks 76

5.3 Discussion 77

第 6 章 Quantum simulation of fermion-antifermion scattering via boson exchange 79

6.1 Introduction 79

6.2 Results 80

6.2.1 Hamiltonian for quantum simulation of quantum field theory 80

6.2.2 Trapped ion implementation 83

6.2.3 Experimental procedure of the quantum simulation 86

6.2.4 Self-interaction and particle creation and annihilation 87

6.3 Discussion 89

6.4 Methods 90

6.4.1 Uniform red sideband 90

6.4.2 Displacement strength adjustment 91

6.4.3 Fermionic state measurement 91

6.4.4 Average boson number measurement 92

6.4.5 Ideal theoretical calculations 92

6.4.6 Feynman diagram calculation 93

第 7 章 Entangling Ions through Multiple Transverse Modes in an Ion-Chain 95

7.1 Introduction 95

7.1.1 Mølmer-Sørensen (MS) gate 96

7.1.2 5-segment Ising (XX) gate 99

7.2 Methods 100

7.3 Results 101

7.4 Discussion and Conclusion 103

第 8 章 Conclusion 104

插图索引 105

表格索引 113

公式索引 115

参考文献 122

致 谢 129

声 明 130

附录 A　Hardwares of a trapped ion system 131
A.1　Vacuum system........ 131
A.2　Oven current supply system 132
A.3　Radio frequency (RF) system 132
A.3.1　Helical resonator........ 132
A.3.2　Radial trap frequency lock 132
A.4　High voltage system 132
A.5　Magnetic system 133
A.6　399 nm laser system........ 133
A.7　370 nm laser system........ 133
A.8　739 nm laser system........ 134
A.8.1　739 nm laser frequency cavity lock 134
A.8.2　739 nm laser frequency iodine lock........ 134
A.9　935 nm laser system........ 135
A.10　Imaging system 135
A.11　Horn system........ 135
A.12　Raman system........ 136
A.12.1　Raman laser repetition rate lock........ 136
A.13　Individual addressing system........ 137
A.14　Control system 138
个人简历、在学期间发表的学术论文与研究成果 139

第 1 章　Introduction

1.1　Quantum computation

From 1925, when the first field-effect transistor was invented, the density of transistors in IC chips, as well as the computational power of electronic devices, has been improving rapidly. According to the Moore's Law, this density and computational power double approximately every 18 month, when the prices of IC chips and electronic devices are the same. However, in spite of the high density of transistors and the great computational power, the circuits in today's computers still function classically. As the density of transistors becomes higher, quantum mechanics start to take effect, which prevents a circuit from functioning correctly. That indicates, there is an upper limit for the density of transistors and computational power of a classical computer. What's more? In face of NP problems, such as factorization, a classical computer shows a lack of ability.

1.1.1　Qubits and quantum gates

Then the concept of quantum computation was introduced[1]. The basic unit of data for a quantum computer is called qubit, which was named after its classical counterpart. Different from classical bit, a qubit can presents a linear superposition of base states $|0\rangle$ and $|1\rangle$, denoted as

$$|\psi_1\rangle = \alpha\,|0\rangle + \beta\,|1\rangle, \tag{1-1}$$

where α and β are complex numbers, which satisfies $|\alpha|^2 + |\beta|^2 = 1$. A multi-qubit system can also be in a superposition state. For example, a 2-qubit state

$$|\psi_2\rangle = \alpha_{00}\,|00\rangle + \alpha_{01}\,|01\rangle + \alpha_{10}\,|10\rangle + \alpha_{11}\,|11\rangle\,. \tag{1-2}$$

In an other word, quantum memory which consists of qubits, has much larger degrees of freedom than that of classical memory of same width.

Corresponding to classical logical gate, a unitary operation on a quantum system is called a quantum gate. A quantum gate applied on a N-qubit system is usually represented by a $2^N \times 2^N$ unitary matrix. For example, a 1-qubit NOT gate, which is the quantum analog of a classical NOT gate ($A \longrightarrow A \oplus 1$), is represented by a 2×2 unitary matrix

$$X = \begin{pmatrix} 0 & 1 \\ 1 & 0 \end{pmatrix}. \tag{1-3}$$

For an input $|\psi\rangle = \alpha |0\rangle + \beta |1\rangle$, the output of X is

$$X |\psi\rangle = \begin{pmatrix} 0 & 1 \\ 1 & 0 \end{pmatrix} \begin{pmatrix} \alpha \\ \beta \end{pmatrix} = \begin{pmatrix} \beta \\ \alpha \end{pmatrix} = \beta |0\rangle + \alpha |1\rangle . \tag{1-4}$$

Unlike some classical gates, a quantum gate never suffers from loss of information. For example, any output of a 2-qubit CNOT (controlled-NOT) gate

$$\begin{pmatrix} 1 & 0 & 0 & 0 \\ 0 & 1 & 0 & 0 \\ 0 & 0 & 0 & 1 \\ 0 & 0 & 1 & 0 \end{pmatrix} \tag{1-5}$$

can be restored to the input by applying CNOT again. However, its classical analog, a classical XOR gate ($A, B \longrightarrow A \oplus B$) is irreversible.

1.1.2 Quantum parallelism and quantum algorithms

The quantum analog of a classical integrated circuit is a quantum circuit, which consists of qubits and quantum gates. Since a qubit can stay in a classical state $|0\rangle$ or $|1\rangle$, and any classical gate can be represented by a quantum gate, a quantum circuit can simulate any classical circuit. In addition, the superposition states of a quantum system create a new property – quantum parallelism[2].

Consider a function $f(x)$ with 2^N possible inputs $x = 0, 1, \cdots, 2^N - 1$ and 2^M possible outputs $f(x) = 0, 1, \cdots, 2^M - 1$. To implement this function on a quantum circuit, $N + M$ qubits are employed – N qubits for x and M qubits for $f(x)$. A quantum gate U_f, which realizes $|x, 0\rangle \longrightarrow |x, f(x)\rangle$, is also employed in the quantum circuit. Quantum parallelism explores the possibility of inputing the superposition of base states

$$|\psi_{\text{in}}\rangle = \left(\bigotimes_{i=0}^{m-1} \frac{|0\rangle + |1\rangle}{\sqrt{2}} \right) \otimes \left(\bigotimes_{j=0}^{n-1} |0\rangle \right) = \frac{1}{\sqrt{2^N}} \sum_{x=0}^{2^N - 1} |x, 0\rangle . \tag{1-6}$$

After applying U_f, the resulting output is

$$|\psi_{\text{out}}\rangle = \frac{1}{\sqrt{2^N}} \sum_{x=0}^{2^m-1} |x, f(x)\rangle \,. \tag{1-7}$$

The quantum circuit thus reads all the information of U_f on $|\psi_{\text{out}}\rangle$ by single operation, while a classical circuit can only read $f(x)$ one by one. By properly extracting informations from $|\psi_{\text{out}}\rangle$, we are able to obtain some general informations about $f(x)$, instead of a single value of $f(x)$.

With the advantage of quantum parallelism, a quantum circuit can implement some new algorithms that are impossible for a classical circuit. Here we give the examples of Grover search algorithm[3] and Shor algorithm[4].

In Grover search algorithm ($M = 1$), $f(x) = 1$ indicates that x is the target we are searching, and $f(x) = 0$ indicates otherwise. By some fancy operations, Grover search algorithm magnifies the amplitude of components $|x, f(x) = 1\rangle$ from $|\psi_{\text{out}}\rangle$. Therefore, the targets we are searching for naturely appear. The time cost of Grover search algorithm is $O(\sqrt{N})$, which is more efficient than $O(N)$ of a classical algorithm.

The Shor algorithm factorizes a exponentially large number. On classical computer, the factorization problem is a complete NP problem. Base on the difficulty of a classical computer to solve factorization problem, the classical public key sryptosystem is established. In 1995, Peter Shor proposes a quantum factorization algorithm, which combines the quantum Fourier transformation and quantum phase estimation. Its time cost is only $O(N^3)$, while classical algorithm requires exponential time. If someone realizes a quantum computer, on which Shor algorithm can be implemented, classical public key sryptosystem will become vulnerable.

In conclusion, a quantum computer can theoretically break the limit of computing power of any classical computer. Its appearance will inevitably subvert classical information-processing methods.

1.2 Trapped $^{171}\text{Yb}^+$ system

While the theorists describe a promising prospect for quantum computers, our experimenters know the difficulties of implementing a quantum computer. A random quantum system can not possess the power of quantum computing automatically. To become a quantum computer, a quantum system must fulfill the requirements described in the following subsections[5].

There are several approaches, such as photonic system, NV center in diamond, superconducting system, neutral atom system and trapped-ion system. The scheme we are using in our lab is trapped-ion system[6–8]. Ions trapped by electric field are encoded into qubits in this approach.

1.2.1 Robustness

To implement a quantum computer, a quantum system must be able to represent quantum information robustly. It is suggested that, the number of base states of the quantum system is finite. For example, a one-dimension position state $|x\rangle$ is a bad representation of quantum information. Although it generates a Hilbert Space of infinite dimension, it is hard to precisely access $|x\rangle$, due to the limited resolution. Usually, we choose a quantum sytem consists of qubits.

The long life-time a quantum state also need to be ensured. For a qubit, the life-time of $|0\rangle$ or $|1\rangle$ is called T_1, and the life-time of $(|0\rangle + |1\rangle)/\sqrt{2}$ is called T_2. Although a classical bit possesses infinite T_1, its T_2 is almost 0, due to its strong interaction with environment. That's why a macroscopic system can't represent quantum information. A quantum system must be well isolated from the environment to ensure its long T_2.

We use trapped $^{171}\mathrm{Yb}^+$ ions to represent quantum information. A qubit is encoded in the clock states $|0\rangle = |F = 0, m_\mathrm{F} = 0\rangle$ and $|1\rangle = |F = 1, m_\mathrm{F} = 0\rangle$ of $^2S_{1/2}$ manifold. They are separated by a transition frequency of $(2\pi)(12642.812\,\mathrm{MHz} + 310.8(B/\mathrm{Gauss})^2\mathrm{Hz})$, which is first-order insensitive to the magnetic field (see 2.3.1), and leads to a relatively long T_2. At some circumstance, Zeeman states $|F = 1, m_\mathrm{F} = -1\rangle$ and $|F = 1, m_\mathrm{F} = 1\rangle$ are also used. They are separated from $|0\rangle = |F = 0, m_\mathrm{F} = 0\rangle$ by transition frequencies of $(2\pi)(12642.812\,\mathrm{MHz} \pm 1.4(B/\mathrm{Gauss})\mathrm{MHz})$, which are first-order sensitive to the magnetic field (see 2.3.1), and lead to much shorter coherence times.

1.2.2 Initialization

In quantum computation, each qubit is required to be initialized into $|0\rangle$ state before any operations. The initialization process is equivalent to the deletion operation in classical computer. It is a process of resetting the entropy of system to 0.

The initialization of $^{171}\mathrm{Yb}^+$ ions is achieved by optical pumping operation (see 2.4.3). At some circumstance, the vibrational modes are also required to be initialized. This is achieved by sideband cooling operation (see 2.6.3).

1.2.3 Measurement

Unlike classical measurement, quantum measurement generally can't extract full information from a quantum state. Consider a quantum system in superposition state $\sum_n \alpha_n |n\rangle$, and a probe in state $|0\rangle$. A simplest quantum measurement realizes

$$\sum_n \alpha_n |n, 0\rangle \to \sum_n \alpha_n |n, n\rangle . \tag{1-8}$$

After measurement, state $\sum_n \alpha_n |n, n\rangle$ quickly decoheres into a mixed state

$$\sum_n |\alpha_n|^2 |n, n\rangle \langle n, n| , \tag{1-9}$$

due to the classical nature of probe. One then can obtain the outcome n from probe with a possibility of $|\alpha_n|^2$. A quantum measurement is an irreversible process, in which the entropy increases.

The measurement of $^{171}\mathrm{Yb}^+$ ions is achieved by detection operation (see 2.4.1).

1.2.4 Gate

The implementation of universal unitary operations is the most difficult part. It is theoretically proved that any multi-qubit gate can be decomposed into single-qubit gates and CNOT gates (see Eq. 1-5). In fact, some systems, such as superconducting and trapped-ion systems, have already realized universal single-qubit gates and CNOT gate. None of them, however, implements a quantum computer that is more powerful than classical computers. This is due to the infidelity of each gate. As the quantum circuit becomes more and more complex, the infidelity accumulates. To minimize this infidelity, the operation time of a quantum circuit should be considerably shorter than $T_2/\sqrt{N}$.

In trapped $^{171}\mathrm{Yb}^+$ system, arbitrary single-qubit gate between $|0\rangle = |F = 0, m_\mathrm{F} = 0\rangle$ and $|1\rangle = |F = 1, m_\mathrm{F} = 0\rangle$ is realized by microwave operation (see 2.3.2) or Raman operation (see 2.6.2). Ions are entangled through their shared vibrational modes. Therefore, a multi-qubit gate can be realized.

1.3 Thesis structure

In chapter 2, I introduce some physics necessary for a trapped-ion system (or a specific trapped $^{171}\mathrm{Yb}^{+}$ system).

In chapter 3, I illustrate the main structure of the softwares that I develop, which assist quantum computation by carring out algebraic calculation, numerical simulation, real-time experiment and data analysis.

In chapter 4, I explain the project "operational effects of the UNOT gate on classical and quantum correlations". This work is mainly accomplished by me, and has been published in Science Bulletin[9].

In chapter 5, I explain the project "implementation of modular DQC1 in a trapped ion system". This work is mainly accomplished by me.

In chapter 6, I explain the project "experimental quantum simulation of fermion-antifermion scattering via boson exchange in a trapped ion". This work is mainly accomplished by Xiang Zhang and myself, and has been published in Nature Communications[10].

In chapter 7, I explain the project "entangling ions through multiple transverse modes in an ion-chain". This work is completed in stages, mainly by Yao Lu, Shuaining Zhang and myself.

In chapter 8, I summarize my works.

第 2 章　Physics in trapped ions

2.1　Ionization

We ionize a neutral ^{171}Yb atom into an ^{171}Yb^{+} ion by 2 steps. First, a 398.91 nm laser excites the ^{171}Yb atom from ^{1}S$_{0}$ manifold to ^{1}P$_{1}$ manifold. Then, another 369.53 nm laser promotes the outermost electron to the continuum.

2.2　Ion trap

The trapped-ion system uses ions as qubits to implement quantum computation. To trap each ion in a static position, an external electric field is employed. This is actually a trick task, considering the fact that an electrostatic field can not generate minimum potential points. Generally, we use 2 parts of electric field. One is a rotating radio frequency field, which is theoretically isotropic along one direction (z-axis). Averaging over time, this radio frequency field forms a pseudopotential, which traps all ions tightly on z-axis. Another part is an electrostatic field. It counteracts the Coulomb force, and pushes each ion to its minimum potential point. Eventually, an ion-chain forms along z-axis. Each ion vibrates around its equilibrium position with a relatively small energy, which is quantized into phonons.

2.2.1　Radio frequency (RF) trap

Around z-axis, the potential of rotating RF field is

$$\Phi = \frac{\Phi_0}{2r_0^2}(x^2 - y^2), \tag{2-1}$$

where $\Phi_0 = U + V\cos\omega t$ varis slowly ($\omega r_0 \ll c$) over time t. Each ion in potential Φ satisfies

$$\begin{cases} \dfrac{d^2x}{d\tau^2} + (a + 2q\cos 2\tau)x &= 0 \\ \dfrac{d^2y}{d\tau^2} - (a + 2q\cos 2\tau)z &= 0, \end{cases} \tag{2-2}$$

where

$$a = \frac{4eU}{mr_0^2\omega^2} \quad ,q = \frac{2eV}{mr_0^2\omega^2} \quad ,\tau = \frac{\omega t}{2}. \tag{2-3}$$

At certain conditions of a and q, ions can be stabilized on z-axis. In this case, the RF field forms a harmonic pseudopotential around z-axis[11].

2.2.2 Quantum dynamics of ion-chain

We consider a single-species ion-chain. For each ion, the degree of ionization is Z and the mass is M. For convenience, we define a unit distance $\sqrt[3]{Z^2e^2/(4\pi\epsilon_0 M)}$ (it is $2.73\,\mu\text{m} \times (2\pi\,\text{MHz})^{2/3}$ in $^{171}\text{Yb}^+$ case), so that x, y and z are rescaled.

Combining the pseudopotential and electrostatic potential, a general form of external electric potential is

$$V(x, y, z) = \frac{x^2}{2}V_1(z) + \frac{y^2}{2}V_2(z) + V_3(z). \tag{2-4}$$

At the equilibrium position of ion i, the external electric field and Coulomb field cancel each other

$$\frac{dV_3}{dz_i} + \sum_{j\neq i} \frac{1}{(z_j - z_i)|z_j - z_i|} = 0. \tag{2-5}$$

Therefore, each equilibrium position z_i can be solved.

Each ion vibrates around its equilibrium position. The real-time position of ion i is denoted as $(x_i, y_i, z_i + u_i)$, where x_i, y_i and u_i are small amounts relative to 1. The total potential energy of ion-chain is

$$\begin{aligned}
&\sum_i V(x_i, y_i, z_i + u_i) + \sum_{i<j} \frac{1}{\sqrt{(x_j - x_i)^2 + (y_j - y_i)^2 + (z_j - z_i + u_j - u_i)^2}} \\
\approx &\sum_i V_3(z_i) + \frac{1}{2}\sum_{i,j} x_i X_{i,j} x_j + \frac{1}{2}\sum_{i,j} y_i Y_{i,j} y_j + \frac{1}{2}\sum_{i,j} u_i Z_{i,j} u_j,
\end{aligned} \tag{2-6}$$

where

$$X_{i,i} = V_1(z_i) - \sum_{j\neq i} \frac{1}{|z_i - z_j|^3} \tag{2-7}$$

$$X_{i,j} = \frac{1}{|z_i - z_j|^3} \tag{2-8}$$

$$Y_{i,i} = V_2(z_i) - \sum_{j\neq i} \frac{1}{|z_i - z_j|^3} \tag{2-9}$$

$$Y_{i,j} = \frac{1}{|z_i - z_j|^3} \tag{2-10}$$

$$Z_{i,i} = \frac{d^2V_3}{dz_i^2} + 2\sum_{j\neq i} \frac{1}{|z_i - z_j|^3} \tag{2-11}$$

$$Z_{i,j} = -2\frac{1}{|z_i - z_j|^3} \tag{2-12}$$

The eigenvalues and eigenstates of matrix X (Y or Z) reveals the vibrational frequencies and vibrational modes in x (y or z) direction.

For the harmonic external electric potential case,

$$V_1 = \nu_x^2, \quad V_2 = \nu_y^2, \quad V_3 = \frac{1}{2}\nu_z^2 z^2, \tag{2-13}$$

where ν_x (ν_y or ν_z) is angular trap frequency in x (y or z) direction. In such case, the vibrational frequencies and vibrational modes are calculated in Ref. [12].

2.3 Magnetic coupling

2.3.1 Zeeman effect

We consider an ion with magnetic dipole moment $\vec{\mu}$ at the influence of static magnetic field $\vec{B}$ (z-direction). The interaction between ion and magnetic field is $-\vec{\mu}\cdot\vec{B} = -\mu_0^{(1)}B$, where $\mu_0^{(1)}$ is a tensor operator of rank 1 with magnetic quantum number 0. According to Wigner-Eckart theorem, we calculate each element

$$-\langle F', m_{\rm F}'|\, \mu_0^{(1)}\, |F, m_{\rm F}\rangle\, B = -\langle F, m_{\rm F}, 1, 0|F', m_{\rm F}'\rangle\langle F'\|\mu^{(1)}\|F\rangle B, \tag{2-14}$$

where $|F, m_{\rm F}\rangle$ and $|F', m_{\rm F}'\rangle$ are energy levels of ion, and $\langle F, m_{\rm F}, 1, 0|F', m_{\rm F}'\rangle$ is Clebsch-Gordan coefficient[13].

For an $^{171}\mathrm{Yb}^+$ ion, we first calculate the effect of static magnetic field on each energy level of $^2\mathrm{S}_{1/2}$ manifold

$$-\langle F=0, m_{\rm F}=0|\, \mu_0^{(1)}\, |F=0, m_{\rm F}=0\rangle\, B = 0, \tag{2-15}$$

$$-\langle F=1,m_{\mathrm{F}}=0|\,\mu_0^{(1)}\,|F=1,m_{\mathrm{F}}=0\rangle\,B=0, \tag{2-16}$$

$$-\langle F=1,m_{\mathrm{F}}=-1|\,\mu_0^{(1)}\,|F=1,m_{\mathrm{F}}=-1\rangle\,B=\frac{\langle 1\|\mu^{(1)}\|1\rangle B}{\sqrt{2}}, \tag{2-17}$$

$$-\langle F=1,m_{\mathrm{F}}=1|\,\mu_0^{(1)}\,|F=1,m_{\mathrm{F}}=1\rangle\,B=-\frac{\langle 1\|\mu^{(1)}\|1\rangle B}{\sqrt{2}}. \tag{2-18}$$

Therefore, $|F=0,m_{\mathrm{F}}=0\rangle$ and $|F=1,m_{\mathrm{F}}=0\rangle$ have no first-order Zeeman shift (see Eq. (2-15)(2-16)), while $|F=1,m_{\mathrm{F}}=-1\rangle$ and $|F=1,m_{\mathrm{F}}=1\rangle$ have (see Eq. (2-17)(2-18)). We thus call $|F=1,m_{\mathrm{F}}=-1\rangle$ and $|F=1,m_{\mathrm{F}}=1\rangle$ Zeeman levels. The amount of their first-order Zeeman shift is

$$-\frac{\langle 1\|\mu^{(1)}\|1\rangle B}{\sqrt{2}}=1.4\frac{B}{\mathrm{Gauss}}\mathrm{MHz}. \tag{2-19}$$

A static magnetic field also couples $|F=0,m_{\mathrm{F}}=0\rangle$ and $|F=1,m_{\mathrm{F}}=0\rangle$ with strength[14]

$$-\langle F=1,m_{\mathrm{F}}=0|\,\mu_0^{(1)}\,|F=0,m_{\mathrm{F}}=0\rangle\,B=-\langle 1\|\mu^{(1)}\|0\rangle B=\zeta\mu_{\mathrm{B}}B. \tag{2-20}$$

When $B=0$, these 2 levels are separated by a transition frequency of[15]

$$\frac{A}{h}=12642.812\,\mathrm{MHz}. \tag{2-21}$$

When $B\neq 0$, the magnetic coupling is described by Hamiltonian

$$\begin{pmatrix} A & \zeta\mu_{\mathrm{B}}B \\ \zeta\mu_{\mathrm{B}}B & 0 \end{pmatrix}\approx\begin{pmatrix} A+(\zeta\mu_{\mathrm{B}}B)^2/A & 0 \\ 0 & -(\zeta\mu_{\mathrm{B}}B)^2/A \end{pmatrix} \tag{2-22}$$

based by $|F=1,m_{\mathrm{F}}=0\rangle$ and $|F=0,m_{\mathrm{F}}=0\rangle$. The resulting effects are secend-order Zeeman shifts

$$\frac{(\zeta\mu_{\mathrm{B}}B)^2}{hA}=155.4(B/\mathrm{Gauss})^2\mathrm{Hz} \tag{2-23}$$

on both $|F=0,m_{\mathrm{F}}=0\rangle$ and $|F=1,m_{\mathrm{F}}=0\rangle$.

2.3.2 Microwave operations

For single $^{171}\mathrm{Yb}^{+}$ ion case, we usually use microwave to manipulate levels of $^2\mathrm{S}_{1/2}$ manifold. The differences between a microwave and static magnetic field are – a microwave is an alternating magnetic field, it is much weaker than static magnetic field, and it can take any direction instead of only z-direction. A microwave is denoted as $\{B_{-1}^{(1)}, B_0^{(1)}, B_1^{(1)}\}\cos(\omega t + \phi)$, where

$$B_{-1}^{(1)} = -\frac{B_\mathrm{x} - iB_\mathrm{y}}{\sqrt{2}}, \quad B_0^{(1)} = B_\mathrm{z}, \quad B_1^{(1)} = \frac{B_\mathrm{x} + iB_\mathrm{y}}{\sqrt{2}}. \tag{2-24}$$

The component $B_q^{(1)}$ $(q = 0, \pm 1)$ couples $|F = 0, m_\mathrm{F} = 0\rangle$ and $|F = 1, m_\mathrm{F} = q\rangle$ with strength (see Eq. (2-20))

$$-\langle F = 1, m_\mathrm{F} = q|\, \mu_q^{(1)}\, |F = 0, m_\mathrm{F} = 0\rangle\, B_q^{(1)} = -\langle 1\|\mu^{(1)}\|0\rangle B_q^{(1)} = \hbar\Omega, \tag{2-25}$$

where Ω is the Rabi frequency. When microwave frequency ω resonates with the energy difference between $|F = 0, m_\mathrm{F} = 0\rangle$ and $|F = 1, m_\mathrm{F} = q\rangle$, the Hamiltonian in Schrödinger picture is

$$\hbar \begin{pmatrix} \omega & \Omega e^{-i(\omega t+\phi)} \\ \Omega e^{i(\omega t+\phi)} & 0 \end{pmatrix} \tag{2-26}$$

based by $|F = 1, m_\mathrm{F} = q\rangle$ and $|F = 0, m_\mathrm{F} = 0\rangle$. In interaction picture ($H_0 = \hbar\omega\,|1, q\rangle\,\langle 1, q|$), the Hamiltonian is simple as

$$\hbar \begin{pmatrix} 0 & \Omega e^{-i\phi} \\ \Omega e^{i\phi} & 0 \end{pmatrix}. \tag{2-27}$$

By applying such microwave with duration d, a microwave operation

$$\exp\left[-\frac{i\chi}{2}\left(e^{-i\phi}\,|1, 0\rangle\,\langle 0, 0| + \mathrm{H.c.}\right)\right] = \begin{pmatrix} \cos\frac{\chi}{2} & -i\sin\frac{\chi}{2}e^{-i\phi} \\ -i\sin\frac{\chi}{2}e^{i\phi} & \cos\frac{\chi}{2} \end{pmatrix} \tag{2-28}$$

is implemented, where $\chi = \Omega d$.

2.4 Electric coupling

For an electrostatic field or a low-frequency electric field, a charged particle stays at its minimum potential point, where no electric field exists. An ion can only couple to a high-frequency electric field, denoted as $\{E^{(1)}_{-1}, E^{(1)}_{0}, E^{(1)}_{1}\}\cos(\omega t + \phi)$, where

$$E^{(1)}_{-1} = -\frac{E_{\mathrm{x}} - iE_{\mathrm{y}}}{\sqrt{2}}, \quad E^{(1)}_{0} = E_{\mathrm{z}}, \quad E^{(1)}_{1} = \frac{E_{\mathrm{x}} + iE_{\mathrm{y}}}{\sqrt{2}}. \tag{2-29}$$

The component $E^{(1)}_q$ $(q = 0, \pm 1)$ couples the eigenstates $|l, m_{\mathrm{L}}\rangle$ and $|l', m'_{\mathrm{L}}\rangle$ of orbital angular momentum of ion with strength

$$-e\,\langle l', m'_{\mathrm{L}}|\, r^{(1)}_q\, |l, m_{\mathrm{L}}\rangle\, E^{(1)}_q = -e\langle l, m_{\mathrm{L}}, 1, q|l', m'_{\mathrm{L}}\rangle\langle l'\|r^{(1)}\|l\rangle E^{(1)}_q, \tag{2-30}$$

where tensor operators

$$r^{(1)}_{-1} = -\frac{x - iy}{\sqrt{2}}, \quad r^{(1)}_{0} = z, \quad r^{(1)}_{1} = \frac{x + iy}{\sqrt{2}}. \tag{2-31}$$

Now we consider the angular momentum of electron $\vec{J} = \vec{L} + \vec{S}$, which consists of orbital angular momentum $\vec{L}$ and spin angular momentum $\vec{S}$. An eigenstate of $\vec{J}$ and its magnetic quantum number m_{J} is composed of

$$|l, s, j, m_{\mathrm{J}}\rangle = \sum_{m_{\mathrm{L}}+m_{\mathrm{S}}=m_{\mathrm{J}}} \langle l, m_{\mathrm{L}}, s, m_{\mathrm{S}}|j, m_{\mathrm{J}}\rangle\, |l, m_{\mathrm{L}}\rangle\, |s, m_{\mathrm{S}}\rangle\,. \tag{2-32}$$

Therefore, $E^{(1)}_q$ $(q = 0, \pm 1)$ couples $|l, s, j, m_{\mathrm{J}}\rangle$ and $|l', s, j', m'_{\mathrm{J}}\rangle$ with strength

$$\begin{aligned}
&-e\,\langle l', s, j', m'_{\mathrm{J}}|\, r^{(1)}_q\, |l, s, j, m_{\mathrm{J}}\rangle\, E^{(1)}_q \\
=&-eE^{(1)}_q \sum_{m_{\mathrm{S}}=-s}^{s} \langle l, m_{\mathrm{L}}, s, m_{\mathrm{S}}|j, m_{\mathrm{J}}\rangle\langle l', m'_{\mathrm{L}}, s, m_{\mathrm{S}}|j', m'_{\mathrm{J}}\rangle \\
&\langle l', m'_{\mathrm{L}} = m'_{\mathrm{J}} - m_{\mathrm{S}}|\, r^{(1)}_q\, |l, m_{\mathrm{L}} = m_{\mathrm{J}} - m_{\mathrm{S}}\rangle \\
=&-e\langle l'\|r^{(1)}\|l\rangle E^{(1)}_q \\
&\sum_{m_{\mathrm{S}}=-s}^{s} \langle l, m_{\mathrm{L}}, s, m_{\mathrm{S}}|j, m_{\mathrm{J}}\rangle\langle l', m'_{\mathrm{L}}, s, m_{\mathrm{S}}|j', m'_{\mathrm{J}}\rangle \\
&\langle l, m_{\mathrm{L}} = m_{\mathrm{J}} - m_{\mathrm{S}}, 1, q|l', m'_{\mathrm{L}} = m'_{\mathrm{J}} - m_{\mathrm{S}}\rangle.
\end{aligned} \tag{2-33}$$

If j and j' are determined, Eq. (2-33) has a simpler expression

$$\begin{aligned} & -e \left\langle l', s, j', m_{\mathrm{J}}' \right| r_q^{(1)} \left| l, s, j, m_{\mathrm{J}} \right\rangle E_q^{(1)} \\ = & -e\langle j, m_{\mathrm{J}}, 1, q | j', m_{\mathrm{J}}' \rangle \langle l', s, j' \| r^{(1)} \| l, s, j \rangle E_q^{(1)}. \end{aligned} \tag{2-34}$$

Finally, we consider the total angular momentum $\vec{F} = \vec{I} + \vec{J}$ of nuclear spin angular momentum $\vec{I}$ and electron angular momentum $\vec{J}$. Similar to Eq. (2-32), we have

$$|i, l, s, j, F, m_{\mathrm{F}}\rangle = \sum_{m_{\mathrm{I}}+m_{\mathrm{J}}=m_{\mathrm{F}}} \langle i, m_{\mathrm{I}}, j, m_{\mathrm{J}} | F, m_{\mathrm{F}} \rangle \left| i, m_{\mathrm{I}} \right\rangle \left| l, s, j, m_{\mathrm{J}} \right\rangle . \tag{2-35}$$

Therefore, $E_q^{(1)}$ ($q = 0, \pm 1$) couples $|i, l, s, j, F, m_{\mathrm{F}}\rangle$ and $|i, l', s, j', F', m_{\mathrm{F}}'\rangle$ with strength

$$\begin{aligned} & -e \left\langle i, l', s, j', F', m_{\mathrm{F}}' \right| r_q^{(1)} \left| i, l, s, j, F, m_{\mathrm{F}} \right\rangle E_q^{(1)} \\ = & -e\langle l' \| r^{(1)} \| l \rangle E_q^{(1)} \\ & \sum_{m_{\mathrm{I}}=-i}^{i} \langle i, m_{\mathrm{I}}, j, m_{\mathrm{J}} | F, m_{\mathrm{F}} \rangle \langle i, m_{\mathrm{I}}, j', m_{\mathrm{J}}' | F', m_{\mathrm{F}}' \rangle \\ & \sum_{m_{\mathrm{S}}=-s}^{s} \langle l, m_{\mathrm{L}}, s, m_{\mathrm{S}} | j, m_{\mathrm{J}} \rangle \langle l', m_{\mathrm{L}}', s, m_{\mathrm{S}} | j', m_{\mathrm{J}}' \rangle \\ & \langle l, m_{\mathrm{L}}, 1, q | l', m_{\mathrm{L}}' \rangle, \end{aligned} \tag{2-36}$$

where $m_{\mathrm{L}} = m_{\mathrm{J}} - m_{\mathrm{S}} = m_{\mathrm{F}} - m_{\mathrm{I}} - m_{\mathrm{S}}$ and $m_{\mathrm{L}}' = m_{\mathrm{J}}' - m_{\mathrm{S}} = m_{\mathrm{F}}' - m_{\mathrm{I}} - m_{\mathrm{S}}$. If j and j' are determined,

$$\begin{aligned} & -e \left\langle i, l', s, j', F', m_{\mathrm{F}}' \right| r_q^{(1)} \left| i, l, s, j, F, m_{\mathrm{F}} \right\rangle E_q^{(1)} \\ = & -e\langle l', s, j' \| r^{(1)} \| l, s, j \rangle E_q^{(1)} \\ & \sum_{m_{\mathrm{I}}=-i}^{i} \langle i, m_{\mathrm{I}}, j, m_{\mathrm{J}} | F, m_{\mathrm{F}} \rangle \langle i, m_{\mathrm{I}}, j', m_{\mathrm{J}}' | F', m_{\mathrm{F}}' \rangle \\ & \langle j, m_{\mathrm{J}} = m_{\mathrm{F}} - m_{\mathrm{I}}, 1, q | j', m_{\mathrm{J}}' = m_{\mathrm{F}}' - m_{\mathrm{I}} \rangle. \end{aligned} \tag{2-37}$$

If F, F', j and j' are determined,

$$\begin{aligned} & -e \left\langle i, l', s, j', F', m_{\mathrm{F}}' \right| r_q^{(1)} \left| i, l, s, j, F, m_{\mathrm{F}} \right\rangle E_q^{(1)} \\ = & -e\langle F, m_{\mathrm{F}}, 1, q | F', m_{\mathrm{F}}' \rangle \langle i, l', s, j', F' \| r^{(1)} \| i, l, s, j, F \rangle E_q^{(1)}. \end{aligned} \tag{2-38}$$

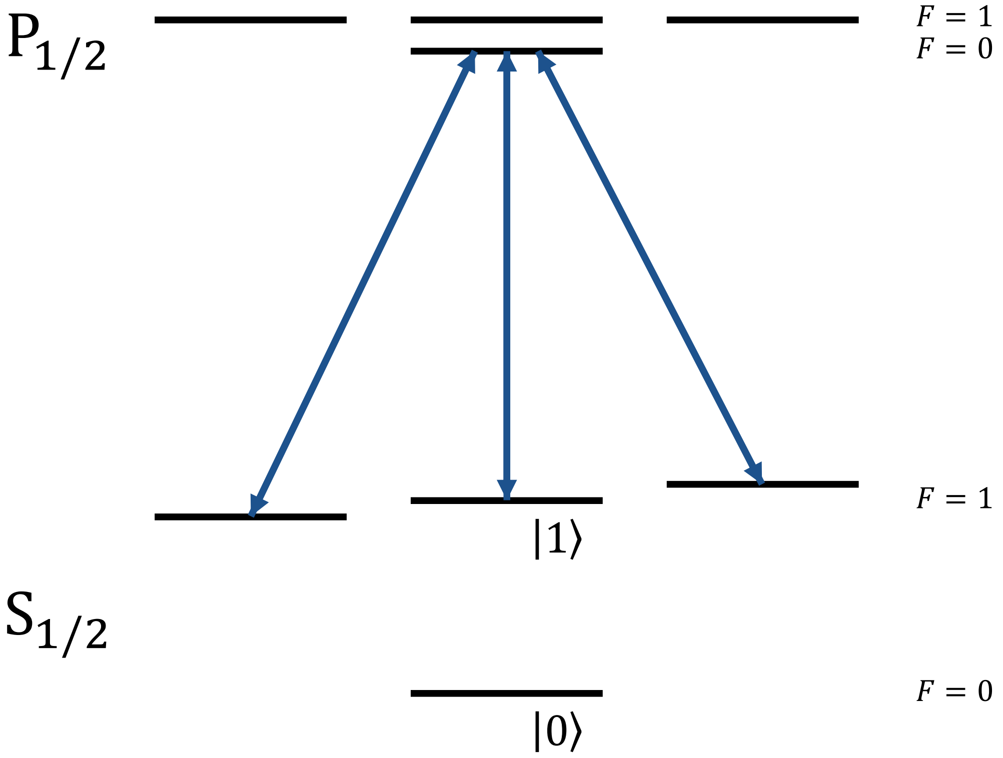

图 2.1　**Detection operation.**　A detection operation makes resonant transitions between $|F = 1, m_F = 0, \pm 1\rangle$ of $^2S_{1/2}$ manifold and $|F = 0, m_F = 0\rangle$ of $^2P_{1/2}$ manifold.

For single $^{171}Yb^+$ ion case, we use a 369.53 nm (or near) laser to couple ^2S and ^2P manifolds ($i = 1/2$, $l = 0$, $l' = 1$ and $s = 1/2$). Usually we specify in $^2S_{1/2}$ and $^2P_{1/2}$ manifolds ($j = j' = 1/2$), and use Eq. (2-37) to calculate the coupling strength ratio between energy-level pairs. For example

$$\frac{\langle l' = 1, F' = 1, m'_F = 0|\, r_0^{(1)}\, |l = 0, F = 0, m_F = 0\rangle}{\langle l' = 1, F' = 0, m'_F = 0|\, r_0^{(1)}\, |l = 0, F = 1, m_F = 0\rangle} = 1. \tag{2-39}$$

Sometimes, Rabi frequencies between $^2S_{1/2} \rightarrow ^2 P_{1/2}$ and $^2S_{1/2} \rightarrow ^2 P_{3/2}$ ($j' = 3/2$) are compared (see 2.6.1). In this case, we have to use Eq. (2-36).

2.4.1 Detection

In trapped $^{171}Yb^+$ system, a detection operation makes resonant transitions between $|F = 1, m_F = 0, \pm 1\rangle$ of $^2S_{1/2}$ manifold and $|F = 0, m_F = 0\rangle$ of $^2P_{1/2}$ manifold (see Fig. 2.1). A $^{171}Yb^+$ ion naturally stays in $^2S_{1/2}$ manifold. If $F = 1$, the detection operation drives ion to $|F=0, m_{\mathrm{F}}=0\rangle$ of ${}^2\mathrm{P}_{1/2}$ manifold and brings it back with rapid rate. During this process, the ion continuously emits photons, which can be detected by a probe. If $F=0$, the ion is shielded from detection operation and remains dark. Therefore, state $|F=0, m_{\mathrm{F}}=0\rangle$ is distinguished from $|F=1, m_{\mathrm{F}}=0,\pm1\rangle$ of ${}^2\mathrm{S}_{1/2}$ manifold.

Consider a superposition state $|\psi\rangle = \sum_{m=-1}^{1} c_m\,|F=1, m_{\mathrm{F}}=m\rangle$ of ${}^2\mathrm{S}_{1/2}$ manifold. Detection field $\{E_{-1}^{(1)}, E_0^{(1)}, E_1^{(1)}\}\cos(\omega t+\phi)$ couples $|\psi\rangle$ and $|F=0, m_{\mathrm{F}}=0\rangle$ of ${}^2\mathrm{P}_{1/2}$ manifold with strength (see Eq. (2-38))

$$\begin{aligned} &-e\sum_{m=-1}^{1}\langle l'=1, F'=0, m_{\mathrm{F}}'=0|\,r_{-m}^{(1)}\,|l=0, F=1, m_{\mathrm{F}}=m\rangle\,c_m E_{-m}^{(1)} \\ =&-e\langle l'=1, F'=0\|r^{(1)}\|l=0, F=1\rangle\sum_{m=-1}^{1}\langle 1, m, 1, -m|0, 0\rangle c_m E_{-m}^{(1)} \\ =&-e\frac{\langle l'=1, F'=0\|r^{(1)}\|l=0, F=1\rangle}{\sqrt{3}}\left(c_{-1}E_1^{(1)}-c_0E_0^{(1)}+c_1E_{-1}^{(1)}\right). \end{aligned} \tag{2-40}$$

If $c_{-1}E_1^{(1)}-c_0E_0^{(1)}+c_1E_{-1}^{(1)}=0$, detection field can not drive $|\psi\rangle$. In this case, $|\psi\rangle$ is called a dark state[16]. In the case of static magnetic field $\vec{B}=\vec{0}$, detection field eventually traps ion into dark state $|\psi\rangle$, due to the spontaneous radiations. Therefore, to keep detection operation functioning, a static magnetic field is necessary.

2.4.2 Doppler cooling

Apart from transitions between $|F=1, m_{\mathrm{F}}=0,\pm1\rangle$ of ${}^2\mathrm{S}_{1/2}$ manifold and $|F=0, m_{\mathrm{F}}=0\rangle$ of ${}^2\mathrm{P}_{1/2}$ manifold, a Doppler cooling operation also makes transitions between $|F=0, m_{\mathrm{F}}=0\rangle$ of ${}^2\mathrm{S}_{1/2}$ manifold and $|F=1, m_{\mathrm{F}}=0,\pm1\rangle$ of ${}^2\mathrm{P}_{1/2}$ manifold. This is done by adding a +14.748 GHz sideband to detection laser. If in ${}^2\mathrm{S}_{1/2}$ manifold, the ion absorbs a photon from laser. If in ${}^2\mathrm{P}_{1/2}$ manifold, the ion emits a photon in laser direction due to stimulated emission, or in random direction due to spontaneous radiation. Averaging over time, the ion absorbs momentum from laser. The frequencies of Doppler cooling laser are slightly smaller (20 MHz) than corresponding resonant frequencies. According to Doppler effect, the ion slows down when coming towards laser. As a result, the ion is eventually cooled down in electric trap. See Ref.[17] for more details about Doppler cooling.

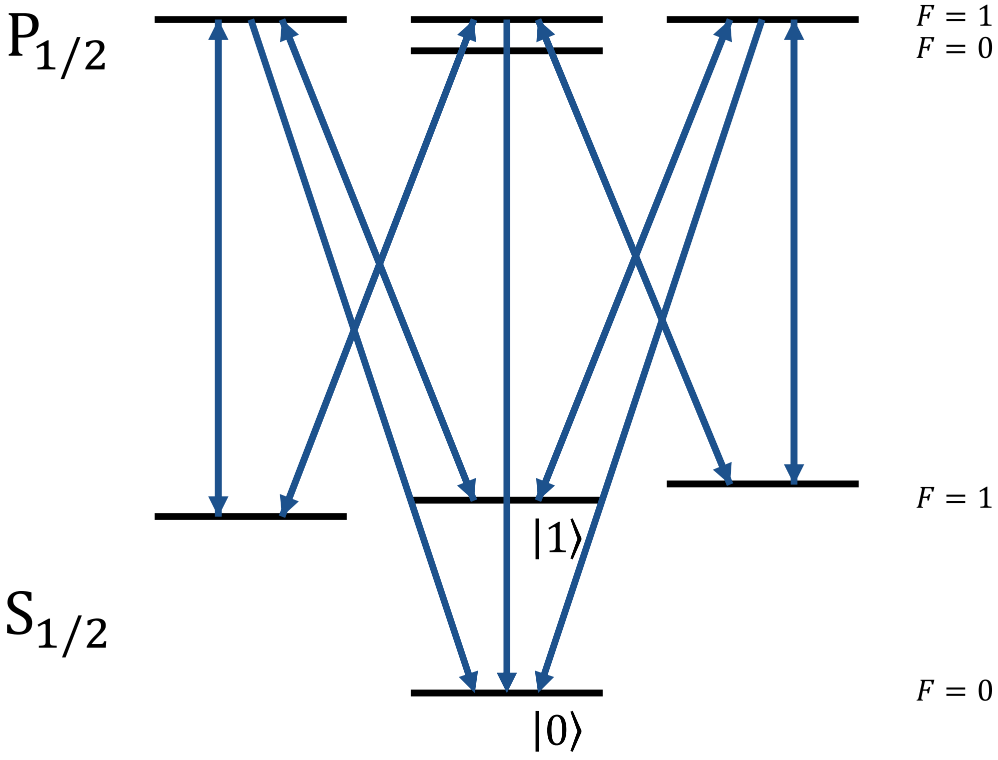

图 2.2　**Optical pumping operation.** A optical pumping operation makes resonant transitions between $|l = 0, F = 1, m_F = -1\rangle$ and $|l = 1, F = 1, m_F = -1, 0\rangle$, between $|l = 0, F = 1, m_F = 0\rangle$ and $|l = 1, F = 1, m_F = \pm 1\rangle$, and between $|l = 0, F = 1, m_F = 1\rangle$ and $|l = 1, F = 1, m_F = 0, 1\rangle$. Possible spontaneous radiations from ${}^2P_{1/2}$ manifold to ${}^2S_{1/2}$ manifold also happen during optical pumping.

2.4.3 Optical pumping

A optical pumping operation makes resonant transitions between $|F = 1, m_\mathrm{F} = 0, \pm 1\rangle$ of ${}^2\mathrm{S}_{1/2}$ manifold and $|F = 1, m_\mathrm{F} = 0, \pm 1\rangle$ of ${}^2\mathrm{P}_{1/2}$ manifold (see Fig. 2.2). This is done by adding a +2.105 GHz sideband to detection laser. Possible spontaneous radiations from ${}^2\mathrm{P}_{1/2}$ manifold to ${}^2\mathrm{S}_{1/2}$ manifold also happen during this process. If in $|F = 0, m_\mathrm{F} = 0\rangle$ of ${}^2\mathrm{S}_{1/2}$ manifold, the ion no longer transits to other states. If in any other state, the ion eventually goes to $|F = 0, m_\mathrm{F} = 0\rangle$ of ${}^2\mathrm{S}_{1/2}$ manifold. Therefore, the state of ion is initialized.

2.5 Re-pumping

To avoid the state of ${}^{171}\mathrm{Yb}^+$ being trapped in ${}^2\mathrm{D}_{3/2}$ manifold, we use a 935.2 nm laser (with a −3.07 GHz sideband) to make transition ${}^2\mathrm{D}_{3/2} \leftrightarrow^3 \mathrm{D}[3/2]_{1/2}$[18]. From ${}^3\mathrm{D}[3/2]_{1/2}$ manifold, ${}^{171}\mathrm{Yb}^+$ rapidly returns to the Doppler cooling cycle (see 2.4.2).

2.6 Raman transition

Consider a 3-level system, where the absolute energy of $|0\rangle$ ($|1\rangle$ or $|2\rangle$) is E_0 (E_1 or E_2), and 2 lasers, where the laser with angular frequency ω_0 (ω_1) couples $|0\rangle$ ($|1\rangle$) and $|2\rangle$ with Rabi frequency Ω_0 (Ω_1). The Hamiltonian of the system is

$$H = \frac{\hbar}{2}\begin{pmatrix} & & \Omega_0^* e^{i\delta_0 t} \\ & & \Omega_1^* e^{i\delta_1 t} \\ \Omega_0 e^{-i\delta_0 t} & \Omega_1 e^{-i\delta_1 t} & \end{pmatrix}, \tag{2-41}$$

where $\delta_0 = \omega_0 - (E_2 - E_0)/\hbar$ and $\delta_1 = \omega_1 - (E_2 - E_1)/\hbar$. If $|\Omega_0| \ll \delta_0 \approx \delta \approx \delta_1 \gg |\Omega_1|$, the effective Hamiltonian is[19]

$$H_\mathrm{eff} = \frac{\hbar}{2}\begin{pmatrix} \frac{|\Omega_0|^2}{2\delta_0} & \frac{\Omega_0^*\Omega_1}{2\delta} e^{i(\delta_0-\delta_1)t} & \\ \frac{\Omega_0\Omega_1^*}{2\delta} e^{i(\delta_1-\delta_0)t} & \frac{|\Omega_1|^2}{2\delta_1} & \\ & & -\frac{|\Omega_0|^2+|\Omega_1|^2}{2\delta_0} \end{pmatrix}, \tag{2-42}$$

where the diagonal parts represent AC Stark shifts on states $|0\rangle$, $|1\rangle$ and $|2\rangle$, and the off-diagonal parts indicate that the effect of these 2 lasers is a coupling between $|0\rangle$ and $|1\rangle$ with Rabi frequency $\Omega_0\Omega_1^*/(2\delta)$. This is called Raman effect.

In trapped $^{171}\mathrm{Yb}^{+}$ system, we can encode $|0\rangle$ and $|1\rangle$ to $^2\mathrm{S}$ manifold and $|2\rangle$ to $^2\mathrm{P}$ manifold, and employ 2 Raman lasers with frequencies far detuned from $^2\mathrm{S}_{1/2} \leftrightarrow ^2 \mathrm{P}_{1/2}$ and $^2\mathrm{S}_{1/2} \leftrightarrow ^2 \mathrm{P}_{3/2}$. In the condition of $|\Omega_0| \ll \delta_0 \approx \delta \approx \delta_1 \gg |\Omega_1|$, these Raman lasers are used to manipulate levels of $^2\mathrm{S}_{1/2}$ manifold. Unlike microwave (see 2.3.2), Raman lasers can couple ions to their vibrational modes (see 2.6.2). Through these vibrational modes, ions can thus be entangled.

2.6.1 Polarization and Rabi frequency

We denote 2 Raman lasers as $\{E_{-1}, E_0, E_1\}\cos\omega t$ and $\{E'_{-1}, E'_0, E'_1\}\cos\omega' t$. Levels $|F, m_\mathrm{F}\rangle$ and $|F', m'_\mathrm{F}\rangle$ of $^2\mathrm{S}_{1/2}$ manifold are coupled through $^2\mathrm{P}_{1/2}$ and $^2\mathrm{P}_{3/2}$ manifolds with strength (see Eq. (2-42))

$$\begin{aligned}
&\frac{e^2}{\hbar}\sum_{j=\frac{1}{2},\frac{3}{2}}\frac{1}{\delta_j}\sum_{F'',m''_\mathrm{F}} E_{m''_\mathrm{F}-m_\mathrm{F}}\left(E'_{m''_\mathrm{F}-m'_\mathrm{F}}\right)^* \\
&\langle l=1,j,F'',m''_\mathrm{F}|\, r^{(1)}_{m''_\mathrm{F}-m_\mathrm{F}}\, |l=0,\frac{1}{2},F,m_\mathrm{F}\rangle \\
&\langle l=1,j,F'',m''_\mathrm{F}|\, r^{(1)}_{m''_\mathrm{F}-m'_\mathrm{F}}\, |l=0,\frac{1}{2},F',m'_\mathrm{F}\rangle\,.
\end{aligned} \tag{2-43}$$

In a typical case, we use 355 nm Raman lasers ($-\delta_{3/2} = 2\delta_{1/2} = 2\delta$) to couple $|0\rangle = |F=0, m_\mathrm{F}=0\rangle$ and $|1\rangle = |F=1, m_\mathrm{F}=0\rangle$ of $^2\mathrm{S}_{1/2}$ manifold (carrier operation). The Rabi frequency

$$\begin{aligned}
\Omega =&\frac{2e^2}{\hbar^2}\sum_{j=\frac{1}{2},\frac{3}{2}}\frac{1}{\delta_j}\sum_{F,m} E_m(E'_m)^* \\
&\langle l=1,j,F,m|\, r^{(1)}_m\, |l=0,\frac{1}{2},0,0\rangle \\
&\langle l=1,j,F,m|\, r^{(1)}_m\, |l=0,\frac{1}{2},1,0\rangle \\
=&\frac{e^2\langle 1\|r^{(0)}\|0\rangle^2}{4\hbar^2\delta}\left(E_1(E'_1)^* - E_{-1}(E'_{-1})^*\right)
\end{aligned} \tag{2-44}$$

is calculated according to Eq. (2-36). We thus establish relationships between the polarization of Raman lasers and the Rabi frequency of transitions.

2.6.2 Single-ion Raman operations

Compared to microwave, a photon of Raman laser contains a great deal of momentum. When an ion absorbs a photon from a Raman laser or emits a photon due to stimulated emission, the momentum of ion vastly changes. A more general effective Hamiltonian (see Eq. (2-42)) is

$$\frac{\hbar}{2}\begin{pmatrix} & \Omega e^{i(\vec{k}\cdot\vec{x}-\delta t-\phi)} \\ \Omega^* e^{i(\delta t+\phi-\vec{k}\cdot\vec{x})} & \end{pmatrix} \tag{2-45}$$

based by $|1\rangle$ and $|0\rangle$, where $\vec{k}=\vec{k}_0-\vec{k}_1$ is the wave vector difference of 2 Raman laser, $\phi=\phi_0-\phi_1$ is the phase difference, and $\delta=\delta_1-\delta_0$. For single ion and single vibrational mode case, we quantize

$$\vec{k}\cdot\vec{x}=kx=\eta\left(ae^{-i\nu t}+a^\dagger e^{i\nu t}\right), \tag{2-46}$$

where ν is angular frequency of mode, and $\eta=k\sqrt{\hbar/2M\nu}$ is called Lamb-Dicke parameter. For multiple ions and their shared vibrational modes, position of ion i is composed of many modes as follows.

$$kx_i=\sum_j \eta_{i,j}\left(a_j e^{-i\nu_j t}+a_j^\dagger e^{i\nu_j t}\right) \tag{2-47}$$

Vector $(\eta_{0,j},\eta_{1,j},\cdots\eta_{i,j},\cdots)$ describes the shape of mode j, which is calculate in 2.2.2.

In an ion-chain, a single-ion Raman operation addresses both Raman lasers on one ion. For $\eta_{i,j}\ll 1$, the Hamiltonian is

$$H_i=\frac{\hbar}{2}\left(\Omega e^{-i(\delta t+\phi)}\sigma_{i,+}\prod_j \exp\left[i\eta_{i,j}\left(a_j e^{-i\nu_j t}+a_j^\dagger e^{i\nu_j t}\right)\right]+\text{H.c.}\right) \tag{2-48}$$

$$\approx\frac{\hbar}{2}\left(\Omega e^{-i(\delta t+\phi)}\sigma_{i,+}\left(1+i\sum_j \eta_{i,j}\left(a_j e^{-i\nu_j t}+a_j^\dagger e^{i\nu_j t}\right)\right)+\text{H.c.}\right), \tag{2-49}$$

where $\sigma_{i,+}=|1_i\rangle\langle 0_i|$.

When $\delta=0$, according to rotating-wave approximation,

$$H_i\approx\frac{\hbar}{2}\left(\Omega e^{-i\phi}\sigma_{i,+}+\text{H.c.}\right). \tag{2-50}$$

By applying H_i with duration d, we implement a carrier operation

$$\begin{aligned}\mathrm{Carrier}_i[\chi,\phi] &= \exp\left[-\frac{i\chi}{2}\left(e^{-i\phi}\sigma_{i,+} + \mathrm{H.c.}\right)\right]\\ &= \begin{pmatrix} \cos\tfrac{\chi}{2} & -i\sin\tfrac{\chi}{2}e^{-i\phi} \\ -i\sin\tfrac{\chi}{2}e^{i\phi} & \cos\tfrac{\chi}{2}\end{pmatrix},\end{aligned} \tag{2-51}$$

where $\chi = \Omega d$.

When $\delta = -\nu_j$,

$$H_i \approx \frac{\hbar}{2}\left(i\eta_{i,j}\Omega e^{-i\phi}\sigma_{i,+}a_j + \mathrm{H.c.}\right), \tag{2-52}$$

which implements a red sideband operation

$$\begin{aligned}\mathrm{Red}_{i,j}[\chi,\phi] &= \exp\left[\frac{\chi}{2}\left(e^{-i\phi}\sigma_{i,+}a_j - \mathrm{H.c.}\right)\right]\\ &= \begin{pmatrix} \cos\left(\sqrt{a_j a_j^\dagger}\tfrac{\chi}{2}\right) & \mathrm{sinc}\left(\sqrt{a_j a_j^\dagger}\tfrac{\chi}{2}\right) a_j \tfrac{\chi}{2} e^{-i\phi} \\ -\mathrm{sinc}\left(\sqrt{a_j^\dagger a_j}\tfrac{\chi}{2}\right) a_j^\dagger \tfrac{\chi}{2} e^{i\phi} & \cos\left(\sqrt{a_j^\dagger a_j}\tfrac{\chi}{2}\right)\end{pmatrix},\end{aligned} \tag{2-53}$$

where $\chi = \eta_{i,j}\Omega d$.

When $\delta = \nu_j$,

$$H_i \approx \frac{\hbar}{2}\left(i\eta_{i,j}\Omega e^{-i\phi}\sigma_{i,+}a_j^\dagger + \mathrm{H.c.}\right), \tag{2-54}$$

which implements a blue sideband operation

$$\begin{aligned}\mathrm{Blue}_{i,j}[\chi,\phi] &= \exp\left[\frac{\chi}{2}\left(e^{-i\phi}\sigma_{i,+}a_j^\dagger - \mathrm{H.c.}\right)\right]\\ &= \begin{pmatrix} \cos\left(\sqrt{a_j^\dagger a_j}\tfrac{\chi}{2}\right) & \mathrm{sinc}\left(\sqrt{a_j^\dagger a_j}\tfrac{\chi}{2}\right) a_j^\dagger \tfrac{\chi}{2} e^{-i\phi} \\ -\mathrm{sinc}\left(\sqrt{a_j a_j^\dagger}\tfrac{\chi}{2}\right) a_j \tfrac{\chi}{2} e^{i\phi} & \cos\left(\sqrt{a_j a_j^\dagger}\tfrac{\chi}{2}\right)\end{pmatrix},\end{aligned} \tag{2-55}$$

where $\chi = \eta_{i,j}\Omega d$.

2.6.3 Sideband cooling

A sideband cooling operation alternatively applies red sideband and optical pumping operations (see 2.4.3). First, we discuss single-ion and single-mode case. At the beginning of each cycle, we suppose the ion starts with a mixed state

$$\rho = \sum_{m=0}^{\infty} p_m \begin{pmatrix} 0 & 0 \\ 0 & |m\rangle\langle m| \end{pmatrix}. \tag{2-56}$$

By applying Red$[\chi, 0]$, ρ goes to

$$\rho' = \sum_{m=0}^{\infty} \frac{p_m}{2} \begin{pmatrix} (1-\cos\chi_m)\,|m-1\rangle\langle m-1| & \sin\chi_m\,|m-1\rangle\langle m| \\ \sin\chi_m\,|m\rangle\langle m-1| & (1+\cos\chi_m)\,|m\rangle\langle m| \end{pmatrix}. \tag{2-57}$$

We calculate average phonon numbers of ρ and ρ', and find

$$\langle a^\dagger a\rangle_{\rho'} = \sum_{m=0}^{\infty} \left(m - \sin^2\frac{\chi_m}{2}\right) p_m < \sum_{m=0}^{\infty} m p_m = \langle a^\dagger a\rangle_{\rho}. \tag{2-58}$$

A optical pumping operation initializes the internal state of ρ' to $|0\rangle$, but doesn't change its average phonon number. Therefore, the average phonon number of ion decreases in each cycle. By enough cycles, the vibrational mode is eventually initialized to $|0\rangle$.

In practice, we assume there is a maximum phonon number q in state

$$\rho = \sum_{m=0}^{q} p_m \begin{pmatrix} 0 & 0 \\ 0 & |m\rangle\langle m| \end{pmatrix}. \tag{2-59}$$

In each cycle, we carefully set $\chi_q = \pi$, so that

$$\begin{aligned} \rho' = \sum_{m=0}^{q-1} \frac{p_m}{2} &\begin{pmatrix} (1-\cos\chi_m)\,|m-1\rangle\langle m-1| & \sin\chi_m\,|m-1\rangle\langle m| \\ \sin\chi_m\,|m\rangle\langle m-1| & (1+\cos\chi_m)\,|m\rangle\langle m| \end{pmatrix} \\ +p_q &\begin{pmatrix} |q-1\rangle\langle q-1| & 0 \\ 0 & 0 \end{pmatrix}, \end{aligned} \tag{2-60}$$

in which the maximum phonon number is $q-1$. A optical pumping operation won't change maximum phonon number. Therefore, in each cycle, q decreases by 1. We thus can decide the number of cycles of sideband cooling operation. From Eq. (2-53), we derive $\chi_q = \sqrt{q}\chi$. We note that, it is not true if q is large enough. From Eq. (2-48), we can derive $\chi_q = L^1_{q-1}[\eta^2]\chi/\sqrt{q}$, where L is Laguerre polynomial.

For N-ion case, we consider N vibrational modes in one direction (x, y or z direction, see 2.2.2). We label the ions as $i = 0, 1, \cdots, N-1$ from middle to sides (e.g. ion 2, ion 0, ion 1 and ion 3 from left to right), and the modes as $j = 1, 2, \cdots, N$ from center-mass (CM) mode to zig-zag (ZZ) mode (monotonic change in frequency). For relatively strong ion-mode couplings (relatively big $\eta_{i,j}$), we use ion i to conduct sideband cooling for mode $j = N - i$. Between 2 optical pumping operations, we apply $\mathrm{Red}_{0,N}$, $\mathrm{Red}_{1,N-1}$, $\cdots$ $\mathrm{Red}_{N-1,1}$ simultaneously for high efficiency. We carefully adjust the amplitudes of these red sideband operations, so that their durations for $\chi_q = \pi$ are the same.

2.7 Optics

In trapped-ion system, the operations of ions are usually realized by lasers. To observe ions, or collect fluorescence of ions during detection (see 2.4.1), a imaging system is required. In summary, a trapped-ion system requires a lot of optical systems, in which (especially in individual-addressing system) some advanced optical knowledges are demonstrated.

2.7.1 Gaussian beam

In general case, we use geometric optics to describe optical beams. In geometric optics, a concentrated beam can eventually be focused into a single point. However, when analysing around a focus point, geometric optics become invalid. In this situation, we describe the laser field by a Gaussian-beam model[20]

$$\frac{\omega_0}{\omega(z)} \exp\left[-i \arctan\frac{z}{z_\mathrm{R}} + ik\left(z + \frac{x^2+y^2}{2R(z)}\right) - \frac{x^2+y^2}{\omega^2(z)}\right], \tag{2-61}$$

where laser propagates along z-direction,

$$z_\mathrm{R} = \frac{k\omega_0^2}{2} \tag{2-62}$$

is called Rayleigh length,

$$R = z + \frac{z_\mathrm{R}^2}{z} \tag{2-63}$$

is wavefront radius, and

$$\omega = \omega_0 \sqrt{1 + \left(\frac{z}{z_\mathrm{R}}\right)^2} \tag{2-64}$$

is the radius of Gaussian beam. As we can see, when $k = 2n\pi/\lambda$ (λ is vacuum wavelength) is fixed, the Gaussian beam is solely characterized by waist radius $\omega_0 = \omega(z = 0)$.

When $z \gg z_\mathrm{R}$, Eq. (2-64) is approximated into $\omega = 2z/(k\omega_0)$, which fits into the geometric optical model. Therefore, ω_0 is usually calculated by $\omega_0 = 2z/(k\omega) = z/(n\pi\omega)$, where z/ω is a property of geometric beam.

2.7.2 ABCD rule

In geometric optics, the transformation of a ray in an optical path is described by

$$\begin{pmatrix} y_1 \\ y_1' \end{pmatrix} = \begin{pmatrix} A & B \\ C & D \end{pmatrix} \begin{pmatrix} y_0 \\ y_0' \end{pmatrix}, \tag{2-65}$$

where y_0 (y_1) is the height of input (output) ray, $y_0' = \partial y_0/\partial z$ (y_1') is its slope, and the ABCD matrix is a linear transformation. For example,

$$\begin{pmatrix} A & B \\ C & D \end{pmatrix} = \begin{pmatrix} 1 & d \\ 0 & 1 \end{pmatrix} \tag{2-66}$$

in a free-space propagation of distance d, and

$$\begin{pmatrix} A & B \\ C & D \end{pmatrix} = \begin{pmatrix} 1 & 0 \\ -\frac{1}{f} & 1 \end{pmatrix} \tag{2-67}$$

for a thin lens of focal length f.

Consider a geometric ray at the edge of a Gaussian beam, where $y = \omega$ and $y' = \omega/z \approx \sqrt{2/(kz_\mathrm{R})}$ (see Eq. (2-62)(2-64)). The q-parameter of a Gaussian beam becomes

$$q = z + iz_\mathrm{R} \approx \frac{y}{y'} + i\frac{2}{k(y')^2}. \tag{2-68}$$

We derive that

$$\begin{aligned}\frac{Aq_0 + B}{Cq_0 + D} &\approx \frac{Az_0 + B}{Cz_0 + D} + i\frac{AD - BC}{(Cz_0 + D)^2}(z_\mathrm{R})_0 \\ &\approx \frac{Ay_0 + By_0'}{Cy_0 + Dy_0'} + i\frac{AD - BC}{k_0}\frac{2}{(Cy_0 + Dy_0')^2} \\ &= \frac{y_1}{y_1'} + i\frac{2}{k(y_1')^2} = q_1,\end{aligned} \tag{2-69}$$

in which we use an important property

$$AD - BC = \begin{vmatrix} A & B \\ C & D \end{vmatrix} = \frac{n_0}{n_1} = \frac{k_0}{k_1}. \tag{2-70}$$

In individual-addressing system, we first abstract each addressing beam into a ray, and calculate their spatial distribution by geometric optics. Then, we analysis the details of each beam by considering only one paraxial Gaussian beam. In either geometric or Gaussian case, ABCD matrices are used to predict the transformations of beams. Therefore, we can roughly simulate and design the optical path.

第 3 章　Softwares in Mathematica

To assist quantum computation, softwares that run on a classic computer are necessary. In our softwares, the main structure (see Fig. 3.1) is aimed to serve any physical system that implements quantum computation, not specific in trapped-ion system. This part, which is called "skeleton", is written by myself. Some parts of our softwares realize specific functions, such as defining new operations, controlling signal generators and probes, and so on. These parts, called "muscles", are developed by me and others, according to the specific needs of our system. These "muscles" can be easily invoked by other systems. The control part of our softwares (see 3.2.3 and 3.3.2) should be adapted to the project currently running on our system. This part, called "brain", requires to be modified in real time by anyone in charge of the project. Our softwares possess 4 functions – algebraic calculation, numerical simulation, real-time experiment and data analysis, which correspond to 4 modules – theory, simulation, experiment and data analysis.

The module of theory (see Sec. 3.1) defines basic transitions (see "Transition" in Fig. 3.1) and their theoretical Hamiltonians (see "Hamiltonian" in Fig. 3.1). The definition of a single operation consists of a transition and its arguments. A composite definition joins several definitions from right to left via "**" (see "Definition" in Fig. 3.1). This module also calculates the theoretical effects of a definition (see "Operating" in Fig. 3.1).

The module of simulation (see Sec. 3.2) simulates interaction between a quantum system and a field (see "Field" in Fig. 3.1), described by a Hamiltonian in interaction picture (see "Hamiltonian" in Fig. 3.1). This module also simulatively implements sequentially applied waves, where each wave provides a field with duration d (see "Waves" in Fig. 3.1). The waves are usually compiled from a definition. The effects of waves are simulated as well (see "Operating" in Fig. 3.1).

The module of experiment (see Sec. 3.3) integrates necessary signal generators (see "Generator" in Fig. 3.1). In each trial of experiment, it instructs each generator g to generate desired signal from each channel (see "Channel" in Fig. 3.1) by loading these signals (see "Signals" in Fig. 3.1) to those generators. The signals are usually compiled from the waves. Therefore, such waves are physically implemented around the quantum system during each trial. This module then instructs the probe to collect raw data from repeated trials (see "Data" in Fig. 3.1), where the datum of each trial is translated into a

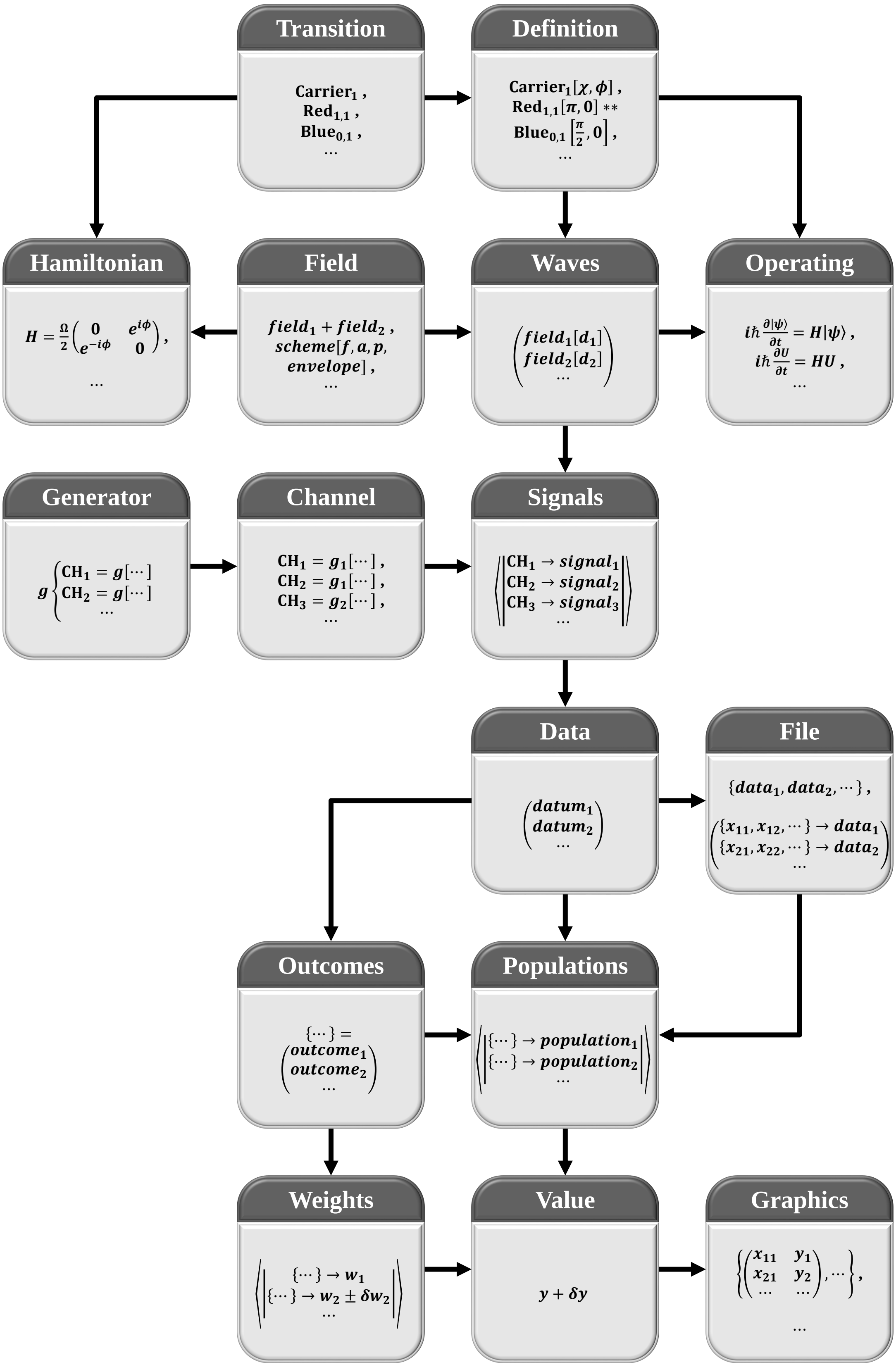
Transition
Carrier_1 , $\text{Red}_{1,1}$, $\text{Blue}_{0,1}$, …
Definition
$\text{Carrier}_1[\chi,\phi]$, $\text{Red}_{1,1}[\pi,0]$ ** $\text{Blue}_{0,1}\left[\frac{\pi}{2},0\right]$, …
Hamiltonian
$H=\frac{\Omega}{2}\begin{pmatrix}0 & e^{i\phi}\\ e^{-i\phi} & 0\end{pmatrix}$, …
Field
$field_1+field_2$, $scheme[f,a,p,envelope]$, …
Waves
$\begin{pmatrix}field_1[d_1]\\ field_2[d_2]\\ \cdots\end{pmatrix}$
Operating
$i\hbar\frac{\partial|\psi\rangle}{\partial t}=H|\psi\rangle$, $i\hbar\frac{\partial U}{\partial t}=HU$, …
Generator
$g\begin{cases}\text{CH}_1=g[\cdots]\\ \text{CH}_2=g[\cdots]\\ \cdots\end{cases}$
Channel
$\text{CH}_1=g_1[\cdots]$, $\text{CH}_2=g_1[\cdots]$, $\text{CH}_3=g_2[\cdots]$, …
Signals
$\left\langle\left|\begin{matrix}\text{CH}_1\to signal_1\\ \text{CH}_2\to signal_2\\ \text{CH}_3\to signal_3\\ \cdots\end{matrix}\right|\right\rangle$
Data
$\begin{pmatrix}datum_1\\ datum_2\\ \cdots\end{pmatrix}$
File
$\{data_1,data_2,\cdots\}$, $\begin{pmatrix}\{x_{11},x_{12},\cdots\}\to data_1\\ \{x_{21},x_{22},\cdots\}\to data_2\\ \cdots\end{pmatrix}$
Outcomes
$\{\cdots\}=\begin{pmatrix}outcome_1\\ outcome_2\\ \cdots\end{pmatrix}$
Populations
$\left\langle\left|\begin{matrix}\{\cdots\}\to population_1\\ \{\cdots\}\to population_2\\ \cdots\end{matrix}\right|\right\rangle$
Weights
$\left\langle\left|\begin{matrix}\{\cdots\}\to w_1\\ \{\cdots\}\to w_2\pm\delta w_2\\ \cdots\end{matrix}\right|\right\rangle$
Value
$y+\delta y$
Graphics
$\left\{\begin{pmatrix}x_{11} & y_1\\ x_{21} & y_2\\ \cdots & \cdots\end{pmatrix},\cdots\right\}$, …

图 3.1　**Main structure of our softwares.**

set of outcomes (see "Outcomes" in Fig. 3.1). The population of each set of outcomes is finally counted (see "Populations" in Fig. 3.1).

The module of data analysis (see Sec. 3.4) can operate in online mode (during experiment) or offline mode (after experiment). In online mode, by scanning the trial configuration, a bunch of data sets are collected and recorded in a data file (see "File" in Fig. 3.1). Meanwhile, each data set is translated into a population distribution (as stated in previous paragraph) in real time, and all distributions are recorded in a global variable. In offline mode, the population distributions are obtained from a recorded data file. In either mode, each population distribution is processed by linearly superimposing each fractional population with a desired weight w (see "Weights" in Fig. 3.1). In addition to the resulting value y, its standard deviation δy is also calculated (see "Value" in Fig. 3.1). For each set of weights, the population distributions are converted to values, which are visualized as a curve. Multiple curves can be displayed simultaneously in one graph (see "Graphics" in Fig. 3.1). This module also fits each curve into a custom model, which can be displayed along with the curve.

Our softwares are implemented by many notebook files written in Mathematica. The name of each file takes the form of “file_version.nb” (e.g. “Basis_5.2.nb”), where "file" describes its function, "version" is the version number, and "nb" indicates that it is a notebook file. All files must be in the same directory. A higher-level file may require some lower-level files. A lower-level file may be required by many higher-level files. To avoid being loaded more than once, each file uses the **LoadQ** function to mark whether it has been loaded. For example, the following code is embedded in any version of “Basis_*.nb”.

```
LoadQ["Basis"] = True;
```

If a version of “Basis_*.nb” is loaded, **LoadQ**[“Basis”] is set to **True**. When a higher-level file, such as “Simulation_Basis_*.nb”, requires “Basis_*.nb”, it checks the value of **LoadQ**[“Basis”]. If **LoadQ**[“Basis”] is **True**, “Simulation_Basis_*.nb” refuses to import any version of “Basis_*.nb”. Otherwise (**LoadQ**[“Basis”] is unassigned by default), “Simulation_Basis_*.nb” imports the last version of “Basis_*.nb”. The user can then load any parts of our softwares as needed by importing corresponding files from correct directory.

3.0.1 Quantum system

Notebook file "Basis_*.nb" introduces a quantum system, which consists of a number of particles (particle $0, 1, \cdots, i, \cdots$) and bosonic modes (mode $1, 2, \cdots, j, \cdots$). Any pure state of particle i is represented by a vector, based by finite levels $|0_i\rangle, |1_i\rangle, \cdots, |n_i\rangle, \cdots$. The user can customize the dimension of such vector by setting **DimensionOfParticle**[i]. For example, the following code introduces 2 2-level particles.

```
DimensionOfParticle[0] = 2;
DimensionOfParticle[1] = 2;
```

Mode j is based by infinite Fock states $|0_{-j}\rangle, |1_{-j}\rangle, \cdots, |m_{-j}\rangle, \cdots$.

In "Representation_Matrix_*.nb", mode j is treated as particle $-j$, in which only a finite number of Fock states with the lowest energy are considered. The user can customize the dimension of mode j by setting **DimensionOfParticle**[$-j$]. For example, the following code introduces mode 1, in which only Fock states $|0_{-1}\rangle$, $|1_{-1}\rangle$ and $|2_{-1}\rangle$ are considered.

```
DimensionOfParticle[-1] = 3;
```

After **DimensionOfParticle**[i] is set, number of particles N and number of modes M are determined, where N is calculated by **CountParticles**[] $= i_{max} + 1$ and M by **CountModes**[] $= j_{max}$.

```
CountParticles[];
CountModes[];
```

Here, i_{max} (j_{max}) is the index of last particle (mode) that has been assigned a demension. In "Simulation_Basis_*.nb" (see 3.2.1), i_{max} and j_{max} are redefined. Therefore, **CountParticles**[] and **CountModes**[] are overridden.

In our softwares, a function like **DimensionOfParticle**[i], which can be set by users, is called a variable function. Each variable function is wrapped by a standard function, which rejects illegal arguments and promises a legal return. The following function wraps variable function **DimensionOfParticle**[i].

```
DimensionOfSystem[i_Integer];
```

If a variable function is unassigned or illegally assigned (e.g. **DimensionOfParticle**[2] is unassigned), its wrapped function reports an error and returns a default value (e.g. **DimensionOfSystem**[2] returns 1). Otherwise, the wrapped function behaves the same as variable function.

The following function calculates the dimension of system that consists of particles $i_0, i_0+1, \cdots, i_1-1$ (mode j is particle $-j$).

```
DimensionOfSystem[i0_Integer, i1_Integer];
```

For example, the dimension of all particles (modes are excluded) is **DimensionOfSystem**$[0, N]$. Therefore, any pure state of all particles is represented by a vector of such dimension, based by $|0\rangle, |1\rangle, \cdots, |n\rangle, \cdots$. By representing integer n with a mixed-radix numeral

$$|n = n^{(N-1)} \cdots n^{(1)} n^{(0)}\rangle = |n_{N-1}^{(N-1)}\rangle \otimes \cdots \otimes |n_1^{(1)}\rangle \otimes |n_0^{(0)}\rangle, \tag{3-1}$$

the digit $n^{(i)}$ is associated with the state of particle i.

In “Representation_Matrix_*.nb”, any base state of all modes is denoted as

$$|\{m^{(1)}, m^{(2)}, \cdots, m^{(M)}\}\rangle = |m_{-1}^{(1)}\rangle \otimes |m_{-2}^{(2)}\rangle \otimes \cdots \otimes |m_{-M}^{(M)}\rangle. \tag{3-2}$$

Another notation of vacuum state is a complex number

$$|0.i\rangle = |0_{-1}\rangle \otimes |0_{-2}\rangle \otimes \cdots \otimes |0_{-M}\rangle. \tag{3-3}$$

Any other base state of all modes is also denoted as a rational number

$$|m = \frac{m^{(1)} m^{(2)} \cdots m^{(M)}}{\textbf{DimensionOfSystem}[-M, 0]}\rangle = |m_{-1}^{(1)}\rangle \otimes |m_{-2}^{(2)}\rangle \otimes \cdots \otimes |m_{-M}^{(M)}\rangle, \tag{3-4}$$

where numerically $m = 0.m^{(1)} m^{(2)} \cdots m^{(M)}$. Any base state of all particles and modes is denoted as a real number

$$|n^{(N-1)} \cdots n^{(0)}.m^{(1)} \cdots m^{(M)}\rangle = |n_{N-1}^{(N)}\rangle \otimes \cdots \otimes |n_0^{(0)}\rangle \otimes |m_{-1}^{(1)}\rangle \otimes \cdots \otimes |m_{-M}^{(M)}\rangle, \tag{3-5}$$

where the j-th decimal place corresponds to mode j.

In “Representation_Matrix_*.nb”, for any mode j, the annihilation operator a_j, and its derivatives a_j^m $(m = 2, 3, \cdots)$, $e^{\alpha a_j}$ and $e^{\alpha a_j^\dagger}$, are represented in matrix form.

3.1 Module for theory

3.1.1 Transition and theoretical Hamiltonian

Notebook file “Theory_Basis_*.nb”, which requires “Basis_*.nb”, defines basic transitions (see "Transition" in Fig. 3.1). Transition $|(n_0)_i\rangle \leftrightarrow |(n_1)_i\rangle$ within particle i is denoted as $i[\{n_0, n_1\}, \{\}]$. The user can customize the main carrier transition of particle i by setting variable function **CarrierOfParticle**$[i] = \{n_0, n_1\}$. For example, the following code sets carrier to $|0_i\rangle \leftrightarrow |1_i\rangle$ for both particle 0 and particle 1.

```
CarrierOfParticle[0] = {0, 1};
CarrierOfParticle[1] = {0, 1};
```

The following function wraps **CarrierOfParticle**$[i]$.

```
Carrier[i_Integer];
```

Sideband $|(n_0)_i m_{-1}^{(1)} m_{-2}^{(2)} \cdots m_{-j}^{(j)}\rangle \leftrightarrow |(n_1)_i (m^{(1)} + m_1)_{-1} (m^{(2)} + m_2)_{-2} \cdots (m^{(j)} + m_j)_{-j}\rangle$ is denoted as

$$i[\{n_0, n_1\}, \{m_1, m_2, \cdots, m_j\}], \tag{3-6}$$

where $m_j \neq 0$ (if $m_j = 0$, it should be removed).

The following function defines the theoretical Hamiltonian of a transition (see "Hamiltonian" in Fig. 3.1).

```
HamiltonianTheoretical[transition_, args___];
```

For example, **HamiltonianTheoretical**$[i[\{n_0, n_1\}, \{m_1 > 0, \cdots, m_j < 0\}], \rho, \phi]$ returns

$$H = \frac{\rho}{2}\left(e^{-i\phi}\,|(n_1)_i\rangle\,\langle(n_0)_i|\,\frac{i^{m_1}(a_1^\dagger)^{m_1}}{\sqrt{m_1!}}\cdots\frac{i^{-m_j}a_j^{-m_j}}{\sqrt{(-m_j)!}} + \text{H.c.}\right), \tag{3-7}$$

where ρ is a dimensionless intensity and ϕ is the phase.

In our softwares, to save users from inputing human-unfriendly forms (see Eq. (3-6)), interface functions are developed. The following interface function resolves a transition from an interface form to a standard form.

```
ResolveTransition[transition_];
```

For example, **ResolveTransition**[**Carrier**$_i$] returns i[**Carrier**$[i]$, $\{\}$]. Its red or blue sideband, denoted as **Red**$_{i,j}$ or **Blue**$_{i,j}$, is resolved to i[**Carrier**$[i]$, $\{0, 0, \cdots, 0, m_j = \pm 1\}$].

In our softwares, some standard functions are wrapped by interface functions. The following interface function wraps **HamiltonianTheoretical**.

```
HTheo[transition_, args___];
```

An interface function allows arguments in interface form (e.g. **HTheo**[**Carrier**$_1$, ρ, ϕ], **HTheo**[**Red**$_{1,1}$, ρ, ϕ] and **HTheo**[**Blue**$_{0,1}$, ρ, ϕ] are allowed).

3.1.2 Definition and theoretical operation

Notebook file “Theory_Definition_*.nb”, which requires “Theory_Basis_*.nb”, introduces the definition of operations (see "Definition" in Fig. 3.1). A definition, denoted as $transition[args]$, consists of a transition (e.g. Eq. (3-6)) and its arguments (e.g. rotation angle χ and phase ϕ).

The following function calculates the theoretical effects of a definition (see "Operating" in Fig. 3.1).

```
OperateTheoretically[definition_, ψ_];
```

If ψ is a state represented by a vector, **OperateTheoretically** regards ψ as input and returns the output of definition. If ψ is 1, **OperateTheoretically** returns a matrix that describes definition. For example, **OperateTheoretically**[$i[\{n_0, n_1\}, \{\}][\chi, \phi]$, 1] returns

$$U = \cos\frac{\chi}{2} - i\sin\frac{\chi}{2}\left(e^{-i\phi}\left|(n_1)_i\right\rangle\left\langle(n_0)_i\right| + e^{i\phi}\left|(n_0)_i\right\rangle\left\langle(n_1)_i\right|\right), \tag{3-8}$$

where $n_1 \neq n_0$.

The following interface function resolves a definition $transition[args]$ from an interface form to a standard form, usually by resolving transition and keeping arguments.

```
ResolveDefinition[definition_];
```

Several interface-form definitions can be joined into a composite definition from right to left via "**" (e.g. **Red**$_{1,1}[\pi, 0] * *$**Blue**$_{0,1}[\pi/2, 0]$).

The following interface function wraps **OperateTheoretically**.

```
OpTheo[definition_, ψ_];
```

This function allows a interface-form definition (composite definition is included).

3.2 Module for simulation

3.2.1 Field and interaction Hamiltonian

Notebook file “Simulation_Basis_*.nb”, which requires “Basis_*.nb”, simulates interaction between a quantum system and a field (see "Field" in Fig. 3.1). A typical field takes the form of $scheme[f, a, p, envelope]$, where $scheme$ determines the distribution of field around the quantum system (e.g. $scheme = i$ indicates that the field is focused around particle i), f is the frequency (not angular frequency) in MHz, a is a dimensionless amplitude, p is the phase in unit of π, and $envelope$ describes the slow variation of field over time (global time t and real-time duration τ). Such field is proportional to

$$\frac{a}{2}\left((-1)^{-2ft-p}envelope + (-1)^{2ft+p}envelope^*\right). \tag{3-9}$$

Several fields can be superimposed into a composite field (e.g. $field_1 + field_2$).

The user can characterize the quantum system by setting the following variable functions.

```
FrequencyOfParticle[0, 1] = 32.;
FrequencyOfParticle[1, 1] = 32.;
FrequencyOfMode[1] = 2.;
FrequencyOfRabi[0, 0, {0, 0}] = 0.25 + 0. I;
FrequencyOfRabi[0, 0, {0, 1}] = 0.25 + 0. I;
FrequencyOfRabi[0, 0, {1, 1}] = 0.25 + 0. I;
FrequencyOfRabi[1, 0, {0, 1}] = 0. + 0.015625 I;
FrequencyOfRabi[1, 1, {0, 1}] = 0.5 + 0. I;
LambDickeParameter[0, 0, 1] = 0.125;
LambDickeParameter[0, 1, 1] = 0.125;
LambDickeParameter[1, 0, 1] = 0.125;
LambDickeParameter[1, 1, 1] = 0.125;
```

For base state $|n_i\rangle$ of particle i, **FrequencyOfParticle**$[i, n] = \omega_n^{(i)}$ (in MHz) determines its absolute energy $h\omega_n^{(i)}$. **FrequencyOfMode**$[j] = \nu_j$ (in MHz) is the frequency (not angular frequency) of bosons in mode j. **FrequencyOfRabi**$[scheme, i, \{n_0, n_1\}] = \Omega^{(i)}_{n_1,n_0}$ (in MHz) is the Rabi frequency of transition $|(n_0)_i\rangle \leftrightarrow |(n_1)_i\rangle$, when $a = envelope = 1$. **LambDickeParameter**$[scheme, i, j] = \eta_{i,j}$ is the Lamb-Dicke parameter of particle i and mode j. The following functions wrap these variable functions.

```
FreqOfParticle[i_Integer, n_Integer];
FreqOfMode[j_Integer];
FreqOfRabi[scheme_, i_Integer, nList : {_Integer, _Integer}];
Eta[scheme_, i_Integer, j_Integer];
```

In “Simulation_Basis_*.nb”, **CountParticles**[] = $i_{max}+1$ and **CountModes**[] = j_{max}, which are defined in “Basis_*.nb” (see 3.0.1), are overridden.

```
CountParticles[];
CountModes[];
```

Here, i_{max} (j_{max}) is the index of last particle (mode) that has been defined in **FrequencyOfParticle**[i, n] (**FrequencyOfMode**[j]).

The following function simulates interaction between the quantum system and the field by a Hamiltonian (see "Hamiltonian" in Fig. 3.1) in interaction picture ($H_0 = \sum_{i,n} \omega_n^{(i)} \left|n_i\right\rangle \left\langle n_i\right| + \sum_j \nu_j a_j^\dagger a_j$).

```
HamiltonianInInteractionPicture[field_];
```

For example, **HamiltonianInInteractionPicture**[$scheme[f, a, p, envelope]$] returns

$$H = \frac{a}{2}\left((-1)^{-2ft-p} envelope \sum_{i=0}^{N-1} H_+^{(i)} D_+^{(i)} + \text{H.c.}\right), \tag{3-10}$$

where

$$H_+^{(i)} = \sum_{n_0,n_1} \Omega_{n_1,n_0}^{(i)} (-1)^{2(\omega_{n_1}^{(i)}-\omega_{n_0}^{(i)})t} \left|(n_1)_i\right\rangle \left\langle (n_0)_i\right|, \tag{3-11}$$

$$D_+^{(i)} = \prod_{j=1}^{M} \exp\left[i\eta_{i,j}(-1)^{2\nu_j t} a_j^\dagger\right] \exp\left[i\eta_{i,j}(-1)^{-2\nu_j t} a_j\right]. \tag{3-12}$$

This function also simulates the Hamiltonian of a composite field (e.g. **HamiltonianInInteractionPicture**[$field_1 + field_2$] returns **HamiltonianInInteractionPicture**[$field_1$] + **HamiltonianInInteractionPicture**[$field_2$]).

3.2.2 Waves and simulative operation

Notebook file “Simulation_Wave_*.nb”, which requires 2 lower-level notebook files “Theory_Definition_*.nb” and “Simulation_Basis_*.nb”, simulatively implements sequentially applied waves (see "Waves" in Fig. 3.1). Each wave, denoted as $field[d]$, provides a field with duration d. The waves are usually compiled from a definition. The user can establish relationships between standard-form definitions and waves by setting the following variable functions.

```
FrequencyOfTransition[0, 0[{0, 1}, {}]] = 32.;
FrequencyOfTransition[0, 0[{0, 1}, {-1}]] = 30.015625;
FrequencyOfTransition[0, 0[{0, 1}, {1}]] = 33.984375;
FrequencyOfTransition[1, 1[{0, 1}, {}]] = 32.;
FrequencyOfTransition[1, 1[{0, 1}, {-1}]] = 30.0625;
FrequencyOfTransition[1, 1[{0, 1}, {1}]] = 33.9375;
AmplitudeOfTransition[0, 0[{0, 1}, {}]] = 1.;
AmplitudeOfTransition[0, 0[{0, 1}, {-1}]] = 1.;
AmplitudeOfTransition[0, 0[{0, 1}, {1}]] = 1.;
AmplitudeOfTransition[1, 1[{0, 1}, {}]] = 1.;
AmplitudeOfTransition[1, 1[{0, 1}, {-1}]] = 1.;
AmplitudeOfTransition[1, 1[{0, 1}, {1}]] = 1.;
DurationOfTransition[0, 0[{0, 1}, {}]] = 2.;
DurationOfTransition[0, 0[{0, 1}, {-1}]] = 16.;
DurationOfTransition[0, 0[{0, 1}, {1}]] = 16.;
DurationOfTransition[1, 1[{0, 1}, {}]] = 1.;
DurationOfTransition[1, 1[{0, 1}, {-1}]] = 8.;
DurationOfTransition[1, 1[{0, 1}, {1}]] = 8.;
```

FrequencyOfTransition$[scheme, transition] = f$ (in MHz) is the resonant frequency of transition. **AmplitudeOfTransition**$[scheme, transition] = a$ is the typical amplitude of transition. **DurationOfTransition**$[scheme, transition] = d$ (in μs) is the duration of a π rotation. The following functions wrap these variable functions.

```
ResonantFrequency[scheme_, transition_];
TransitionAmplitude[scheme_, transition_];
PiDuration[scheme_, transition_];
```

The following interface functions wrap the above functions.

```
Freq[scheme_, transition_];
Amp[scheme_, transition_];
PiTime[scheme_, transition_];
```

The following functions get and set the Ramsey frequency of a transition.

```
RamseyFrequency[transition_];
SetRamseyFrequency[transition_, f_Real];
```

For example, **RamseyFrequency**$[i[\{n_0, n_1\}, \{m_1, m_2, \cdots, m_j\}]]$ returns $\omega^{(i)}_{n_1} - \omega^{(i)}_{n_0} + \sum_j m_j \nu_j$, and **SetRamseyFrequency**$[i[\{n_0, n_1\}, \{m_1, m_2, \cdots, m_j\}], f]$ (**SetRamseyFrequency**$[i[\{n_0, n_1\}, \{\}], f]$) sets Ramsey frequency to f by resetting **FrequencyOfMode**$[j]$ (**FrequencyOfParticle**$[i, n_1]$). The following interface function wraps **RamseyFrequency**.

```
Ramsey[transition_];
```

The following function compiles a standard-form definition into waves.

```
WavesFromDefinition[definition_];
```

For example, for $transition = i[\{n_0, n_1\}, \{m_1, m_2, \cdots, m_j\}]$, **WavesFromDefinition**$[transition[\chi, \phi]]$ returns $\{i[f, a, p, 1][d]\}$, where $f =$ **ResonantFrequency**$[i, transition]$, $a =$ **TransitionAmplitude**$[i, transition]$, $p = \phi/\pi$ and $d = \chi$**PiDuration**$[i, transition]/\pi$. The following interface function wraps **WavesFromDefinition**.

```
Waves[definition_];
```

The following function simulates the effects of waves (see "Operating" in Fig. 3.1).

```
OperateSimulatively[waveList : {_@_Real ...}, ψ_List];
OperateSimulatively[waveList : {_@_Real ...}, ψ_?NumericQ];
```

In matrix representation ("Representation_Matrix_*.nb" is required), **HamiltonianInInteractionPicture** returns a numerical matrix. **OperateSimulatively** then functions by numerically solving Schrödinger equations. The following interface function wraps **OperateSimulatively**.

```
OpSim[definition_, ψ_];
```

This function first compiles a interface-form definition into waves by **Waves** and then invokes **OperateSimulatively**.

3.2.3 Initialization and reorganization of parameters

Notebook file "Simulation_Control_*.nb", which is a "brain" unit that requires "Simulation_Wave_*.nb" and necessary "muscles" (e.g. "Operation_*_*.nb" that define new operations), initializes and reorganizes the parameters assigned to variable functions **DimensionOfParticle**, **CarrierOfParticle**, **FrequencyOfParticle**, **FrequencyOfMode**, **FrequencyOfRabi**, **LambDickeParameter**, **FrequencyOfTransition**, **AmplitudeOfTransition** and **DurationOfTransition**. As N and M increase, the number of such parameters increases rapidly. To save users from manually assigning such parameters, the following function is recommended to be developed.

```
InitializeVariables[];
```

A typical protocol is that, the user assigns a few parameters to provide necessary informations, and **InitializeVariables**[] realizes one-click initialization.

3.3 Module for experiment

3.3.1 Signals

Notebook file “Experiment_Signal_*.nb”, which requires “Simulation_Wave_*.nb”, compiles waves into signals generated in experiment (see "Signals" in Fig. 3.1). The user can customize the delay time of each channel (see "Channel" in Fig. 3.1), by setting variable function **DelayTimeOfChannel**[*channel*]. The following function wraps **DelayTimeOfChannel**[*channel*].

```
DelayOfChannel[channel_];
```

The default value of **DelayTimeOfChannel** is 0. To synchronize signals, each signal is advanced by time **DelayOfChannel**[*channel*] during compilation.

The following function compiles a field into signals.

```
SignalsFromField[field_];
```

In “Experiment_Signal_*.nb”, only symbolic compilation is provided due to lack of hardwares. In an online version of “Experiment_Control_*.nb” (see 3.3.2), **SignalsFromField** should be overridden according to experimental needs.

The following function compiles waves by sequentially compiling each field.

```
SignalsFromWaves[waveList : {_@Except@_List ...}];
```

For example, **SignalsFromWaves**[$\{\cdots, field_j[d_j], \cdots\}$] returns a form of

$$\left\langle \left| \cdots, channel_i \to \begin{pmatrix} \cdots & \cdots & \cdots \\ signal_{i,j} & \sum_{k=1}^{j-1} d_k - \delta t_i & \sum_{k=1}^{j} d_k - \delta t_i \\ \cdots & \cdots & \cdots \end{pmatrix}, \cdots \right| \right\rangle, \tag{3-13}$$

where $channel_i = g[\cdots]$ is a channel of generator g (see "Generator" in Fig. 3.1), and its signal describes a piecewise function

$$\begin{cases} \cdots & \cdots \\ signal_{i,j} & \sum_{k=1}^{j-1} d_k - \delta t_i \le t < \sum_{k=1}^{j} d_k - \delta t_i \\ \cdots & \cdots \end{cases}, \tag{3-14}$$

where $signal_{i,j}$ is compiled from $field_j$ by **SignalsFromField**, and δt_i = **DelayOfChannel**[$channel_i$]. The following interface function wraps **SignalsFromWaves**.

```
Signals[definition_];
```

This function first compiles a interface-form definition into waves by **Waves** and then invokes **SignalsFromWaves**. Each signal returned by **Signals** is in form of Eq. (3-14), which is human-friendly but hard to be further processed.

3.3.2 Experimental control

Notebook file “Experiment_Control_*.nb”, which is a "brain" unit that requires “Simulation_Control_*.nb”, “Experiment_Signal_*.nb”, “Generator_*_*.nb” and “Probe_*_*.nb”, can be an online or offline version. An offline version does nothing except importing low-level files. An online version integrates and initializes necessary hardwares.

Each “Generator_*_*.nb” interfaces with a specific model of generators. The following function loads a signal to a channel.

```
LoadSignalToChannel[signal_, channel_];
```

The following function loads signals (see Eq. (3-13)) to all channels of generator g.

```
LoadSignalsToGenerator[signalAssociation_Association, g_];
```

Each “Probe_*_*.nb” interfaces with a probe. The following function collects raw data from repeated trials (see "Data" in Fig. 3.1).

```
ToData[];
```

A typical data set consists of datum from each trial. The following function translates a datum into a set of outcomes (see "Outcomes" in Fig. 3.1).

```
OutcomesFromDatum[datum_];
```

The following function translates a data set into a population distribution, which counts the population of each set of outcomes (see "Populations" in Fig. 3.1).

```
PopulationsFromData[data_List];
```

An online version of “Experiment_Control_*.nb” should override or overload some functions according to experimental needs. For example, **SignalsFromField** should be overridden to instruct generators to generate signals that implement each field.

3.3.3 Data collection

Notebook file “Experiment_Data_*.nb”, which requires an online version of “Experiment_Control_*.nb”, collects data from configured trials. The following function collects a data set from repeated trials configured by loading signals (see Eq. (3-13)).

```
DataFromSignals[signalAssociation_Association];
```

The following interface functions wrap **DataFromSignals**.

```
Data[definition_];
Populations[definition_];
```

Both functions first compile a interface-form definition into signals by **Waves** and **SignalsFromWaves**. **Data** then invokes **DataFromSignals**. **Populations** further translates the data set to a population distribution by **PopulationsFromData**.

The following function scans the trial configuration, and records the data set of each configuration in a data file.

```
ScanSignalsToFile[signalAssociationList : {___Association}, file_String];
ScanSignalsToFile[{signalAssociation_Association, xLists : {_, __} ..}, file_String];
```

Here, each data set is translated into a population distribution in real time, and all distributions are recorded in a global variable $**Populations**. If the trial configuration is a function of $x_1, x_2, \cdots$, by scanning horizontal coordinates $x_1, x_2, \cdots$, $**Populations** is recorded in a form of

$$\left\langle \left| \cdots, \{x_{l,1}, x_{l,2}, \cdots\} \to \left\langle \left| \begin{matrix} \cdots \\ \{outcome_{n,1}, \cdots\} \to population_{l,n} \\ \cdots \end{matrix} \right| \right\rangle, \cdots \right| \right\rangle. \tag{3-15}$$

If trial configurations are itemized in a list, $**Populations** also itemizes each population distribution in a list.

The following function scans the trial configuration that is in form of waves.

```
ScanWavesToFile[waveListList : {{_@_Real ...} ...}, file_String];
ScanWavesToFile[{waveList : {_@Except@_List ...}, xLists : {_, __} ..}, file_String];
```

In addition to **ScanSignalsToFile**, **ScanWavesToFile** also creates a notebook file, in which necessary informations (e.g. parameters mentioned in 3.2.3 and the first argument of **ScanWavesToFile**) are logged.

3.4 Module for data analysis

3.4.1 Data processing

Notebook file “Data_Basis_*.nb”, which requires an online or offline version of “Experiment_Control_*.nb”, processes data during or after experiment. The following function obtains population distributions from a recorded data file (see "File" in Fig. 3.1).

```
PopulationsFromFile[file_String];
```

In our softwares, data files are recommended to store in an established database located in the directory recorded by global variable $**DirectoryOfData**. The following interface function resolves a file name to a recommended file path.

```
ResolveFile[file_String];
```

The following interface function wraps **PopulationsFromFile**.

```
FilePopulations[file_String];
```

This function allows a simple file name.

The following function processes a population distribution by linearly superimposing each fractional population with a desired weight (see "Weights" in Fig. 3.1).

```
ValueFromPopulations[
  populationAssociation : <|(_List -> _Integer) ...|>,
  wAssociation : <|(_List -> _) ...|>
  ];
```

For example, with arguments $\langle|\cdots,\{\cdots\}\to population_n,\cdots|\rangle$ and $\langle|\cdots,\{\cdots\}\to w_n+\delta w_n,\cdots|\rangle$, **ValueFromPopulations** returns $y+\delta y$ (see "Value" in Fig. 3.1), where δw_n and δy are standard deviations, and

$$y=\frac{\sum_n w_n population_n}{\sum_n population_n}. \tag{3-16}$$

The following function processes population distributions for each set of weights.

```
ValuesFromPopulations[
  populationAssociations :
   {<|(_List -> _Integer) ...|> ...} |
    <|(_List -> <|(_List -> _Integer) ...|>) ...|>,
  wAssociations :
   {<|(_List -> _) ...|> ...} |
    <|(_ -> <|(_List -> _) ...|>) ...|>
  ];
```

```
ValuesFromPopulations[
  populationAssociations :
   {<|(_List -> _Integer) ...|> ...} |
    <|(_List -> <|(_List -> _Integer) ...|>) ...|>,
  All
  ];
```

If the first argument is Eq. (3-15) and the second is

$$\left\langle\left|\cdots, \text{Expression}_m \to \left\langle\left|\begin{matrix}\cdots\\ \{outcome_{n,1},\cdots\} \to w_{m,n} + \delta w_{m,n}\\ \cdots\end{matrix}\right|\right\rangle, \cdots\right|\right\rangle, \tag{3-17}$$

ValuesFromPopulations returns

$$\left\langle\left|\cdots, \text{Expression}_m \to \left\langle\left|\begin{matrix}\cdots\\ \{x_{l,1}, x_{l,2},\cdots\} \to y_{m,l} + \delta y_{m,l}\\ \cdots\end{matrix}\right|\right\rangle, \cdots\right|\right\rangle. \tag{3-18}$$

If the first (second) argument is a list, dimension l (m) of Eq. (3-18) degenerates into a list. If the second argument is **All**, then $\text{Expression}_m = \{outcome_{m,1}, outcome_{m,2}, \cdots\}$ and $y_{m,l} = population_{l,m}/\sum_m population_{l,m}$.

The following function visualizes experimental values (see "Graphics" in Fig. 3.1).

```
PlotValues[
  ysList :
   {{_Real ±_Real ...} ...} |
    {<|(_List -> _Real ±_Real) ...|> ...}
  , options : OptionsPattern[]];
PlotValues[
  ysAssociation :
   <|(_ -> {_Real ±_Real ...}) ...|> |
    <|(_ -> <|(_List -> _Real ±_Real) ...|>) ...|>
  , options : OptionsPattern[]];
```

If the first argument takes the form of Eq. (3-18), the dimension of horizontal coordinates is recommended to be 1. Therefore, each $\langle|\cdots, \{x_{l,1}\} \to y_{m,l} + \delta y_{m,l}, \cdots|\rangle$ is visualized as a curve labeled Expression_m, and multiple curves are simultaneously displayed in one graph. If dimension l is a list, the horizontal coordinates of graph are $1, 2, \cdots$. If dimension m is a list, curves are unlabelled.

3.4.2 Data fitting

Notebook file “Data_Fitting_*.nb”, which requires “Data_Basis_*.nb”, fits processed data. The following function fits experimental values into a custom model.

```
FitValues[
  yList : {_Real ±_Real ...},
  form_, βList_List, x_
  , options : OptionsPattern[]];
FitValues[
  yAssociation : <|(_List -> _Real ±_Real) ...|>,
  form_, βList_List, x_
  , options : OptionsPattern[]];
```

For example **FitValues**$[\{\cdots, y_l + \delta y_l, \cdots\}, kx + b, \{b, k\}, x]$ returns a linearly fitted model, where variable x is automatically assigned $1, 2, \cdots$. This function also allows multidimensional horizontal coordinates (e.g. **FitValues**$[\langle| \cdots, \{x_{l,1}, x_{l,2}, \cdots\} \longrightarrow y_l + \delta y_l, \cdots |\rangle, k_1 x_1 + k_2 x_2 + \cdots + b, \{b, k_1, k_2, \cdots\}, \{x_1, x_2, \cdots\}]$).

第 4 章 Operational consequences of the UNOT gate

The NOT gate that flips a classical bit is ubiquitous in classical information processing. However its quantum analogue, the universal NOT (UNOT) gate that flips a quantum spin in any alignment into its antipodal counterpart is strictly forbidden. Here we explore the connection between this discrepancy and how UNOT gates affect classical and quantum correlations. We show that while a UNOT gate always preserves classical correlations between two spins, it can non-locally increase or decrease their shared discord in ways that allow violation of the data processing inequality. We experimentally illustrate this using a multi-level trapped $^{171}\mathrm{Yb}^{+}$ ion that allows simulation of anti-unitary operations.

4.1 Introduction

When given a quantum spin pointing in some unknown direction $\vec{n}$, is it possible to engineer a universal device that flips this spin to point in the antipodal direction $-\vec{n}$? While this process is easy to envision for classical vectors, it is strictly impossible for quantum spins. The quantum operation that takes an arbitrary quantum state $|\varphi\rangle$ to its orthogonal complement $|\varphi^{\perp}\rangle$ is anti-unitary, and thus does not exist[21–24]. Like the no-cloning theorem, this uniquely quantum constraint has drawn significant scientific interest[25–27].

In contrast to cloning, the radical operational consequences of the UNOT gate are not as readily apparent on a single qubit. Suppose Alice secretly encodes a direction $\vec{n}$ in 3-dimensional space by preparing a spin aligned in $\vec{n}$. She then challenges Bob to estimate $\vec{n}$. If Bob can perfectly clone quantum states, then he can violate the uncertainty principle by measuring each clone in a different complementary basis. On the other hand, any measurement Bob makes after applying a UNOT gate on the input spin can be simulated by measuring the input directly and reinterpreting the measurement outcome (recording ‘up’ as ‘down’ and vice versa). Thus UNOT gates do not allow Bob to retrieve information about $\vec{n}$ beyond standard quantum limits.

The consequences of the UNOT gate surface when an ancillary qubit is introduced. Consider the same game, but now played on two qubits. Instead of sending a single spin, Alice now sends a pair of spins. Take two different strategies, either (a) sending Bob two aligned spins, both in direction $\vec{n}$, or (b) an anti-aligned pair, with one spin in direction

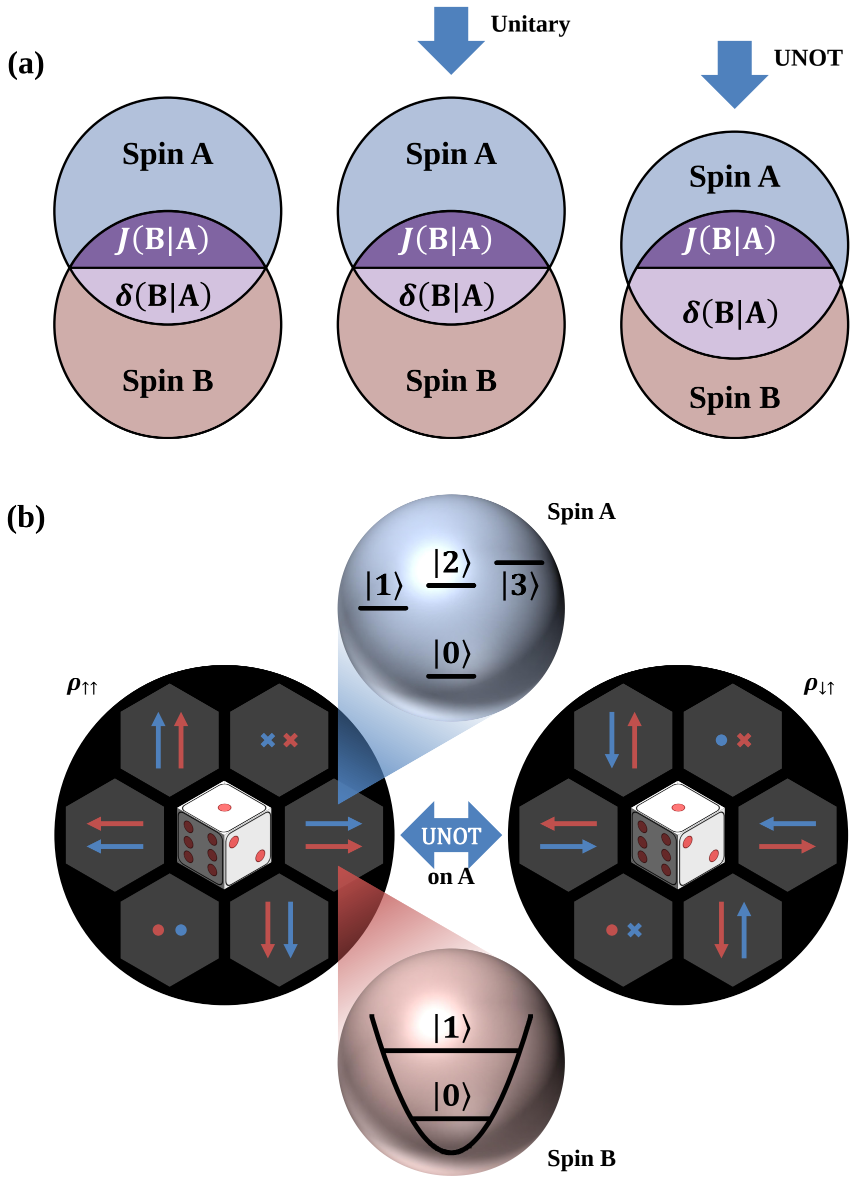

图 4.1　**UNOT gates on spin pairs.** (a) Local reversible operations leave classical correlations $J(\mathrm{B}|\mathrm{A})$ and quantum correlations $\delta(\mathrm{B}|\mathrm{A})$ unchanged, where A and B are two separable spins. A UNOT gate also preserves $J(\mathrm{B}|\mathrm{A})$, but can change $\delta(\mathrm{B}|\mathrm{A})$. (b) We simulate the effect of UNOT on $\rho_{\uparrow\uparrow}$ and $\rho_{\downarrow\uparrow}$, where the two spins are encoded in the internal and external degrees of freedom of a trapped $^{171}\mathrm{Yb}^{+}$ ion in a harmonic potential. Spin A is mapped to a 4-level system using Eq. (4-1), spanned by the basis $|0_\mathrm{A}\rangle = |F = 0, m_\mathrm{F} = 0\rangle$ and $|(n = 1, 2, 3)_\mathrm{A}\rangle = |F = 1, m_\mathrm{F} = n - 2\rangle$, where F and m_F characterize the total internal angular momentum of $^{171}\mathrm{Yb}^{+}$. The transition frequency from $|F = 0, m_\mathrm{F} = 0\rangle$ to $|F = 1, m_\mathrm{F}\rangle$ is $(2\pi)(12642.8 + 9.0m_\mathrm{F})$ MHz. Spin B is mapped to the ground and first excited states of external motional mode, denoted by $|0_\mathrm{B}\rangle$ and $|1_\mathrm{B}\rangle$, which are separated by the trap frequency $(2\pi)2.44$ MHz.

$\vec{n}$, and the other in direction $-\vec{n}$. Gisin and Popescu illustrated that the second strategy improves Bob's capacity to estimate $\vec{n}$[21]. They noted that if Bob possesses a UNOT gate, he can deterministically convert a pair of aligned spins to anti-aligned spins, and thus break standard quantum limits whenever Alice adopts strategy (a).

This connection suggests that UNOT gate exhibits distinctive effects on quantum correlations. Here we formalize this intuition using recent methods that isolate the purely quantum component of correlations between two systems. These correlations, known as discord, are often motivated as correlations accessible only to quantum observers[28–30]. We show that the UNOT gate preserves classical correlations between two spins, but can change their shared quantum correlations in ways forbidden by fundamental data processing principles (see Fig. 4.1(a)). We illustrate this through experiment – by adapting recent ion trap technology that allows perfect simulation of anti-unitary operations[17,31,32]. We then outline how these results rationalize the discrepancy in communication rate between aligned and anti-aligned spins, showing that it exactly relates to the UNOT gate's non-trivial effect on discord during the decoding process.

4.2 Theory

4.2.1 Technical framework

Consider first two classical spins A and B. Let $S(\cdot)$ denote the information entropy function, such that $S(\mathrm{A})$ and $S(\mathrm{B})$ quantify the respective uncertainties of A and B when viewed independently and $S(\mathrm{AB})$ the uncertainty of the joint spin pair. The mutual information $I(\mathrm{A},\mathrm{B}) = S(\mathrm{A}) + S(\mathrm{B}) - S(\mathrm{AB})$ then captures the total correlations between A and B. This coincides with $J(\mathrm{B}|\mathrm{A}) = S(\mathrm{B}) - S(\mathrm{B}|\mathrm{A})$, the reduction of uncertainty in B, when someone measures and communicates the state of A. The *data processing inequality* implies that $I(\mathrm{A},\mathrm{B})$ can never increase under local operations[1,33]. This reflects the principle that we can never spontaneously obtain more information about a spatially separated system B through local operations on A. Consequently, any reversible operation on A must conserve $I(\mathrm{A},\mathrm{B})$ – a condition clearly satisfied by the classical NOT gate.

When the two spins are quantum, the analogues of $I(\mathrm{A},\mathrm{B})$ and $J(\mathrm{B}|\mathrm{A})$ no longer coincide. Any positive operator valued measurements (POVMs) $\{\Pi_a\}$ on A can induce unavoidable noise, limiting the entropy reduction on B to $J(\mathrm{B}|\mathrm{A}) = \sup_{\{\Pi_a\}}\left[S(\mathrm{B}) - \sum_a p_a S(\mathrm{B}|a)\right]$, where p_a is the probability of getting outcome a, and $S(\mathrm{B}|a)$ represents the corresponding entropy of B conditioned on this outcome. In literature, $J(\mathrm{B}|\mathrm{A})$ is considered to be the classical component of $I(\mathrm{A},\mathrm{B})$, as it represents how much information a *classical observer* can gain about B when measuring A. The remaining portion, $\delta(\mathrm{B}|\mathrm{A}) = I(\mathrm{A},\mathrm{B}) - J(\mathrm{B}|\mathrm{A})$, is defined as the quantum discord, and interpreted as the purely quantum correlations between A and B [28,30,34–36].

4.2.2 Theoretical results

Let ρ be a separable bipartite state on two spins, A and B. Here we establish the following relations between the UNOT gate and classical and quantum correlations:

(i) Local UNOT gates preserve $J(\mathrm{B}|\mathrm{A})$ and $J(\mathrm{A}|\mathrm{B})$.

(ii) If $\delta(\mathrm{B}|\mathrm{A}) = 0$, a local UNOT gate conserves $I(\mathrm{A},\mathrm{B})$.

(iii) Local UNOT gates can nevertheless violate the data processing inequality, but only when $\delta(\mathrm{B}|\mathrm{A}) > 0$.

Result (i) implies that the UNOT gate can never break the data processing inequality for classical correlations. A classical observer that quantifies correlations by local measurement (i.e., $J(\mathrm{A}|\mathrm{B})$ or $J(\mathrm{B}|\mathrm{A})$) will conclude that the UNOT gate has no radical effects. Meanwhile result (ii) implies that the UNOT gate always obeys the data processing inequality, provided no discord is present. Finally result (iii) shows that the UNOT gate can violate the data processing inequality, but only when discord is present. Furthermore, this violation can only be witnessed when purely quantum correlations are taken into account. We demonstrate (iii) directly by explicit examples in the next section, while proofs for (i) and (ii) are given below.

4.2.2.1 Proof of result (i)

Note first that as ρ is separable, it can be written in the form

$$\rho = \sum_i p_i \left|\varphi_i\right\rangle \left\langle\varphi_i\right| \otimes \left|\phi_i\right\rangle \left\langle\phi_i\right| .$$

Note also that $J(\mathrm{B}|\mathrm{A})$ is asymmetric. Thus we consider the cases where UNOT gate on spin A and spin B separately.

When the UNOT gate is applied to A, the state is transformed to

$$\rho^{\mathrm{o}} = \sum_i p_i \left|\varphi_i^{\perp}\right\rangle \left\langle\varphi_i^{\perp}\right| \otimes \left|\phi_i\right\rangle \left\langle\phi_i\right| ,$$

where $|\varphi_i^{\perp}\rangle$ satisfies $\langle\varphi_i|\varphi_i^{\perp}\rangle = 0$. Let $J^{\mathrm{o}}(\mathrm{B}|\mathrm{A})$ and $\delta^{\mathrm{o}}(\mathrm{B}|\mathrm{A})$ denote the resulting classical and quantum correlations in ρ^{o}. Recall also that the definition of $J(\mathrm{B}|\mathrm{A})$ involves an optimization over the measurement basis for A. For a given rank-1 POVM, $\{\Pi_a\}$, consider the basis-dependent classical correlations $J_{\{\Pi_a\}}(\mathrm{B}|\mathrm{A}) = S(\mathrm{B}) - \sum_a p_a S(\mathrm{B}|a)$. We now introduce a second rank-1 POVM, $\{\Pi_a^{\perp}\}$, whose projective operators satisfy $\mathrm{tr}_{\mathrm{A}}(\Pi_a\Pi_a^{\perp}) = 0$. Thus $\mathrm{tr}_{\mathrm{A}}\left(\Pi_a|\varphi\rangle\langle\varphi|\right) = \mathrm{tr}_{\mathrm{A}}\left(\Pi_a^{\perp}|\varphi^{\perp}\rangle\langle\varphi^{\perp}|\right)$. Combining this relation with the definition of $J_{\{\Pi_a\}}(\mathrm{B}|\mathrm{A})$, one obtains $J_{\{\Pi_a\}}(\mathrm{B}|\mathrm{A}) = J^{\mathrm{o}}_{\{\Pi_a^{\perp}\}}(\mathrm{B}|\mathrm{A})$. Note that $J(\mathrm{B}|\mathrm{A}) = \sup_{\{\Pi_a\}}\left[J_{\{\Pi_a\}}(\mathrm{B}|\mathrm{A})\right]$, then it follows that $J^{\mathrm{o}}(\mathrm{B}|\mathrm{A}) = J(\mathrm{B}|\mathrm{A})$. Thus $J(\mathrm{B}|\mathrm{A})$ is preserved.

Consider now the case where the UNOT operation is applied to B. Note that the UNOT gate preserves the entropy of any single spin state, in particular when the UNOT operation is applied to B, both $S(\mathrm{B})$ and $S(\mathrm{B}|a)$ are preserved. Thus, since $J_{\{\Pi_a\}}(\mathrm{B}|\mathrm{A}) = S(\mathrm{B}) - \sum_a p_a S(\mathrm{B}|a)$, the UNOT gate preserves $J_{\{\Pi_a\}}(\mathrm{B}|\mathrm{A})$. Therefore $J(\mathrm{B}|\mathrm{A})$ is preserved.

4.2.2.2 Proof of result (ii)

Consider the situation where ρ has no discord, i.e., $\delta(\mathrm{B}|\mathrm{A}) = 0$. Thus ρ is a quantum-classical state, which takes the form $\rho = \sum_{i=0}^{1} p_i |i\rangle\langle i| \otimes \rho_i$, with $\{|i\rangle\}_{i=0,1}$ being an orthogonal basis. The mutual information between A and B is given by $I(\mathrm{A},\mathrm{B}) = S\left(\sum_{i=0}^{1} p_i\rho_i\right) - \sum_{i=0}^{1} p_i S(\rho_i)$.

If we apply a UNOT gate to A, we transform the state to $\rho^{\mathrm{o}} = \sum_{i=0}^{1} p_i |i\oplus 1\rangle\langle i\oplus 1| \otimes \rho_i$. Clearly, the mutual information of ρ^{o} is still $I(\mathrm{A},\mathrm{B})$. If we apply a UNOT gate to B, both $S\left(\sum_{i=0}^{1} p_i\rho_i\right)$ and $S(\rho_i)$ are preserved. Thus $I(\mathrm{A},\mathrm{B})$ remains unchanged.

4.3 Experiment

4.3.1 Protocol

Our experiment considers a separable bipartite quantum state $\rho_{\downarrow\uparrow}$ constructed as follows: first let $\mathcal{I} = \{\vec{x}, -\vec{x}, \vec{y}, -\vec{y}, \vec{z}, -\vec{z}\}$ represent a set of six standard coordinate directions in 3-dimensional space. We select a direction $\vec{n} \in \mathcal{I}$ uniformly at random, and prepare one spin aligned in direction $-\vec{n}$ and the other in $\vec{n}$. Denote their states respectively by $|-\vec{n}_{\mathrm{A}}\rangle$ and $|\vec{n}_{\mathrm{B}}\rangle$. The choice of $\vec{n}$ is then discarded. The resulting mixed state $\rho_{\downarrow\uparrow} = \sum_{\vec{n}\in\mathcal{I}} |-\vec{n}_{\mathrm{A}}, \vec{n}_{\mathrm{B}}\rangle\langle -\vec{n}_{\mathrm{A}}, \vec{n}_{\mathrm{B}}|/6$ then describes two anti-aligned spins that are oriented along one of the six directions in $\mathcal{I}$ at random. Application of the UNOT gate

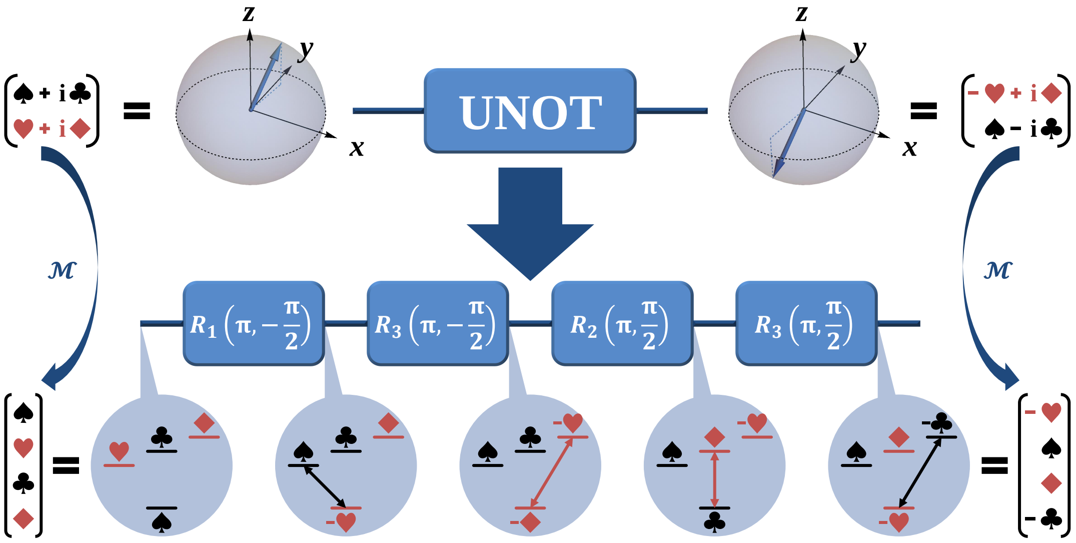
♠ + i♣
♥ + i♦
z
y
x
UNOT
z
y
x
-♥ + i♦
♠ - i♣
$\mathcal{M}$
$\mathcal{M}$
$R_1\left(\pi,-\frac{\pi}{2}\right)$
$R_3\left(\pi,-\frac{\pi}{2}\right)$
$R_2\left(\pi,\frac{\pi}{2}\right)$
$R_3\left(\pi,\frac{\pi}{2}\right)$
♠
♥
♣
♦
-♥
♠
♦
-♣

图 4.2　**Simulation of UNOT Gate on encoded spin A.** While the UNOT gate is unphysical, it can be exactly simulated using a quantum 4-level system. To simulate UNOT acting on state $|\varphi\rangle = \alpha|\uparrow\rangle + \beta|\downarrow\rangle$, we initialize a suitable state $|\bar{\varphi}\rangle = \mathcal{M}|\varphi\rangle$ on the 4-level system (see Eq. (4-1)). The expected output state $|\varphi^{\perp}\rangle = \Theta_{\mathrm{UNOT}}|\varphi\rangle = -\beta^{*}|\uparrow\rangle + \alpha^{*}|\downarrow\rangle$ can then be simulated by applying $\bar{\Theta}_{\mathrm{UNOT}} = |1\rangle\langle 0| - |0\rangle\langle 1| - |3\rangle\langle 2| + |2\rangle\langle 3|$ on $|\bar{\varphi}\rangle$. It is easy to check that $\bar{\Theta}_{\mathrm{UNOT}}|\bar{\varphi}\rangle = \mathcal{M}|\varphi^{\perp}\rangle$. In the ion trap system, $\bar{\Theta}_{\mathrm{UNOT}}$ can be realized with 4 microwave pulses, where $R_n(\pi,\phi) = -i\left(e^{-i\phi}|n_{\mathrm{A}}\rangle\langle 0_{\mathrm{A}}| + \mathrm{h.c.}\right) + \sum_{m\neq 0,n}|m_{\mathrm{A}}\rangle\langle m_{\mathrm{A}}|$, $n = 1, 2, 3$.

on one of the two spins then results in the state $\rho_{\uparrow\uparrow} = \sum_{\vec{n}\in\mathcal{I}}|\vec{n}_{\mathrm{A}},\vec{n}_{\mathrm{B}}\rangle\langle\vec{n}_{\mathrm{A}},\vec{n}_{\mathrm{B}}|/6$ which represents two aligned spins oriented randomly in some direction $\vec{n}\in\mathcal{I}$ (see Fig. 4.1(b)). By result (i), $\rho_{\uparrow\uparrow}$ and $\rho_{\downarrow\uparrow}$ must have coinciding classical correlations $J(\mathrm{B}|\mathrm{A})$.

Here we conduct two separate experiments. In the first, we prepare $\rho_{\downarrow\uparrow}$ on a spin pair, and simulate the action of the UNOT gate on one of the two spins. We characterize, by tomography, the effect of this action on the classical and quantum correlations within the spin pair. This process is then repeated with $\rho_{\uparrow\uparrow}$ in place of $\rho_{\downarrow\uparrow}$. This allows us to experimentally demonstrate result (iii) by showing that the local application of a UNOT gate can fundamentally increase or decrease $\delta(\mathrm{B}|\mathrm{A})$ while preserving $J(\mathrm{B}|\mathrm{A})$, and thus violate the data processing inequality.

4.3.2 Experimental methods

4.3.2.1 Simulating UNOT

The experiment involves exact simulation of the UNOT gate – an unphysical operation. Indeed, all existing demonstrations of the UNOT gate are based on theoretically optimal approximations[25,26]. We circumvent these issues by embedding the state of spin A within a larger Hilbert space (see Fig. 4.2) – a technique recently proposed for exactly simulating anti-unitary operations[31,32]. This approach maps each spin state $|\varphi\rangle = \alpha\,|\uparrow\rangle + \beta\,|\downarrow\rangle$ to a corresponding state

$$\mathcal{M}\,|\varphi\rangle = |\bar{\varphi}\rangle = \alpha_{\mathrm{R}}\,|0\rangle + \beta_{\mathrm{R}}\,|1\rangle + \alpha_{\mathrm{I}}\,|2\rangle + \beta_{\mathrm{I}}\,|3\rangle \tag{4-1}$$

on some 4-level quantum system, where $\alpha = \alpha_{\mathrm{R}} + i\alpha_{\mathrm{I}}$ and $\beta = \beta_{\mathrm{R}} + i\beta_{\mathrm{I}}$, and $|n = 0, 1, 2, 3\rangle$ denotes some orthogonal basis. The action of the UNOT gate can then be simulated by a suitable unitary operator on the 4-level system.

4.3.2.2 Encoding

We use a trapped $^{171}\mathrm{Yb}^{+}$ ion in a harmonic potential[17]. Spin B is encoded within the ground and first excited external motional states of the ion, denoted $|0_{\mathrm{B}}\rangle$ and $|1_{\mathrm{B}}\rangle$. Meanwhile spin A is encoded within the four internal degrees of freedom of the trapped ion using the aforemention technique (see Fig. 4.1(b)).

4.3.2.3 Microwave

We manipulate the internal states of $^{171}\mathrm{Yb}^{+}$ by microwave operations which drive transitions $|0_{\mathrm{A}}\rangle \leftrightarrow |(n = 1, 2, 3)_{\mathrm{A}}\rangle$ resonantly, allowing synthesis of the unitary operations

$$R_n(\chi, \phi) = \exp\left[-i\frac{\chi}{2}\left(e^{-i\phi}\,|n_{\mathrm{A}}\rangle\,\langle 0_{\mathrm{A}}| + \mathrm{h.c.}\right)\right] \tag{4-2}$$

for arbitrary χ and ϕ[32,37]. This allows us to simulate any unitary or anti-unitary operation on spin A. In particular, we develop an explicit pulse sequence for simulating the UNOT gate as shown in Fig. 4.2.

Population of the internal state $|0_{\mathrm{A}}\rangle$ can be directly measured by standard fluorescence detection and detection error correction[38]. Population of any other internal state $|n_{\mathrm{A}}\rangle$ can be measured by first transferring it to $|0_{\mathrm{A}}\rangle$ via the microwave operation $R_n(\pi, \phi)$.

4.3.2.4 Red sideband

We manipulate the external motional degrees of freedom via the red sideband, a standard Raman operation[17] that synthesizes the unitary

$$R_{-}(\chi, \phi) = \exp\left[\frac{\chi}{2}\left(e^{-i\phi}\sigma_{+}a - e^{i\phi}\sigma_{-}a^{\dagger}\right)\right]. \tag{4-3}$$

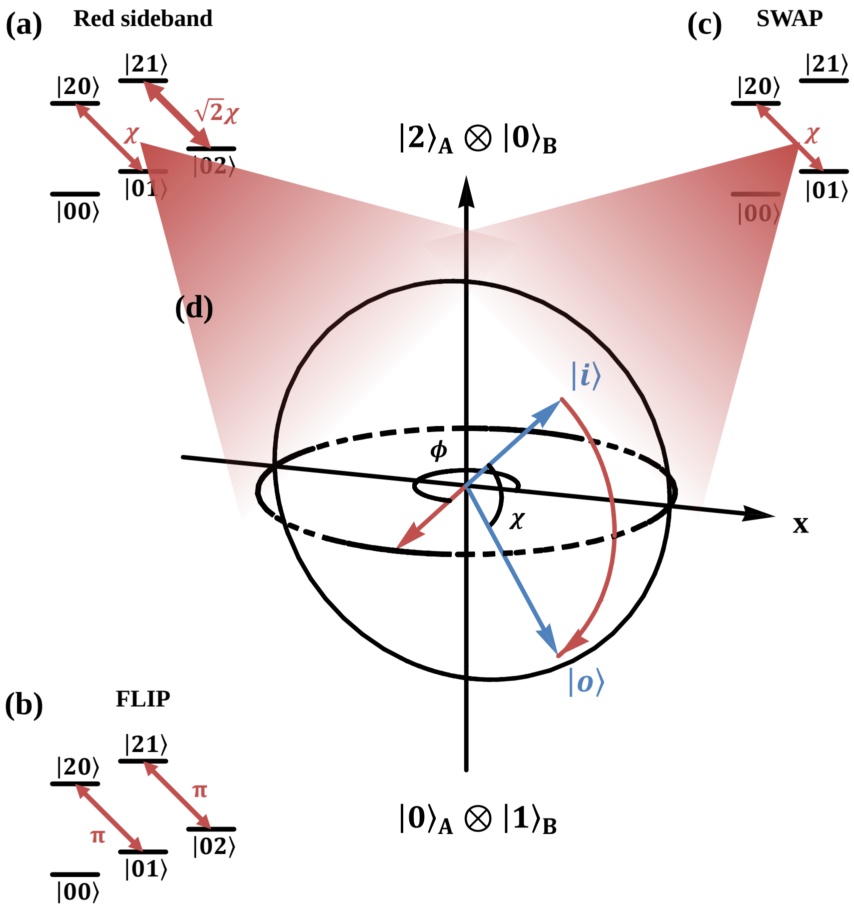

图 4.3　**Effects of external levels involved operations.** (a)(b)(c) The effects of the red sideband, FLIP and SWAP operations on low motional energy levels. (d) The graphic description of transition $|0_A1_B\rangle \leftrightarrow |2_A0_B\rangle$ caused by $R_-(\chi,\phi)$ or $R_{\mathrm{SWAP}}(\chi,\phi)$.

表 4.1　**Pulse sequences of FLIP and SWAP operations.** In the SWAP operation, $\alpha = \arccos\left[\csc(\pi/\sqrt{2})\sin(\chi/4)\right]$ and $\gamma = \phi - \arccos\left[\cot(\pi/\sqrt{2})\tan(\chi/4)\right]$.

Operation	Sequence
$R_{\mathrm{FLIP}}(\phi)$	$R_-(\pi/2,\phi)$, $R_-(\pi/\sqrt{2},\phi+\pi/2)$, $R_-(\pi/2,\phi)$
$R_{\mathrm{SWAP}}(\chi,\phi)$	$R_-(\pi/\sqrt{2},\gamma)$, $R_-(\sqrt{2}\pi,2\alpha+\gamma)$, $R_-(\pi/\sqrt{2},\gamma)$

Here, $\sigma_+ = |2_A\rangle\langle 0_A|$ and $\sigma_- = |0_A\rangle\langle 2_A|$, while a and $a^\dagger$ are the annihilation and creation operators with respect to system B. The red sideband operation drives transitions $|0_A(m+1)_B\rangle \leftrightarrow |2_Am_B\rangle$ with transition rates depending on $m = 0, 1, 2, \cdots$.

4.3.2.5　FLIP

The population of $|0_A1_B\rangle$ can also be probed by measuring the population of $|0_A\rangle$, after suitable pre-processing. This is done by first developing a FLIP operation that instigates π transitions for both $|0_A1_B\rangle \leftrightarrow |2_A0_B\rangle$ and $|0_A2_B\rangle \leftrightarrow |2_A1_B\rangle$[39–41]. In our protocol, motional levels with $m \geq 2$ are unpopulated. Thus measuring the population of $|2_\mathrm{A}\rangle$ after application of the FLIP operation reveals the the population of $|0_\mathrm{A}1_\mathrm{B}\rangle$.

The FLIP operation is composed of 3 red sideband pulses as shown in Tab. 4.1. Its effect shown in Fig. 4.3(b) can be described as following

$$\begin{aligned}
R_\mathrm{FLIP}(\phi)\,|0_\mathrm{A}0_\mathrm{B}\rangle &= |0_\mathrm{A}0_\mathrm{B}\rangle\,, \\
R_\mathrm{FLIP}(\phi)\,|0_\mathrm{A}1_\mathrm{B}\rangle &= |2_\mathrm{A}0_\mathrm{B}\rangle\, e^{-i\left(\phi+\frac{\pi}{2\sqrt{2}}\right)}, \\
R_\mathrm{FLIP}(\phi)\,|0_\mathrm{A}2_\mathrm{B}\rangle &= |2_\mathrm{A}1_\mathrm{B}\rangle\, e^{-i\left(\phi+\frac{\pi}{2}\right)}, \\
R_\mathrm{FLIP}(\phi)\,|1_\mathrm{A}m_\mathrm{B}\rangle &= |1_\mathrm{A}m_\mathrm{B}\rangle\,, \\
R_\mathrm{FLIP}(\phi)\,|2_\mathrm{A}0_\mathrm{B}\rangle &= |0_\mathrm{A}1_\mathrm{B}\rangle\, e^{i\left(\phi+\frac{\pi}{2\sqrt{2}}\right)}, \\
R_\mathrm{FLIP}(\phi)\,|2_\mathrm{A}1_\mathrm{B}\rangle &= |0_\mathrm{A}2_\mathrm{B}\rangle\, e^{i\left(\phi+\frac{\pi}{2}\right)}, \\
R_\mathrm{FLIP}(\phi)\,|3_\mathrm{A}m_\mathrm{B}\rangle &= |3_\mathrm{A}m_\mathrm{B}\rangle\,,
\end{aligned} \tag{4-4}$$

where $m = 0, 1, 2, \cdots$.

4.3.2.6 SWAP

To measure the population of general $|n_\mathrm{A}m_\mathrm{B}\rangle$, we develop a generalized version of the SWAP gate of Ref.[39], which is able to drive $|0_\mathrm{A}1_\mathrm{B}\rangle$ to arbitrary superposition state of $|0_\mathrm{A}1_\mathrm{B}\rangle$ and $|2_\mathrm{A}0_\mathrm{B}\rangle$, while preserving the populations of $|0_\mathrm{A}0_\mathrm{B}\rangle$ and $|2_\mathrm{A}1_\mathrm{B}\rangle$. This allows us to transfer the population of any general $|n_\mathrm{A}m_\mathrm{B}\rangle$ to state $|0_\mathrm{A}1_\mathrm{B}\rangle$ with combined sequence of microwave and SWAP operations.

We develop the SWAP operation with 3 red sideband pulses as shown in Tab. 4.1. The Fig. 4.3(c) shows the effect of SWAP described as following

$$\begin{aligned}
R_\mathrm{SWAP}(\chi,\phi)\,|0_\mathrm{A}0_\mathrm{B}\rangle &= |0_\mathrm{A}0_\mathrm{B}\rangle\,, \\
R_\mathrm{SWAP}(\chi,\phi)\,|0_\mathrm{A}1_\mathrm{B}\rangle &= |0_\mathrm{A}1_\mathrm{B}\rangle\cos\frac{\chi}{2} + |2_\mathrm{A}0_\mathrm{B}\rangle\sin\frac{\chi}{2}e^{-i\phi}, \\
R_\mathrm{SWAP}(\chi,\phi)\,|1_\mathrm{A}m_\mathrm{B}\rangle &= |1_\mathrm{A}m_\mathrm{B}\rangle\,, \\
R_\mathrm{SWAP}(\chi,\phi)\,|2_\mathrm{A}0_\mathrm{B}\rangle &= |2_\mathrm{A}0_\mathrm{B}\rangle\cos\frac{\chi}{2} - |0_\mathrm{A}1_\mathrm{B}\rangle\sin\frac{\chi}{2}e^{i\phi}, \\
R_\mathrm{SWAP}(\chi,\phi)\,|3_\mathrm{A}m_\mathrm{B}\rangle &= |3_\mathrm{A}m_\mathrm{B}\rangle\,,
\end{aligned} \tag{4-5}$$

where $m = 0, 1, 2, \cdots$.

表 4.2 **Preparation of aligned or anti-aligned spin pairs in 6 directions.** We obtain the 5th pair $|0_A 0_B\rangle$ by standard sideband cooling process. Other 11 pairs are generated from $|0_A 0_B\rangle$ with corresponding sequences in the right column.

Spin pair	Encoded form	Sequence
$\lvert\vec{x}_A, \vec{x}_B\rangle$	$(\lvert 0_A\rangle + \lvert 1_A\rangle)(\lvert 0_B\rangle + \lvert 1_B\rangle)/2$	$R_2(\pi/2, \pi/2)$, $R_-(\pi, 0)$, $R_1(\pi/2, -\pi/2)$
$\lvert -\vec{x}_A, -\vec{x}_B\rangle$	$(\lvert 0_A\rangle - \lvert 1_A\rangle)(\lvert 0_B\rangle - \lvert 1_B\rangle)/2$	$R_2(\pi/2, -\pi/2)$, $R_-(\pi, 0)$, $R_1(\pi/2, \pi/2)$
$\lvert\vec{y}_A, \vec{y}_B\rangle$	$(\lvert 0_A\rangle + \lvert 3_A\rangle)(\lvert 0_B\rangle + i\lvert 1_B\rangle)/2$	$R_2(\pi/2, 0)$, $R_-(\pi, 0)$, $R_3(\pi/2, -\pi/2)$
$\lvert -\vec{y}_A, -\vec{y}_B\rangle$	$(\lvert 0_A\rangle - \lvert 3_A\rangle)(\lvert 0_B\rangle - i\lvert 1_B\rangle)/2$	$R_2(\pi/2, \pi)$, $R_-(\pi, 0)$, $R_3(\pi/2, \pi/2)$
$\lvert\vec{z}_A, \vec{z}_B\rangle$	$\lvert 0_A 0_B\rangle$	
$\lvert -\vec{z}_A, -\vec{z}_B\rangle$	$\lvert 1_A 1_B\rangle$	$R_2(\pi, 0)$, $R_-(\pi, 0)$, $R_1(\pi, 0)$
$\lvert -\vec{x}_A, \vec{x}_B\rangle$	$(\lvert 0_A\rangle - \lvert 1_A\rangle)(\lvert 0_B\rangle + \lvert 1_B\rangle)/2$	$R_2(\pi/2, \pi/2)$, $R_-(\pi, 0)$, $R_1(\pi/2, \pi/2)$
$\lvert\vec{x}_A, -\vec{x}_B\rangle$	$(\lvert 0_A\rangle + \lvert 1_A\rangle)(\lvert 0_B\rangle - \lvert 1_B\rangle)/2$	$R_2(\pi/2, -\pi/2)$, $R_-(\pi, 0)$, $R_1(\pi/2, -\pi/2)$
$\lvert -\vec{y}_A, \vec{y}_B\rangle$	$(\lvert 0_A\rangle - \lvert 3_A\rangle)(\lvert 0_B\rangle + i\lvert 1_B\rangle)/2$	$R_2(\pi/2, 0)$, $R_-(\pi, 0)$, $R_3(\pi/2, \pi/2)$
$\lvert\vec{y}_A, -\vec{y}_B\rangle$	$(\lvert 0_A\rangle + \lvert 3_A\rangle)(\lvert 0_B\rangle - i\lvert 1_B\rangle)/2$	$R_2(\pi/2, \pi)$, $R_-(\pi, 0)$, $R_3(\pi/2, -\pi/2)$
$\lvert -\vec{z}_A, \vec{z}_B\rangle$	$\lvert 1_A 0_B\rangle$	$R_1(\pi, -\pi/2)$
$\lvert\vec{z}_A, -\vec{z}_B\rangle$	$\lvert 0_A 1_B\rangle$	$R_2(\pi, \pi/2)$, $R_-(\pi, 0)$

4.3.2.7 Preparation of spin pair

We prepare $\rho_{\uparrow\uparrow}$ or $\rho_{\downarrow\uparrow}$ by deterministically creating pure spin pairs in 6 directions and equally averaging them. The original form, encoded form and the preparation sequence of each spin pair are shown in Tab. 4.2.

4.3.2.8 Tomography of spin pair

To reconstruct the spin pair into a density operator

$$\rho = \begin{pmatrix} z_0 & x_{0,1} - iy_{0,1} & x_{0,2} - iy_{0,2} & x_{0,3} - iy_{0,3} \\ x_{0,1} + iy_{0,1} & z_1 & x_{1,2} - iy_{1,2} & x_{1,3} - iy_{1,3} \\ x_{0,2} + iy_{0,2} & x_{1,2} + iy_{1,2} & z_2 & x_{2,3} - iy_{2,3} \\ x_{0,3} + iy_{0,3} & x_{1,3} + iy_{1,3} & x_{2,3} + iy_{2,3} & z_3 \end{pmatrix} \tag{4-6}$$

with basis $|\uparrow_A\uparrow_B\rangle$, $|\uparrow_A\downarrow_B\rangle$, $|\downarrow_A\uparrow_B\rangle$ and $|\downarrow_A\downarrow_B\rangle$, we employ quantum state tomography by measuring $\langle\psi|\,\rho\,|\psi\rangle$ with several choices of $|\psi\rangle$.

In experiment, ρ is encoded as $\bar{\rho} = \mathcal{M}\rho\mathcal{M}^\dagger$. To interpret $\langle\psi|\,\rho\,|\psi\rangle$, we derive the

表 4.3 **Information of the measurements in the tomography.** We measure each population $P = \langle\psi\rvert \rho \lvert\psi\rangle /2 = \langle\bar{\psi}\rvert \bar{\rho} \lvert\bar{\psi}\rangle$ (see Eq. (4-8)) in the left column, where $\lvert\psi\rangle$ and $\lvert\bar{\psi}\rangle$ are listed in the middle and right column respectively.

Population P	state $\lvert\psi\rangle$	Measured state $\lvert\bar{\psi}\rangle$
$P_0 = z_0/2$	$\lvert\vec{z}_A, \vec{z}_B\rangle$	$(\lvert 0_A\rangle - i\lvert 2_A\rangle)\lvert 0_B\rangle/\sqrt{2}$
$P_1 = z_1/2$	$\lvert\vec{z}_A, -\vec{z}_B\rangle$	$(\lvert 0_A\rangle - i\lvert 2_A\rangle)\lvert 1_B\rangle/\sqrt{2}$
$P_2 = z_2/2$	$\lvert -\vec{z}_A, \vec{z}_B\rangle$	$(\lvert 1_A\rangle - i\lvert 3_A\rangle)\lvert 0_B\rangle/\sqrt{2}$
$P_3 = z_3/2$	$\lvert -\vec{z}_A, -\vec{z}_B\rangle$	$(\lvert 1_A\rangle - i\lvert 3_A\rangle)\lvert 1_B\rangle/\sqrt{2}$
$P_4 = (z_0 + z_1 + 2x_{0,1})/4$	$\lvert\vec{z}_A, \vec{x}_B\rangle$	$(\lvert 0_A\rangle - i\lvert 2_A\rangle)(\lvert 0_B\rangle + \lvert 1_B\rangle)/2$
$P_5 = (z_0 + z_1 + 2y_{0,1})/4$	$\lvert\vec{z}_A, \vec{y}_B\rangle$	$(\lvert 0_A\rangle - i\lvert 2_A\rangle)(\lvert 0_B\rangle + i\lvert 1_B\rangle)/2$
$P_6 = (z_0 + z_2 + 2x_{0,2})/4$	$\lvert\vec{x}_A, \vec{z}_B\rangle$	$(\lvert 0_A\rangle + \lvert 1_A\rangle - i\lvert 2_A\rangle - i\lvert 3_A\rangle)\lvert 0_B\rangle/2$
$P_7 = (z_0 + z_2 + 2y_{0,2})/4$	$\lvert\vec{y}_A, \vec{z}_B\rangle$	$(\lvert 0_A\rangle + i\lvert 1_A\rangle - i\lvert 2_A\rangle + \lvert 3_A\rangle)\lvert 0_B\rangle/2$
$P_8 = (z_0 + z_3 + 2x_{0,3})/4$	$(\lvert\uparrow_A, \uparrow_B\rangle + \lvert\downarrow_A, \downarrow_B\rangle)/\sqrt{2}$	$(\lvert 0_A 0_B\rangle + \lvert 1_A 1_B\rangle - i\lvert 2_A 0_B\rangle - i\lvert 3_A 1_B\rangle)/2$
$P_9 = (z_0 + z_3 - 2x_{0,3})/4$	$(\lvert\uparrow_A, \uparrow_B\rangle - \lvert\downarrow_A, \downarrow_B\rangle)/\sqrt{2}$	$(\lvert 0_A 0_B\rangle - \lvert 1_A 1_B\rangle - i\lvert 2_A 0_B\rangle + i\lvert 3_A 1_B\rangle)/2$
$P_{10} = (z_0 + z_3 + 2y_{0,3})/4$	$(\lvert\uparrow_A, \uparrow_B\rangle + i\lvert\downarrow_A, \downarrow_B\rangle)/\sqrt{2}$	$(\lvert 0_A 0_B\rangle + i\lvert 1_A 1_B\rangle - i\lvert 2_A 0_B\rangle + \lvert 3_A 1_B\rangle)/2$
$P_{11} = (z_1 + z_2 + 2x_{1,2})/4$	$(\lvert\uparrow_A, \downarrow_B\rangle + \lvert\downarrow_A, \uparrow_B\rangle)/\sqrt{2}$	$(\lvert 0_A 1_B\rangle + \lvert 1_A 0_B\rangle - i\lvert 2_A 1_B\rangle - i\lvert 3_A 0_B\rangle)/2$
$P_{12} = (z_1 + z_2 + 2y_{1,2})/4$	$(\lvert\uparrow_A, \downarrow_B\rangle + i\lvert\downarrow_A, \uparrow_B\rangle)/\sqrt{2}$	$(\lvert 0_A 1_B\rangle + i\lvert 1_A 0_B\rangle - i\lvert 2_A 1_B\rangle + \lvert 3_A 0_B\rangle)/2$
$P_{13} = (z_1 + z_3 + 2x_{1,3})/4$	$\lvert\vec{x}_A, -\vec{z}_B\rangle$	$(\lvert 0_A\rangle + \lvert 1_A\rangle - i\lvert 2_A\rangle - i\lvert 3_A\rangle)\lvert 1_B\rangle/2$
$P_{14} = (z_1 + z_3 + 2y_{1,3})/4$	$\lvert\vec{y}_A, -\vec{z}_B\rangle$	$(\lvert 0_A\rangle + i\lvert 1_A\rangle - i\lvert 2_A\rangle + \lvert 3_A\rangle)\lvert 1_B\rangle/2$
$P_{15} = (z_2 + z_3 + 2x_{2,3})/4$	$\lvert -\vec{z}_A, \vec{x}_B\rangle$	$(\lvert 1_A\rangle - i\lvert 3_A\rangle)(\lvert 0_B\rangle + \lvert 1_B\rangle)/2$
$P_{16} = (z_2 + z_3 + 2y_{2,3})/4$	$\lvert -\vec{z}_A . \vec{y}_B\rangle$	$(\lvert 1_A\rangle - i\lvert 3_A\rangle)(\lvert 0_B\rangle + i\lvert 1_B\rangle)/2$

decoding procedure

$$\mathcal{W} = \begin{pmatrix} 1 & & & & i & & & \\ & 1 & & & & i & & \\ & & 1 & & & & i & \\ & & & 1 & & & & i \end{pmatrix}, \tag{4-7}$$

which is the inverse of the encoding $\mathcal{M}$. Thus

$$\langle\psi\rvert \rho \lvert\psi\rangle = \langle\psi\rvert \mathcal{W}\bar{\rho}\mathcal{W}^\dagger \lvert\psi\rangle = 2\langle\bar{\psi}\rvert \bar{\rho} \lvert\bar{\psi}\rangle, \tag{4-8}$$

where $\lvert\bar{\psi}\rangle = \mathcal{W}^\dagger \lvert\psi\rangle/\sqrt{2}$. Each $\langle\bar{\psi}\rvert \bar{\rho} \lvert\bar{\psi}\rangle$ is obtained by population measurement with 1000 trials. We conduct this population measurement on 6 pure spin pairs from $\rho_{\uparrow\uparrow}$ or $\rho_{\downarrow\uparrow}$ with 17 choices of $\lvert\psi\rangle$ listed in the middle column of Tab. 4.3. In total, we reconstruct $\rho_{\uparrow\uparrow}$ or $\rho_{\downarrow\uparrow}$ with $6 \times 17 \times 1000 = 102000$ trials.

We note that

$$\begin{aligned} 2P_8 &= \langle\Phi^+|\,\rho\,|\Phi^+\rangle, \\ 2P_9 &= \langle\Phi^-|\,\rho\,|\Phi^-\rangle, \\ 2P_{11} &= \langle\Psi^+|\,\rho\,|\Psi^+\rangle, \\ 2(1-P_8-P_9-P_{11}) &= \langle\Psi^-|\,\rho\,|\Psi^-\rangle, \end{aligned} \tag{4-9}$$

where $|\Phi^+\rangle = (|\uparrow_A\uparrow_B\rangle + |\downarrow_A\downarrow_B\rangle)/\sqrt{2}$, $|\Phi^-\rangle = (|\uparrow_A\uparrow_B\rangle - |\downarrow_A\downarrow_B\rangle)/\sqrt{2}$, $|\Psi^+\rangle = (|\uparrow_A\downarrow_B\rangle + |\downarrow_A\uparrow_B\rangle)/\sqrt{2}$ and $|\Psi^-\rangle = (|\uparrow_A\downarrow_B\rangle - |\downarrow_A\uparrow_B\rangle)/\sqrt{2}$ are Bell states. Thus P_8, P_9 and P_{11} provide Bell-basis measurements for ρ.

We reconstruct the most probable density operator of $\rho_{\uparrow\uparrow}$ or $\rho_{\downarrow\uparrow}$ from the experimental data of P_j, subject to constraint that it is normalized ($z_0+z_1+z_2+z_3 = 1$) and non-negative definite. We determine the maximum likelihood of $\rho_{\uparrow\uparrow}$ or $\rho_{\downarrow\uparrow}$ by minimizing

$$\sum_{j=0}^{16} \frac{(P_j - P_j^{\mathrm{E}})^2}{2\Delta_j^2}, \tag{4-10}$$

where P_j^{E} is the experimental result of P_j, and Δ_j is the uncertainty of P_j^{E}. This objective function is obtained by maximizing the probability density

$$f(\rho) = \prod_{j=0}^{16} \frac{1}{\sqrt{2\pi}\sigma_j} \exp\left[-\frac{(P_j - P_j^{\mathrm{E}})^2}{2\sigma_j^2}\right], \tag{4-11}$$

supposing that each variable P_j follows a Gaussian distribution with mean P_j^{E} and standard deviation σ_j. Here we set $\Delta_j = 1.96\sigma_j$, corresponding to the confidence level of 95%.

4.3.3 Experimental results

We conduct two separate experimental tests. The first initializes $\rho_{\downarrow\uparrow}$, and determines how its classical and quantum correlations are affected by a UNOT operation on spin A. The second experiment repeats this process, using $\rho_{\uparrow\uparrow}$ in place of $\rho_{\downarrow\uparrow}$. The tomographic data of both cases are exhibited in Fig. 4.4. The experimentally reconstructed density operators agree with the theoretical predictions to high fidelity (see Fig. 4.5).

The experimentally observed effects of the UNOT gate on classical and quantum correlations are illustrated in Fig. 4.6. They confirm that the amount of classical correlations between A and B are preserved, in agreement with result (i). Meanwhile the

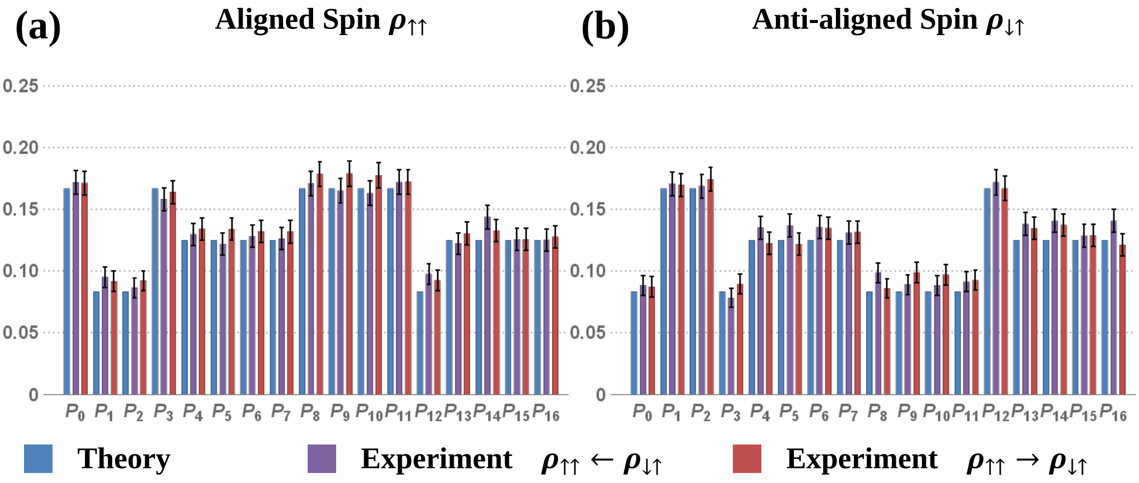

图 4.4 **The comparison between theoretical and experimental results of 17 population measurements** for (a) the aligned spin $\rho_{\uparrow\uparrow}$ and (b) the anti-aligned spin $\rho_{\downarrow\uparrow}$. The error bar of each quantity is calculated with confidence level of 95%.

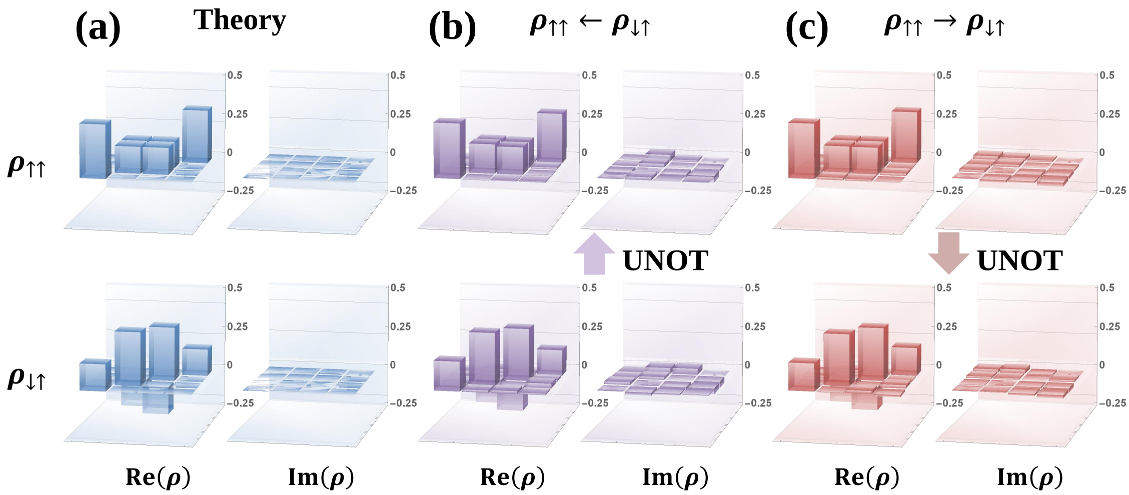

图 4.5 **Experimentally measured density operators compared with theoretical predictions.** (a) illustrates the theoretically predicted density operators for $\rho_{\uparrow\uparrow}$ and $\rho_{\downarrow\uparrow}$, where each vertical bar represents a corresponding matrix element. In the first experiment (b), $\rho_{\downarrow\uparrow}$ is prepared with a fidelity of 0.992 ± 0.004. After simulating the UNOT gate, we retrieve $\rho_{\uparrow\uparrow}$ with fidelity of 0.997 ± 0.007. In the second experiment (c), $\rho_{\uparrow\uparrow}$ is prepared with fidelity 0.998 ± 0.004, and the final state approximates $\rho_{\downarrow\uparrow}$ to fidelity 0.997 ± 0.002. The errors are estimated by Monte Carlo methods with a confidence level of 95%.

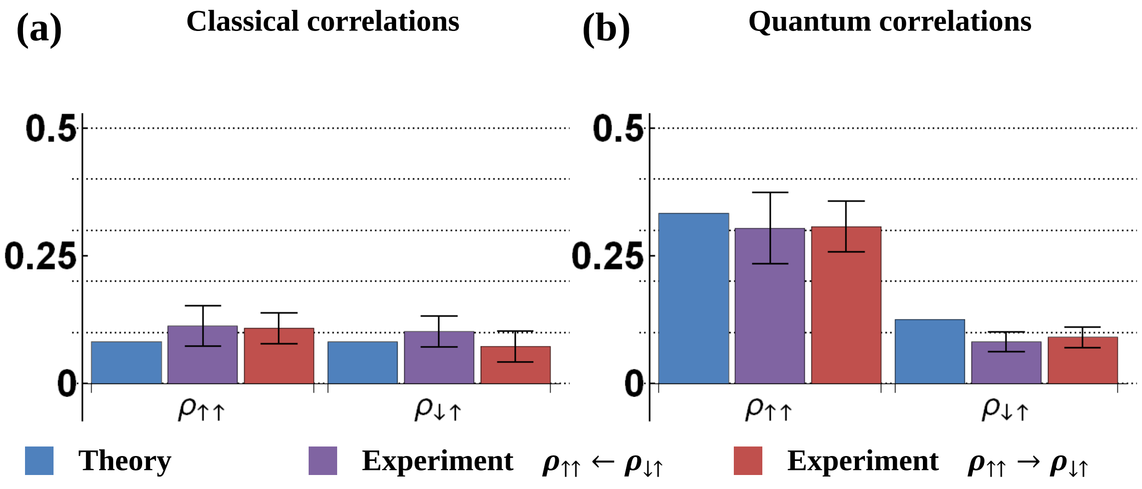

图 4.6　**The effect of UNOT gate on various types of correlations.** The theoretically predicted effect of UNOT gate (blue bars), together with experimentally measured effects when acting on $\rho_{\downarrow\uparrow}$ (purple bars) and $\rho_{\uparrow\uparrow}$ (red bars) are displayed for (a) classical correlations $J(\mathrm{B}|\mathrm{A})$ and (b) quantum correlations $\delta(\mathrm{B}|\mathrm{A})$. (a) Theory predicts that $J(\mathrm{B}|\mathrm{A}) = 0.082$ for both $\rho_{\uparrow\uparrow}$ and $\rho_{\downarrow\uparrow}$. Experimental results agree within experimental error. (b) Theory predicts that $\delta(\mathrm{B}|\mathrm{A})$ is 0.333 for $\rho_{\uparrow\uparrow}$ and 0.126 for $\rho_{\downarrow\uparrow}$ – a difference of 0.207. This agrees with the experiment, where we see respective increase and decrease of 0.22 ± 0.07 and 0.22 ± 0.05 when converting to and from $\rho_{\uparrow\uparrow}$.

application of UNOT on $\rho_{\downarrow\uparrow}$ increases quantum correlations by 0.22 ± 0.07, violating the data processing inequality by over 5 standard deviations and thus establishing (iii). The application of the UNOT gate on $\rho_{\uparrow\uparrow}$ can reverse this, inducing a decrease in $\delta(\mathrm{B}|\mathrm{A})$ of 0.22 ± 0.05.

4.4　Discussion

To conclude, we tie our results back to the communication advantage of using anti-aligned versus aligned spin pairs[21]. Specifically, consider the scenario where Alice encodes a classical message into two aligned spins, using the six possible codewords $\{|\vec{n}_{\mathrm{A}}, \vec{n}_{\mathrm{B}}\rangle\}_{\vec{n}\in\mathcal{I}}$ with equiprobability. The communication capacity is given by the Holevo quantity $\chi_{\uparrow\uparrow} = S(\rho_{\uparrow\uparrow})$, which bounds the amount of information Alice can communicate per spin pair[42]. This bound can always be saturated in the independent and identically distributed (i.i.d) limit, but never exceeded by conventional means.

Bob, however, can use a UNOT gate to surpass this bound. The rationale being that the capacity of such a channel $\chi_{\uparrow\uparrow} = S(\mathrm{A}) + S(\mathrm{B}) - I(\mathrm{A}, \mathrm{B})$ can be divided into $S(\mathrm{A}) + S(\mathrm{B})$, representing the amount of information A and B each individually communicate discounting correlations; and $I(\mathrm{A}, \mathrm{B})$, a correction term that captures how much of the aforementioned information is redundant. $I(\mathrm{A},\mathrm{B}) = J(\mathrm{B}|\mathrm{A}) + \delta(\mathrm{B}|\mathrm{A})$ can then be further divided into classical and quantum components. The UNOT gate, acting on $\rho_{\uparrow\uparrow}$, can uniquely reduce $\delta(\mathrm{B}|\mathrm{A})$, and thus reduce redundant information about $\vec{n}$ encoded in the two spins. The UNOT gate thereby boosts the amount of information Bob can extract. The performance gain is given by $\Delta\chi = \delta_{\uparrow\uparrow}(\mathrm{B}|\mathrm{A}) - \delta_{\downarrow\uparrow}(\mathrm{B}|\mathrm{A}) \approx 0.21$, where $\delta_{\uparrow\uparrow}$ and $\delta_{\downarrow\uparrow}$ respectively represent the discord of $\rho_{\uparrow\uparrow}$ and $\rho_{\downarrow\uparrow}$. This gain exactly coincides with the change in discord.

Observe also that Bob's application of the UNOT gate is functionally equivalent to Alice encoding the message in anti-aligned spins, i.e., using the codewords $\{|-\vec{n}_\mathrm{A}, \vec{n}_\mathrm{B}\rangle\}_{\vec{n}\in\mathcal{I}}$ in place of $\{|\vec{n}_\mathrm{A}, \vec{n}_\mathrm{B}\rangle\}_{\vec{n}\in\mathcal{I}}$. Thus, we see that the performance advantage of having UNOT gates exactly coincides with the performance discrepancy between using aligned vs. anti-aligned spins. Note also that this advantage only exists assuming Bob can measure in an entangling basis. This corroborates recent evidence that many operational effects of discord can only be accessed via entangling measurements[30,43,44]. That is, the UNOT only imparts unphysical effects on the quantum component of the correlations between two spins.

4.5 Conclusion

This work explores the UNOT gate's capacity to locally increase the correlations between spins, and thus break the data processing inequality. We establish that this gate shows no such capability in classical domain. It obeys the data processing inequality for all classically correlated systems. Furthermore, it preserves all classical correlations within general correlated quantum systems. Violation can only be witnessed when quantum correlations are explicitly considered. We adopt state of the art techniques for simulating anti-unitary operations to experimentally demonstrate this phenomena using a trapped $^{171}\mathrm{Yb}^+$ ion. A violation of the data processing inequality by over 5 standard deviations is observed. These results connect the unphysicality of the UNOT gate, its effect on quantum correlations, and the discrepancy in communicating using aligned versus anti-aligned spins. Our experiment then highlights how such unphysical effects can be simulated using present day ion trap technology.

There are a number of directions in which these results can generalize. Observe that the UNOT gate is equivalent, up to local unitary rotation, to any other anti-unitary operator on a qubit. The effect of UNOT gates on classical and quantum correlations thus also applies to any other anti-unitary operation. Meanwhile we may extend these ideas to systems of higher dimensions. For example, in optical systems, one can communicate more information using a conjugate pair of coherent states than using the same state twice[45]. This performance difference is likely due to an analogous effect of anti-unitary operations on bipartite Gaussian correlations.

Our results could also offer a new way to capture what classes of correlations are quantum. One could take as an axiom that states whose correlations change under the UNOT gate are quantum. The motivation being such effects field no classical explanation. Such an axiom would identify certain discordant states such as $\rho = (|\vec{x}_{\mathrm{A}}, \vec{x}_{\mathrm{B}}\rangle \langle\vec{x}_{\mathrm{A}}, \vec{x}_{\mathrm{B}}| + |\vec{z}_{\mathrm{A}}, \vec{z}_{\mathrm{B}}\rangle \langle\vec{z}_{\mathrm{A}}, \vec{z}_{\mathrm{B}}|)/2$ as more classical than others, since we can replicate the effect of a UNOT gate acting on them using only local unitary operations. This could well generalize to multi-partite systems, and present a general operational criterion for identifying quantum correlations residing somewhere between discord and entanglement.

第 5 章　Implementation of modular DQC1 in a trapped ion system

Modern computation relies crucially on modularity, the ability to break a computational routine down into myriad of self-contained subtasks that can be executed independently. A client can then call upon a remote server to implement parts of the computation autonomously, through an application programming interface (API). To date all such APIs have relayed classical information. Here we design an implement of quantum API to execute a modular power one pure qubit (DQC1) algorithm that computes certain properties of a server-provided unitary U. We demonstrate that the algorithm functions correctly irrespective of what unitary U the server implements or how the server specifically realizes U. Our realization involves pioneering techniques to coherently swap qubits encoded within motional states of a trapped $^{171}\mathrm{Yb}^{+}$ ion, controlled on its hyperfine state. This constitutes the first demonstration of modularity in the quantum regime, providing a step towards scalable, parallelization of quantum computation.

5.1 Introduction

When Google upgrades their hardware, applications that make use of Google services continue to operate without needing an update. This modular architecture plays an essential role in modern technology. It allows a client, Alice, to make use to computations done on a remote server, without knowing any details regarding how this computation was executed. Modularity is enabled by an interface – an established set of rules that specifies how Alice delivers input to the server, and how the server returns relevant output to Alice. Once agreed, Alice can design technology that makes use of the server's functions as subroutines, while remaining completely ignorant of their implementation. Such interfaces are now industry standard. Known as APIs (application programming interfaces), their adoption is almost universal – from specifying how we interface with graphics cards to the IBM quantum computer.

Existing interfaces assume server-client communication to be classical, limiting the scope of collaborative quantum computing. What happens if the server allows quantum information to be exchanged with the client? Consider the DQC1 algorithm that evaluates the normalized trace of a $2^n \times 2^n$ unitary matrix U in time polynomial of n[46,47]. Suppose now that a remote server features a quantum interface, such that it promises to return state $U|\psi\rangle$ whenever it is given a suitably encoded state $|\psi\rangle$. Could Alice construct a U-independent device that can harness this service to efficiently evaluate the normalized trace, $T(U) = \mathrm{tr}(U)/2^n$, of U? The benefits of this modular architecture are clear. It enables Alice to design a universal device that can efficiently probe the normalized trace of any unitary process. Alice can treat the server as a black-box. She need not know anything about the quantum circuits that synthesize U. In addition, Alice can use the same device to evaluate the normalized trace of some different U' by exchanging one server for another.

This is, in fact, impossible. To see this, note that $T(U)$ depends on the global phase of U - a quantity that is unphysical. Therefore if Alice could determine $T(U)$, she could measure an unphysical quantity. Indeed, recent works show that modular architectures in the quantum regime face significant restrictions, an iconic case being the impossibility of adding a control to an unknown unitary[48–50]. These results motivated recent work on restoring modularity to key quantum algorithms[50]. In the context of DQC1, the key observation is that while $T(U)$ depends on the global phase, its modulus does not. The resulting protocol – *modular* DQC1 – is a device that evaluates $|T(U)|$ by outsourcing implementation of U to an external party. In addition, the modular DQC1 algorithm could be chained together to construct a modular factoring algorithm – a variant of Shor's factoring algorithm that requires fewer entangling gates to realize the computational speedup[4].

Here we report the experimental implementation of the modular DQC1 algorithm in a trapped $^{171}\mathrm{Yb}^+$ ion system. We test this by successfully evaluating $|T(U)|$ for 19 different unitary operations. In each case, we illustrate that the only aspect of the quantum circuit that needs to be modified is on the side of the server – guaranteeing true modular architecture. The physical implementation involves pioneering techniques to realize a control-swap gate, which swaps two motional modes of an ion trapped in a 3D harmonic oscillator, controlled on the internal levels of the trapped ion. This thus presents the first demonstration of a modular quantum algorithm, where server and client are entangled, and provides the first step towards a fully modular quantum network. Meanwhile, our experimental techniques are scalable, enabling efficient pathway towards coherently swaping Hilbert spaces of exponentially growing dimensions.

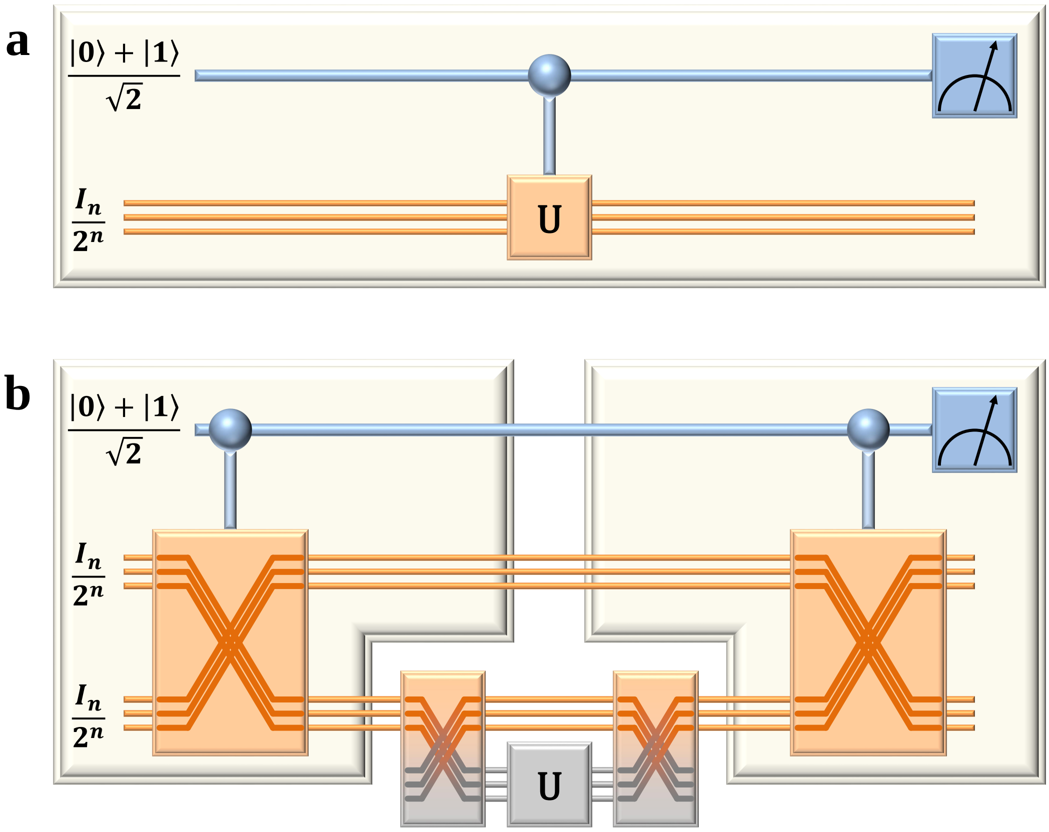
a
$\frac{|0\rangle+|1\rangle}{\sqrt{2}}$
$\frac{I_n}{2^n}$
U
b
$\frac{|0\rangle+|1\rangle}{\sqrt{2}}$
$\frac{I_n}{2^n}$
$\frac{I_n}{2^n}$
U

图 5.1　**The DQC1 and the modular DQC1.** (a) The standard DQC1 algorithm operates by applying U on an n-qubit register controlled by a pure qubit initialized in state $|0\rangle$. Measuring the expectation values of this control qubit with respect to standard Pauli operators $\sigma_1 = |0\rangle\langle 1| + |1\rangle\langle 0|$ and $\sigma_2 = i(|0\rangle\langle 1| - |1\rangle\langle 0|)$ then allows estimation of the real and imaginary components of the normalized trace $T(U)$. The action of U cannot be outsourced to an external server in a modular fashion. (b) Modular DQC1 evaluates $|T(U)|$ instead of $T(U)$ in way in which implementation of U can be out-sourced. In this protocol, Alice introduces a second n-qubit register and prepares ρ_1. She then sends the server one of the n-qubit registers (for example this may be realized by first mapping this register into a medium suitable for communication via a SWAP Gate). On the proviso that the server applies U to the register, she is able to estimate $|T(U)|$ by performing a σ_1 measurement on the control qubit.

5.2 Results

5.2.1 Framework

The modular DQC1 algorithm can be understood by dividing its actions into server and client. We first assume there exists a server, Bob, who offers the service of implementing an n-qubit unitary U. That is, Bob announces a quantum interface. The interface specifies that whenever someone sends Bob any state $|\psi\rangle$ encoded within some designated Hilbert space of a quantum system S, Bob will return a system S encoding $U|\psi\rangle$ within the same space. No other promises are made. Bob, for example, is not constrained to preserve information stored in any other degrees of freedom within S. Our goal is to take on the role of Alice, and build a device that employs Bob's services as a subroutine to evaluate $|T(U)|$.

To do this, Alice begins with a bipartite system, consisting of S to be delivered to Bob and some A that she retains for the duration of the protocol. The protocol then contains two distinct tasks (see Fig. 5.1(b)).

(i) *Preprocessing* – representing Alice's necessary actions of preparing some ρ_1 on the joint system system $A \otimes S$ before delivery of S to Bob

(ii) *Postprocessing* – representing Alice's actions to retrieve $|T(U)|$ from the state $\rho_2 = U\rho_1 U^\dagger$ after receiving Bob's output. Here U is represents the unitary process on S implemented by Bob.

Alice can achieve this by taking a single pure qubit initialized in state $|+\rangle = (|0\rangle + |1\rangle)/\sqrt{2}$, together with two maximally mixed n-qubit registers. In the *preprocessing* stage, she coherently swaps the two registers, controlled on the pure qubit to obtain ρ_1. Alice then forwards one of the registers to Bob via his specified quantum interface. Upon receipt of Bob's output, Alice enters the *postprocessing* stage. This involves a second application of the control swap operation mentioned above. Measurement of the ancilla in the σ_1 basis then has expectation value of $|T(U)|^2$, enabling efficient estimates of $|T(U)|$. Further details are shown in Fig. 5.1.

The combination of *preprocessing* and *postprocessing* constitutes the modular DQC1 protocol. Critically, neither procedure depends on the physical means that Bob chooses to realize U. For instance, Bob could initially implement U by applying physical operations directly on the system S. Alternatively, Bob could decide it is more efficient to map the received quantum state to an entirely new physical platform, and implement U on that platform. Alice's modular DQC1 protocol would function regardless. Moreover, Alice's *preprocessing* and *postprocessing* procedures are independent of which U Bob chooses to implement, or how Bob realizes this gate. Thus, the protocol also functions as a probe, able to efficiently estimate $|T(U)|^2$ for a completely unknown unitary process U.

5.2.2 Implementation

Here we construct a proof of principle realization of modular DQC1 using a trapped $^{171}\mathrm{Yb}^+$ ion in a harmonic potential when $n = 1$. In this special case, the protocol involves

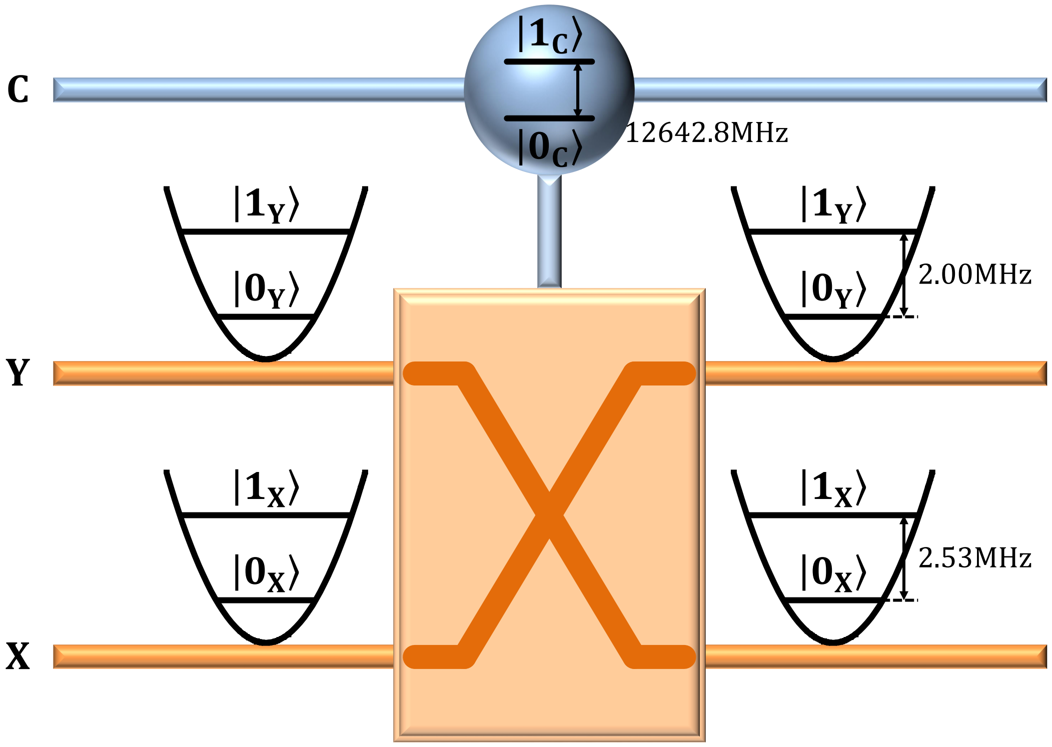
C
Y
X
$|1_C\rangle$
$|0_C\rangle$
12642.8MHz
$|1_Y\rangle$
$|0_Y\rangle$
$|1_Y\rangle$
$|0_Y\rangle$
2.00MHz
$|1_X\rangle$
$|0_X\rangle$
$|1_X\rangle$
$|0_X\rangle$
2.53MHz

图 5.2　**Encoding methods.** The control qubit C is encoded within two hyperfine levels of the $S_{1/2}$ manifold in the $^{171}\mathrm{Yb}^+$ ion. Denote these by $|0_\mathrm{C}\rangle = |F = 0, m_\mathrm{F} = 0\rangle$ and $|1_\mathrm{C}\rangle = |F = 1, m_\mathrm{F} = 0\rangle$, where F is the quantum number of total internal angular momentum and m_F is the magnetic quantum number. The transition frequency between $|0_\mathrm{C}\rangle$ and $|1_\mathrm{C}\rangle$ is 12642.826 MHz. Qubits X and Y are encoded within the ground and first excited states of two radial motional modes in $^{171}\mathrm{Yb}^+$, denoted as $|0_\mathrm{X}\rangle$, $|1_\mathrm{X}\rangle$ and $|0_\mathrm{Y}\rangle$, $|1_\mathrm{Y}\rangle$. The trap frequencies of modes X and Y are given by 2.53 MHz and 2.00 MHz.

a system of three qubits. Qubit C represents the control, which is encoded into the internal states of ${}^{171}\mathrm{Yb}^{+}$. Two registers, denoted as qubits X and Y, are encoded into the external motional levels of ${}^{171}\mathrm{Yb}^{+}$ (See Fig. 5.2 for details).

5.2.2.1 Basic operations

We use microwaves to perform the operations on hyperfine levels of ${}^{171}\mathrm{Yb}^{+}$

$$R_0(\chi,\phi) = \exp\left[-\frac{i\chi}{2}\left(e^{-i\phi}\left|1_{\mathrm{C}}\right\rangle\left\langle 0_{\mathrm{C}}\right| + \mathrm{H.c.}\right)\right], \tag{5-1}$$

$$R_{\pm\mathrm{Z}}(\chi,\phi) = \exp\left[-\frac{i\chi}{2}\left(e^{-i\phi}\left|\pm \mathrm{Z}_{\mathrm{C}}\right\rangle\left\langle 0_{\mathrm{C}}\right| + \mathrm{H.c.}\right)\right], \tag{5-2}$$

where the carrier operation (see Eq. (5-1)) drives transition $|0_{\mathrm{C}}\rangle \leftrightarrow |1_{\mathrm{C}}\rangle$ resonantly, and the Zeeman operations (see Eq. (5-2)) drive transitions $|0_{\mathrm{C}}\rangle \leftrightarrow |\pm \mathrm{Z}_{\mathrm{C}}\rangle$ resonantly[32,37].

We use counter-propagating Raman laser beams to execute the blue sideband operations, which are the operations between hyperfine and motional levels

$$R_{\mathrm{X}}(\chi,\phi) = \exp\left[\frac{\chi}{2}\left(e^{-i\phi}\sigma_{+}a_{\mathrm{X}}^{\dagger} - e^{i\phi}\sigma_{-}a_{\mathrm{X}}\right)\right], \tag{5-3}$$

$$R_{\mathrm{Y}}(\chi,\phi) = \exp\left[\frac{\chi}{2}\left(e^{-i\phi}\sigma_{+}a_{\mathrm{Y}}^{\dagger} - e^{i\phi}\sigma_{-}a_{\mathrm{Y}}\right)\right], \tag{5-4}$$

where $\sigma_{+} = |1_{\mathrm{C}}\rangle\langle 0_{\mathrm{C}}|$, $\sigma_{-} = |0_{\mathrm{C}}\rangle\langle 1_{\mathrm{C}}|$, a_{X} ($a_{\mathrm{X}}^{\dagger}$) and a_{Y} ($a_{\mathrm{Y}}^{\dagger}$) are the annihilation (creation) operators of motional modes X and Y[9,17,39].

5.2.2.2 Preprocessing

During *preprocessing*, the standard circuit design for synthesizing ρ_1 involves application of a controlled swap (CSWAP) gate on registers X and Y with qubit C as the control. Since ρ_1 is input-independent, for the purposes of modular DQC1, any means of preparing this state is equally valid. Here, we perform *preprocessing* without explicitly using the CSWAP gate, with no impact on practical usages and scalability.

For the case of n-qubit registers, prepocessing creates a mixed state

$$\rho_1 = \frac{1}{N^2}\sum_{l,m=0}^{N-1}\left|\psi_{l,m}\right\rangle\left\langle\psi_{l,m}\right|, \tag{5-5}$$

where $N = 2^n$, and each pure state $|\psi_{l,m}\rangle = (|0_{\mathrm{C}} l_{\mathrm{X}} m_{\mathrm{Y}}\rangle + |1_{\mathrm{C}} m_{\mathrm{X}} l_{\mathrm{Y}}\rangle)/\sqrt{2}$ is created by

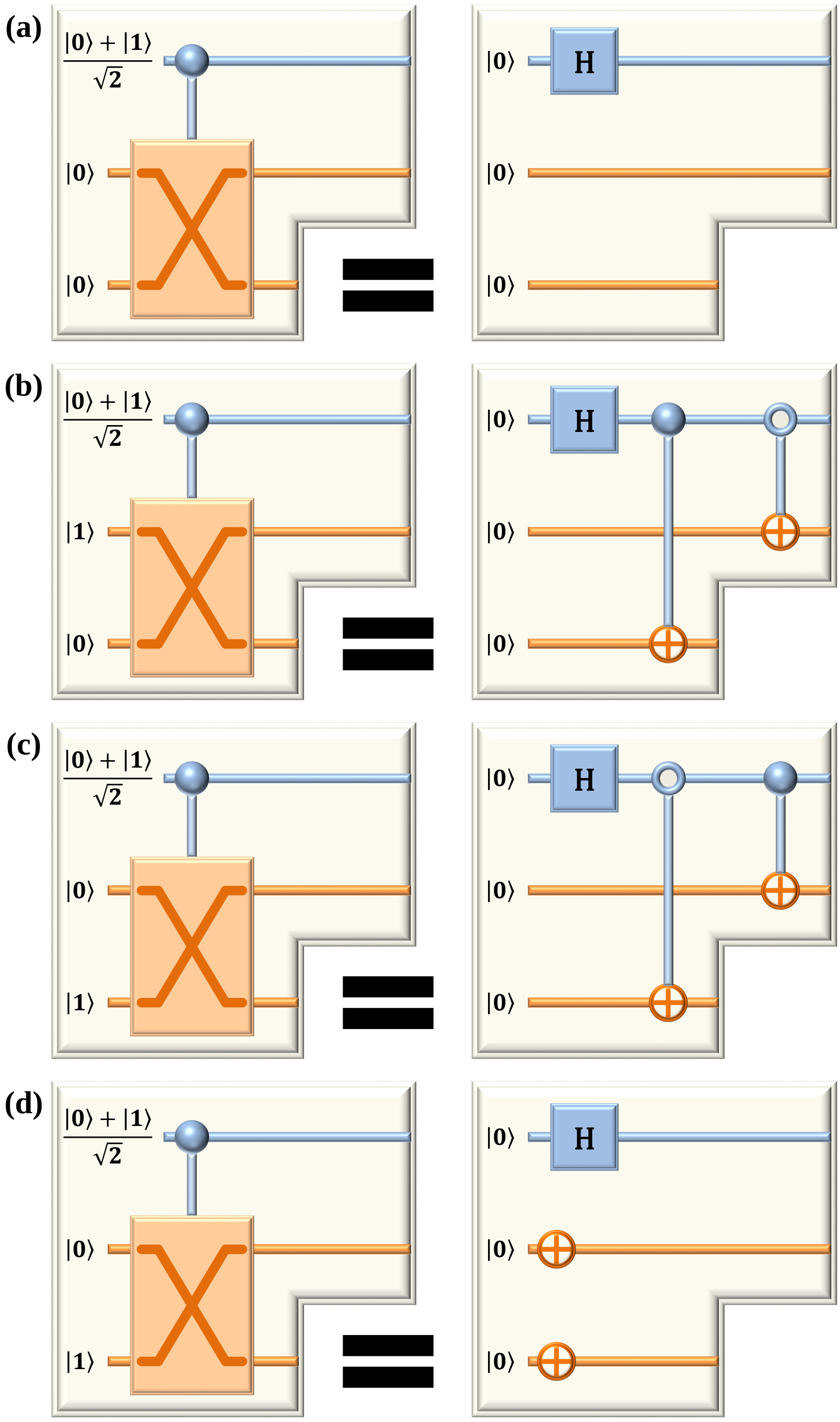
(a)
$\frac{|0\rangle+|1\rangle}{\sqrt{2}}$
$|0\rangle$
$|0\rangle$
H
(b)
$|1\rangle$
(c)
(d)

图 5.3　**Conceptual circuits of implementating preprocessing.** In $n = 1$ modular DQC1, each pure state component of ρ_1 (see Eq. (5-5)) is created by each circuit shown in left column. Our implementation processes are conceptually represented by the circuits in right column, where the output of each circuit is the same as the corresponding circuit in left column.

表 5.1 **Implementation of preprocessing.** Each sequence shown in the right column implements the corresponding operation shown in the left column.

Operation	Sequence
$\lvert 0_C0_X0_Y\rangle \to (\lvert 0_C0_X0_Y\rangle + \lvert 1_C0_X0_Y\rangle)/\sqrt{2}$	$R_0(\pi/2, -\pi/2)$
$\lvert 0_C0_X0_Y\rangle \to (\lvert 0_C0_X1_Y\rangle - \lvert 1_C1_X0_Y\rangle)/\sqrt{2}$	$R_0(\pi/2, -\pi/2)$, $R_0(\pi, \pi/2)$, $R_{-Z}(\pi, 0)$, $R_0(\pi, -\pi/2)$, $R_Y(\pi, 0)$, $R_0(\pi, \pi/2)$, $R_{-Z}(\pi, 0)$, $R_X(\pi, 0)$, $R_{-Z}(\pi, \pi)$
$\lvert 0_C0_X0_Y\rangle \to (\lvert 0_C1_X0_Y\rangle + \lvert 1_C0_X1_Y\rangle)/\sqrt{2}$	$R_0(\pi/2, -\pi/2)$, $R_0(\pi, \pi/2)$, $R_{-Z}(\pi, 0)$, $R_0(\pi, -\pi/2)$, $R_X(\pi, 0)$, $R_0(\pi, \pi/2)$, $R_{-Z}(\pi, 0)$, $R_Y(\pi, \pi)$, $R_{-Z}(\pi, \pi)$
$\lvert 0_C0_X0_Y\rangle \to (\lvert 0_C1_X1_Y\rangle + \lvert 1_C1_X1_Y\rangle)/\sqrt{2}$	$R_X(\pi, 0)$, $R_0(\pi, \pi/2)$, $R_Y(\pi, \pi)$, $R_0(\pi, \pi/2)$, $R_0(\pi/2, -\pi/2)$

applying a CSWAP gate on state $(\lvert 0_C\rangle + \lvert 1_C\rangle)/\sqrt{2} \otimes \lvert l_X\rangle \otimes \lvert m_Y\rangle$. The mixed state ρ_1 (see Eq. (5-5)) can be created by generating each $\lvert \psi_{l,m}\rangle$ with equal weight.

For our implementation at $n = 1$ case, we simplify *preprocessing* by inputting the same state $\lvert 0_C0_X0_Y\rangle$ into different circuits, instead of inputting different states $\lvert 0_C l_X m_Y\rangle$ into the same circuit (see Fig. 5.3). Our implementation processes are as follows

$$\begin{aligned}
\lvert 0_C0_X0_Y\rangle &\to \frac{\lvert 0_C\rangle + \lvert 1_C\rangle}{\sqrt{2}} \lvert 0_X\rangle \lvert 0_Y\rangle = \lvert \psi'_{0,0}\rangle, && \text{(5-6)}\\
\lvert 0_C0_X0_Y\rangle &\to \frac{\lvert 0_C\rangle + \lvert 1_C\rangle}{\sqrt{2}} \lvert 0_X\rangle \lvert 0_Y\rangle && \text{(5-7)}\\
&\to \lvert \psi'_{0,1}\rangle = \frac{\lvert 0_C0_X1_Y\rangle - \lvert 1_C1_X0_Y\rangle}{\sqrt{2}}, && \text{(5-8)}\\
\lvert 0_C0_X0_Y\rangle &\to \frac{\lvert 0_C\rangle + \lvert 1_C\rangle}{\sqrt{2}} \lvert 0_X\rangle \lvert 0_Y\rangle && \text{(5-9)}\\
&\to \lvert \psi'_{1,0}\rangle = \frac{\lvert 0_C1_X0_Y\rangle + \lvert 1_C0_X1_Y\rangle}{\sqrt{2}}, && \text{(5-10)}\\
\lvert 0_C0_X0_Y\rangle &\to \lvert 0_C1_X1_Y\rangle && \text{(5-11)}\\
&\to \lvert \psi'_{1,1}\rangle = \frac{\lvert 0_C\rangle + \lvert 1_C\rangle}{\sqrt{2}} \lvert 1_X\rangle \lvert 1_Y\rangle, && \text{(5-12)}
\end{aligned}$$

which are conceptually represented by the circuits in the right column of Fig. 5.3. We repeat each process 1000 times to create the ensemble of mixed state

$$\rho'_1 = \frac{1}{4} \sum_{l,m=0}^{1} \lvert \psi'_{l,m}\rangle \langle \psi'_{l,m}\rvert = Z_1^\dagger \rho_1 Z_1, \tag{5-13}$$

where the phase shift

$$Z_1 = \mathrm{Diag}\,(1, 1, 1, 1, 1, -1, 1, 1), \tag{5-14}$$

caused by the minus sign of $|\psi'_{0,1}\rangle$ in Eq. (5-8), has no effect on the results, which is proved in 5.2.2.5. The detail of implementation of each process is shown in Tab. 5.1.

Our approach of implementing *preprocessing* can be scaled up to general n case, where each register is encoded to the ground and first excited states of n motional modes. For any $l, m = 0, 1, \cdots, N-1$, pure state $|\psi'_{l,m}\rangle$ is created by invoking the processes of $n = 1$ case as follows

$$
\begin{aligned}
|0_\mathrm{C}0_\mathrm{X}0_\mathrm{Y}\rangle &\to |0_\mathrm{C}(l\,\&\,m)_\mathrm{X}(l\,\&\,m)_\mathrm{Y}\rangle && \text{(5-15)}\\
&\to \frac{|0_\mathrm{C}\rangle + |1_\mathrm{C}\rangle}{\sqrt{2}}\,|(l\,\&\,m)_\mathrm{X}\rangle\,|(l\,\&\,m)_\mathrm{Y}\rangle && \text{(5-16)}\\
&\to \frac{|0_\mathrm{C}l_\mathrm{X}(l\,\&\,m)_\mathrm{Y}\rangle + |1_\mathrm{C}(l\,\&\,m)_\mathrm{X}l_\mathrm{Y}\rangle}{\sqrt{2}} && \text{(5-17)}\\
&\to \frac{|0_\mathrm{C}l_\mathrm{X}m_\mathrm{Y}\rangle + (-1)^p\,|1_\mathrm{C}m_\mathrm{X}l_\mathrm{Y}\rangle}{\sqrt{2}} = |\psi'_{l,m}\rangle, && \text{(5-18)}
\end{aligned}
$$

where the operator ‘&’ is bitwise-AND, and p is the number of 1 in binary representation of $\bar{l}\,\&\,m$, where the bar operator is bitwise-NOT. Process of Eq. (5-15) is realized by repeatedly conducting process of Eq. (5-11) on the corresponding qubits of registers X and Y. Process of Eq. (5-16) is realized by a Hadamard gate on qubit C. Processes of Eq. (5-17) is realized by repeatedly conducting process of Eq. (5-10). And Eq. (5-18) is by Eq. (5-8).

5.2.2.3 Postprocessing

During *postprocessing*, a second CSWAP gate is necessary for extracting information about $|T(U)|$ from ρ_2. This ρ_2 is input-dependent, thus the CSWAP gate needs to be realized explicitly. In our experiment, we pioneer a way to realize the CSWAP gate involving motional qubits by using a sequence of Raman laser beams together with microwaves, as shown in Fig. 5.4.

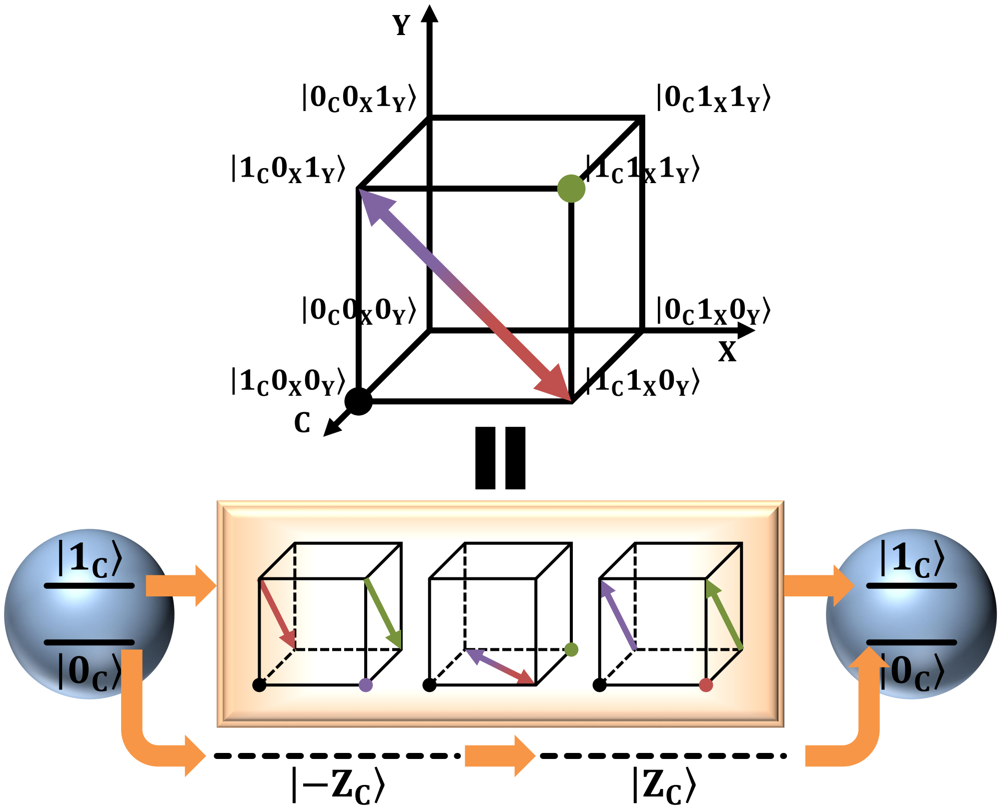
Y
$|0_C0_X1_Y\rangle$
$|0_C1_X1_Y\rangle$
$|1_C0_X1_Y\rangle$
$|1_C1_X1_Y\rangle$
$|0_C0_X0_Y\rangle$
$|0_C1_X0_Y\rangle$
X
$|1_C0_X0_Y\rangle$
$|1_C1_X0_Y\rangle$
C
$|1_C\rangle$
$|0_C\rangle$
$|1_C\rangle$
$|0_C\rangle$
$|-Z_C\rangle$
$|Z_C\rangle$

图 5.4　**The implementation of control SWAP gate.** A CSWAP operation on X and Y represents coherently interchanging the populations of $|1_C0_X1_Y\rangle$ and $|1_C1_X0_Y\rangle$. In experiment this is achieved as follows: first, we temporarily shelve $|0_C\rangle$ into an ancillary Zeeman level $|\pm Z_C\rangle = |F = 1, m_F = \pm 1\rangle$ by microwave pulses. The Two Zeeman levels $|Z_C\rangle$ and $|-Z_C\rangle$ are employed sequentially with equal duration, so that the AC stark shift and energy level jittering of both Zeeman levels cancel. The transition between $|0_C\rangle$ and $|\pm Z_C\rangle = |F = 1, m_F = \pm 1\rangle$ is realized by a microwave pulse with frequency $12642.819 \pm 9.507 m_F$ MHz. Meanwhile the SWAP operation that interchanges $|1_C0_X1_Y\rangle$ and $|1_C1_X0_Y\rangle$ is realized by 3 sequential Raman pulses. Subsequently, the shelved $|0_C\rangle$ is restored by a second microwave pulse.

表 5.2　**Implementation of postprocessing.** Here $\alpha = \arccos\left[\csc(\pi/\sqrt{2})/\sqrt{2}\right]$ and $\gamma = \phi - \arccos\left[\cot(\pi/\sqrt{2})\right]$.

Operation	Sequence
$F(\phi)$	$R_{-Z}(\pi, 0)$, $R_Y(\pi, \pi)$, $R_X(\pi/\sqrt{2}, \gamma)$, $R_X(\pi/\sqrt{2}, 2\alpha + \gamma)$, $R_Z(\pi, \pi)$, $R_{-Z}(\pi, \pi)$, $R_Z(\pi, 0)$, $R_X(\pi/\sqrt{2}, 2\alpha + \gamma)$, $R_X(\pi/\sqrt{2}, \gamma)$, $R_Y(\pi, 0)$, $R_Z(\pi, \pi)$

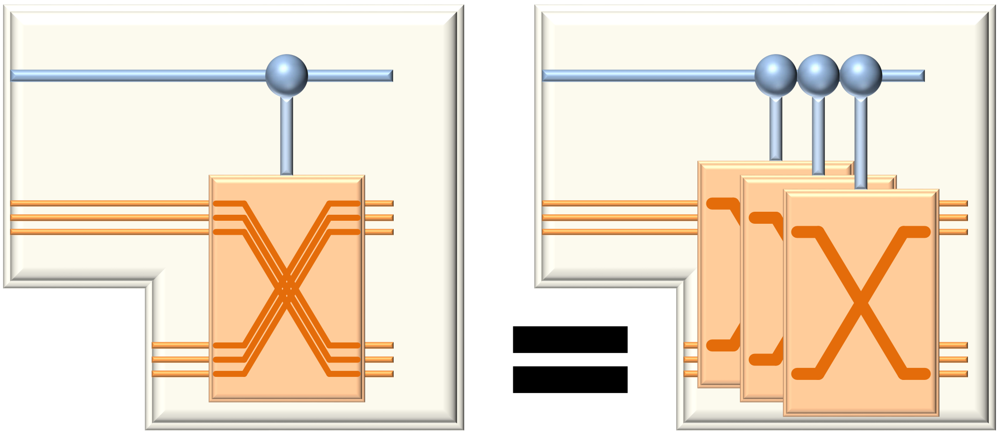

图 5.5　**Scalability of the CSWAP gate.** A CSWAP gate with n-qubit registers, as shown in left circuit, is equivalent to a combination of n CSWAP gates with 1-qubit registers, as shown in right circuit.

Instead of implementing a standard CSWAP gate, we develop the following operation

$$F(\phi) = \begin{pmatrix} 1 &&&&&&& \\ & 1 &&&&&& \\ && 1 &&&&& \\ &&& 1 &&&& \\ &&&& 1 &&& \\ &&&&&& -e^{i\phi} & \\ &&&&& e^{-i\phi} && \\ &&&&&&& 1 \end{pmatrix} \tag{5-19}$$

with basis $|0_\mathrm{C}0_\mathrm{X}0_\mathrm{Y}\rangle, |0_\mathrm{C}0_\mathrm{X}1_\mathrm{Y}\rangle, \cdots, |1_\mathrm{C}1_\mathrm{X}1_\mathrm{Y}\rangle$. When qubit C is in state $|0_\mathrm{C}\rangle$, it is temporarily shelved into Zeeman levels $|\pm\mathrm{Z_C}\rangle$. We first transfer $|0_\mathrm{C}\rangle$ to $|-\mathrm{Z_C}\rangle$ by $R_{\text{-Z}}(\pi, 0)$ in the beginning. At halfway, $|-\mathrm{Z_C}\rangle$ is transferred to $|\mathrm{Z_C}\rangle$ by sequence $R_\mathrm{Z}(\pi,\pi)$, $R_{\text{-Z}}(\pi,\pi)$, $R_\mathrm{Z}(\pi, 0)$. Finally, we transfer $|\mathrm{Z_C}\rangle$ back to $|0_\mathrm{C}\rangle$ by $R_\mathrm{Z}(\pi,\pi)$ in the end. When qubit C is in state $|1_\mathrm{C}\rangle$, a swap of populations between $|1_\mathrm{C}0_\mathrm{X}1_\mathrm{Y}\rangle$ and $|1_\mathrm{C}1_\mathrm{X}0_\mathrm{Y}\rangle$ is executed by sequence $R_\mathrm{Y}(\pi,\pi)$, $S_\mathrm{X}(\pi,\phi)$, $R_\mathrm{Y}(\pi, 0)$. The full implementation of $F(\phi)$ is shown in Tab. 5.2. In *postprocessing*, we perform operation $F(0) = F_0 Z_3$, where F_0 is a standard CSWAP gate, and the phase shift

$$Z_3 = \mathrm{Diag}(1, 1, 1, 1, 1, -1, 1, 1) \tag{5-20}$$

has no effect on the results, which is proved in 5.2.2.5.

表 5.3 **Implementation of outsourcing.** Here $\alpha = \arccos\left[\csc(\pi/\sqrt{2})\sin(\chi/4)\right]$ and $\gamma = \phi - \arccos\left[\cot(\pi/\sqrt{2})\tan(\chi/4)\right]$.

Operation	Sequence
$U(\chi,\theta,\phi)$	$R_0(\pi/2-\theta,\phi+\pi/2)$, $R_0(\chi,\phi)$, $R_0(\pi/2-\theta,\phi-\pi/2)$
$S_X(\chi,\phi)$	$R_X(\pi/\sqrt{2},\gamma)$, $R_X(\sqrt{2}\pi,2\alpha+\gamma)$, $R_X(\pi/\sqrt{2},\gamma)$

We also demonstrate the scalability of our approach of implementing CSWAP gate. For general n case, the implementation can be done by repeatedly conducting $F(0)$ (see Fig. 5.5).

The final measurement is a $\langle\sigma_1\rangle$ measurement on qubit C. A single $\langle\sigma_1\rangle$ measurement is realized by sequentially applying Hadamard gate and standard fluorescence detection. A complete run of modular DQC1 requires single $\langle\sigma_1\rangle$ measurement for each of 4 *preprocessing* modules. For each of 19 different U processes, we evaluate $\langle\sigma_1\rangle$ by averaging the results of 1000 runs and correcting detection error. In total, we conduct $4 \times 19 \times 1000 = 76000$ measurements.

5.2.2.4 The outsoucing of U

To benchmark Alice's protocol, our experiment also needs to simulate the actions of the server Bob. In practical situations, the server would likely be spatially separated from Alice, and the quantum interface between Alice and Bob would involve a physical medium that is relatively amenable to long range quantum communication (e.g. optical modes). Bob would then map this information onto a more suitable medium for direct computation.

As a proof of principle demonstration, We simulate the actions of the server by acting unitaries on the trapped ion system, transforming ρ_1 to $\rho_2 = U\rho_1 U^\dagger$ for various choices of U. This is achieved by using coherent quantum SWAP gates to temporarily map information from the motional degree of freedom into the internal state of the trapped ion. The state can then be directly addressed to implement U, after which a second quantum SWAP maps it back into the motional degree to obtain ρ_2.

A general U is represented by matrix

$$
\begin{aligned}
U &= \begin{pmatrix} a & b \\ -b^* & a^* \end{pmatrix} = \exp\left(-\tfrac{i\chi}{2}\sigma_{\theta,\phi}\right) \\
&= \begin{pmatrix} \cos\frac{\chi}{2} + i\sin\frac{\chi}{2}\cos\theta & -i\sin\frac{\chi}{2}\sin\theta e^{i\phi} \\ -i\sin\frac{\chi}{2}\sin\theta e^{-i\phi} & \cos\frac{\chi}{2} - i\sin\frac{\chi}{2}\cos\theta \end{pmatrix}
\end{aligned}
\tag{5-21}
$$

with basis $|0\rangle$ and $|1\rangle$, where

$$
\sigma_{\theta,\phi} = \begin{pmatrix} -\cos\theta & \sin\theta e^{i\phi} \\ \sin\theta e^{-i\phi} & \cos\theta \end{pmatrix}
\tag{5-22}
$$

is a Pauli operator in any direction. For the demonstration of $n = 1$ case, qubit C is employed as the register qubit of server, on which U is performed by microwave operations (see Tab. 5.3).

The quantum application programming interface (API), through which client and server communicate, is implemented by 2 SWAP gates (see Fig. 5.1(b)). In experiment, instead of using standard SWAP gates, we develop the following operation

$$
S_{\mathrm{X}}(\chi,\phi) = \begin{pmatrix} \cos\frac{\chi}{2} & & & -\sin\frac{\chi}{2}e^{i\phi} \\ & 1 & & \\ & & 1 & \\ \sin\frac{\chi}{2}e^{-i\phi} & & & \cos\frac{\chi}{2} \end{pmatrix}
\tag{5-23}
$$

with basis $|0_{\mathrm{C}}0_{\mathrm{X}}\rangle$, $|1_{\mathrm{C}}0_{\mathrm{X}}\rangle$, $|0_{\mathrm{C}}1_{\mathrm{X}}\rangle$ and $|1_{\mathrm{C}}1_{\mathrm{X}}\rangle$, by Raman operations (see Tab. 5.3). It can still function as quantum API. The experimental effect of outsourcing module is

$$
S_{\mathrm{X}}(\pi,\pi)U_{\mathrm{C}}S_{\mathrm{X}}(\pi,0) = \begin{pmatrix} a^* & -b^* & & \\ b & a & & \\ & & a^* & b^* \\ & & -b & a \end{pmatrix} = Z_2U_{\mathrm{X}}^*Z_2^\dagger,
\tag{5-24}
$$

where operation U_{C} (U_{X}) is U on qubit C (X), and the phase shift

$$
Z_2 = \mathrm{Diag}\,(1,-1,1,1)
\tag{5-25}
$$

has no effect on the results, which is proved in 5.2.2.5, and U^* has the same effect on the results as U, since $|\mathrm{tr}(U^*)| = |\mathrm{tr}(U)|$.

5.2.2.5 Phase issues

Here we prove that phase shifts Z_1, Z_2 and Z_3 (see Eq. (5-14)(5-25)(5-20)), has no effect on theoretical expectation value $\langle\sigma_1\rangle$. In fact, the above conclusion is true for general n case, as long as $Z_1 = Z_3$. In this case, the state before measurement is

$$\begin{aligned}
\rho_3' &= \tfrac{1}{N'} F_0 Z_1 Z_2 U_\mathrm{X} Z_2^\dagger Z_1^\dagger F_0 \begin{pmatrix} I & I \\ I & I \end{pmatrix} F_0 Z_1 Z_2 U_\mathrm{X}^\dagger Z_2^\dagger Z_1^\dagger F_0 \\
&= \tfrac{1}{N'} \Lambda F_0 U_\mathrm{X} F_0 \Lambda^\dagger \begin{pmatrix} I & I \\ I & I \end{pmatrix} \Lambda F_0 U_\mathrm{X}^\dagger F_0 \Lambda^\dagger \\
&= \tfrac{1}{N'} \begin{pmatrix} \Lambda_0 U_\mathrm{X} \Lambda_0^\dagger & \\ & \Lambda_1 U_\mathrm{Y} \Lambda_1^\dagger \end{pmatrix} \begin{pmatrix} I & I \\ I & I \end{pmatrix} \begin{pmatrix} \Lambda_0 U_\mathrm{X}^\dagger \Lambda_0^\dagger & \\ & \Lambda_1 U_\mathrm{Y}^\dagger \Lambda_1^\dagger \end{pmatrix} \\
&= \tfrac{1}{N'} \begin{pmatrix} I & \Lambda_0 U_\mathrm{X} \Lambda_0^\dagger \Lambda_1 U_\mathrm{Y}^\dagger \Lambda_1^\dagger \\ \Lambda_1 U_\mathrm{Y} \Lambda_1^\dagger \Lambda_0 U_\mathrm{X}^\dagger \Lambda_0^\dagger & I \end{pmatrix}
\end{aligned} \tag{5-26}$$

with basis $|0_\mathrm{C}\rangle$ and $|1_\mathrm{C}\rangle$, where I is the identity matrix,

$$\Lambda = F_0 Z_1 Z_2 F_0 = \begin{pmatrix} \Lambda_0 & \\ & \Lambda_1 \end{pmatrix} \tag{5-27}$$

has only eigenvalues of ±1, and N' is the dimension of system. For general n case, the client possesses 1 control qubit and 2 registers, and the server possesses 1 register. Thus $N' = 2N^3$. In our special case, the control qubit serves as server register. Thus $N' = 8$.

We derive the expectation value $\langle\sigma_1\rangle$ of ρ_3'

$$\begin{aligned}
\langle\sigma_1\rangle &= \mathrm{tr}\left(\Lambda_0 U_\mathrm{X} \Lambda_0^\dagger \Lambda_1 U_\mathrm{Y}^\dagger \Lambda_1^\dagger + \mathrm{h.c.}\right)/N' \\
&= \textstyle\sum_{l,m} \langle l|\, \Lambda_0 U_\mathrm{X} \Lambda_0^\dagger \,|m\rangle \langle m|\, \Lambda_1 U_\mathrm{Y}^\dagger \Lambda_1^\dagger \,|l\rangle /N' + \mathrm{h.c.} \\
&= \textstyle\sum_m \langle m|\, U_\mathrm{X} \,|m\rangle \langle m|\, U_\mathrm{Y}^\dagger \,|m\rangle /N' + \mathrm{h.c.} \\
&= \mathrm{tr}(U \otimes U^\dagger + U^\dagger \otimes U)/(2N) \\
&= |\mathrm{tr}(U)/N|^2,
\end{aligned} \tag{5-28}$$

where $|l\rangle = |m\rangle$ (if $|l\rangle \neq |m\rangle$, then $\langle l|\, U_\mathrm{X} \,|m\rangle = 0$ or $\langle l|\, U_\mathrm{Y} \,|m\rangle = 0$) traverses the N' eigenstates of Λ, and U is an $N \times N$ matrix. Thus we prove our conclusion.

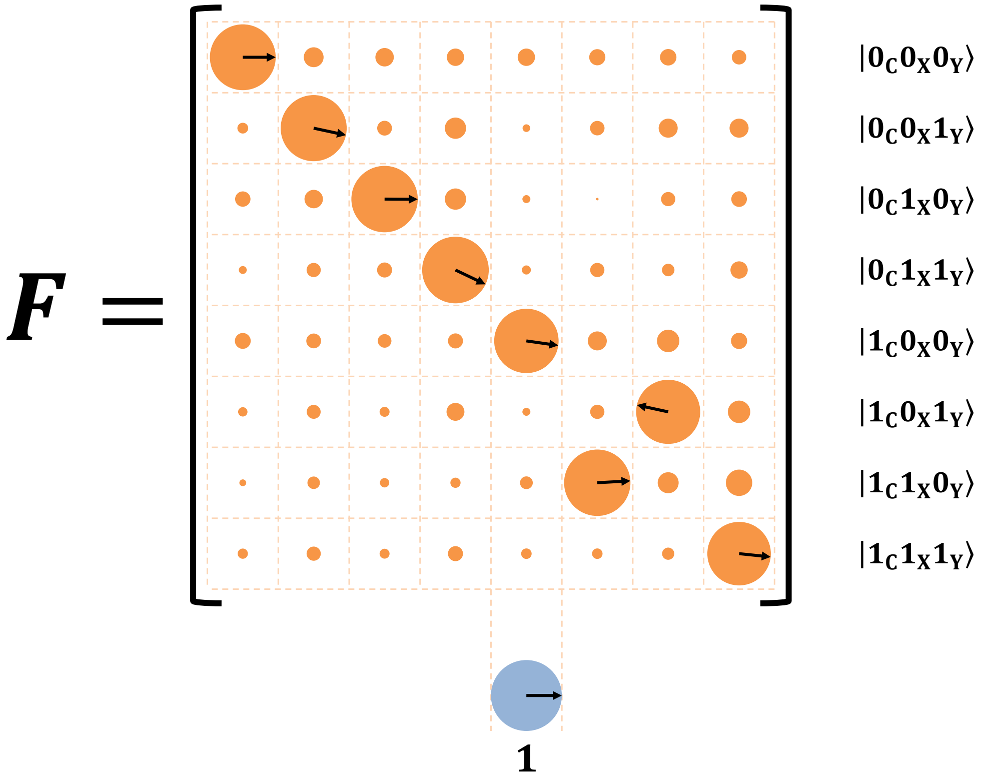

图 5.6 **The truth table of control SWAP gate.** Visual representation of relevant probabilities and the phases of the CSWAP gate in the computational basis. The area of orange disk on the l^{th} column and m^{th} row reflects the probability of obtaining corresponding output $|l\rangle$ given corresponding input $|m\rangle$, where l, m range over all binary representations of the 3 encoded qubits. So the radius of the disk is proportional to $|\langle l| F |m\rangle|$. Meanwhile, the orientation of each black arrow on the disk gives the phase information of corresponding element $\langle l| F |m\rangle$. The radius and orientation of the blue disk represents an amplitude of 1 and a phase of 0. Note that the negative phase $\langle 1_C 0_X 1_Y| F |1_C 1_X 0_Y\rangle = -1$ is consequence of the choice of physical realization, and does not affect computational output (see 5.2.2.5).

5.2.3 Performance of CSWAP gate

To demonstrate the validity of our CSWAP operation, we find its 8×8 truth table (see Fig. 5.6) achieves a fidelity (classical gate fidelity[51]) of 0.85 ± 0.02.

The theoretical result of $F(0)$ is defined in Eq. (5-19). In experiment, we obtain the absolute value of each matrix element of $F(0)$. We also obtain the phase of any element that has a absolute value of 1 in theory. These are all done by measuring population $|\langle\varphi| F(0) |\psi\rangle|^2$ for necessary inputs $|\psi\rangle$ and outputs $|\varphi\rangle$. Each measurement

$$|\langle\varphi| F(0) |\psi\rangle|^2 = |\langle 1_C 1_X 1_Y| R_o F(0) R_i |0_C 0_X 0_Y\rangle|^2 \tag{5-29}$$

表 5.4　**Implementation of R_{i}.**

Operation	Sequence
$\lvert 0_{\mathrm{C}}0_{\mathrm{X}}0_{\mathrm{Y}}\rangle \rightarrow \lvert 0_{\mathrm{C}}0_{\mathrm{X}}1_{\mathrm{Y}}\rangle$	$R_{\mathrm{Y}}(\pi, 0)$, $R_0(\pi, \pi/2)$
$\lvert 0_{\mathrm{C}}0_{\mathrm{X}}0_{\mathrm{Y}}\rangle \rightarrow \lvert 0_{\mathrm{C}}1_{\mathrm{X}}0_{\mathrm{Y}}\rangle$	$R_{\mathrm{X}}(\pi, 0)$, $R_0(\pi, \pi/2)$
$\lvert 0_{\mathrm{C}}0_{\mathrm{X}}0_{\mathrm{Y}}\rangle \rightarrow \lvert 0_{\mathrm{C}}1_{\mathrm{X}}1_{\mathrm{Y}}\rangle$	$R_{\mathrm{X}}(\pi, 0)$, $R_0(\pi, \pi/2)$, $R_{\mathrm{Y}}(\pi, 0)$, $R_0(\pi, \pi/2)$
$\lvert 0_{\mathrm{C}}0_{\mathrm{X}}0_{\mathrm{Y}}\rangle \rightarrow \lvert 1_{\mathrm{C}}0_{\mathrm{X}}0_{\mathrm{Y}}\rangle$	$R_0(\pi, -\pi/2)$
$\lvert 0_{\mathrm{C}}0_{\mathrm{X}}0_{\mathrm{Y}}\rangle \rightarrow \lvert 1_{\mathrm{C}}0_{\mathrm{X}}1_{\mathrm{Y}}\rangle$	$R_{\mathrm{Y}}(\pi, 0)$
$\lvert 0_{\mathrm{C}}0_{\mathrm{X}}0_{\mathrm{Y}}\rangle \rightarrow \lvert 1_{\mathrm{C}}1_{\mathrm{X}}0_{\mathrm{Y}}\rangle$	$R_{\mathrm{X}}(\pi, 0)$
$\lvert 0_{\mathrm{C}}0_{\mathrm{X}}0_{\mathrm{Y}}\rangle \rightarrow \lvert 1_{\mathrm{C}}1_{\mathrm{X}}1_{\mathrm{Y}}\rangle$	$R_{\mathrm{X}}(\pi, 0)$, $R_0(\pi, \pi/2)$, $R_{\mathrm{Y}}(\pi, 0)$
$\lvert 0_{\mathrm{C}}0_{\mathrm{X}}0_{\mathrm{Y}}\rangle \rightarrow (\lvert 0_{\mathrm{C}}0_{\mathrm{X}}0_{\mathrm{Y}}\rangle + \lvert 1_{\mathrm{C}}0_{\mathrm{X}}0_{\mathrm{Y}}\rangle)/\sqrt{2}$	$R_0(\pi/2, -\pi/2)$
$\lvert 0_{\mathrm{C}}0_{\mathrm{X}}0_{\mathrm{Y}}\rangle \rightarrow (\lvert 0_{\mathrm{C}}0_{\mathrm{X}}0_{\mathrm{Y}}\rangle + \lvert 1_{\mathrm{C}}0_{\mathrm{X}}1_{\mathrm{Y}}\rangle)/\sqrt{2}$	$R_{\mathrm{Y}}(\pi/2, 0)$
$\lvert 0_{\mathrm{C}}0_{\mathrm{X}}0_{\mathrm{Y}}\rangle \rightarrow (\lvert 0_{\mathrm{C}}0_{\mathrm{X}}0_{\mathrm{Y}}\rangle + \lvert 1_{\mathrm{C}}1_{\mathrm{X}}0_{\mathrm{Y}}\rangle)/\sqrt{2}$	$R_{\mathrm{X}}(\pi/2, 0)$
$\lvert 0_{\mathrm{C}}0_{\mathrm{X}}0_{\mathrm{Y}}\rangle \rightarrow (\lvert 0_{\mathrm{C}}0_{\mathrm{X}}1_{\mathrm{Y}}\rangle + \lvert 1_{\mathrm{C}}1_{\mathrm{X}}0_{\mathrm{Y}}\rangle)/\sqrt{2}$	$R_{-\mathrm{Z}}(\pi/2, -\pi/2)$, $R_{\mathrm{Y}}(\pi, 0)$, $R_0(\pi, \pi/2)$, $R_{-\mathrm{Z}}(\pi, \pi/2)$, $R_{\mathrm{X}}(\pi, 0)$, $R_{-\mathrm{Z}}(\pi, -\pi/2)$
$\lvert 0_{\mathrm{C}}0_{\mathrm{X}}0_{\mathrm{Y}}\rangle \rightarrow (\lvert 0_{\mathrm{C}}0_{\mathrm{X}}1_{\mathrm{Y}}\rangle + \lvert 1_{\mathrm{C}}1_{\mathrm{X}}1_{\mathrm{Y}}\rangle)/\sqrt{2}$	$R_{\mathrm{Y}}(\pi, 0)$, $R_0(\pi, \pi/2)$, $R_{\mathrm{X}}(\pi/2, 0)$
$\lvert 0_{\mathrm{C}}0_{\mathrm{X}}0_{\mathrm{Y}}\rangle \rightarrow (\lvert 0_{\mathrm{C}}1_{\mathrm{X}}0_{\mathrm{Y}}\rangle + \lvert 1_{\mathrm{C}}0_{\mathrm{X}}1_{\mathrm{Y}}\rangle)/\sqrt{2}$	$R_{-\mathrm{Z}}(\pi/2, -\pi/2)$, $R_{\mathrm{X}}(\pi, 0)$, $R_0(\pi, \pi/2)$, $R_{-\mathrm{Z}}(\pi, \pi/2)$, $R_{\mathrm{Y}}(\pi, 0)$, $R_{-\mathrm{Z}}(\pi, -\pi/2)$
$\lvert 0_{\mathrm{C}}0_{\mathrm{X}}0_{\mathrm{Y}}\rangle \rightarrow (\lvert 0_{\mathrm{C}}1_{\mathrm{X}}0_{\mathrm{Y}}\rangle + \lvert 1_{\mathrm{C}}1_{\mathrm{X}}1_{\mathrm{Y}}\rangle)/\sqrt{2}$	$R_{\mathrm{X}}(\pi, 0)$, $R_0(\pi, \pi/2)$, $R_{\mathrm{Y}}(\pi/2, 0)$
$\lvert 0_{\mathrm{C}}0_{\mathrm{X}}0_{\mathrm{Y}}\rangle \rightarrow (\lvert 0_{\mathrm{C}}1_{\mathrm{X}}1_{\mathrm{Y}}\rangle + \lvert 1_{\mathrm{C}}1_{\mathrm{X}}1_{\mathrm{Y}}\rangle)/\sqrt{2}$	$R_{\mathrm{X}}(\pi, 0)$, $R_0(\pi, \pi/2)$, $R_{\mathrm{Y}}(\pi, 0)$, $R_0(\pi/2, \pi/2)$
$\lvert 0_{\mathrm{C}}0_{\mathrm{X}}0_{\mathrm{Y}}\rangle \rightarrow (\lvert 0_{\mathrm{C}}0_{\mathrm{X}}0_{\mathrm{Y}}\rangle + i\,\lvert 1_{\mathrm{C}}0_{\mathrm{X}}0_{\mathrm{Y}}\rangle)/\sqrt{2}$	$R_0(\pi/2, \pi)$
$\lvert 0_{\mathrm{C}}0_{\mathrm{X}}0_{\mathrm{Y}}\rangle \rightarrow (\lvert 0_{\mathrm{C}}0_{\mathrm{X}}0_{\mathrm{Y}}\rangle + i\,\lvert 1_{\mathrm{C}}0_{\mathrm{X}}1_{\mathrm{Y}}\rangle)/\sqrt{2}$	$R_{\mathrm{Y}}(\pi/2, -\pi/2)$
$\lvert 0_{\mathrm{C}}0_{\mathrm{X}}0_{\mathrm{Y}}\rangle \rightarrow (\lvert 0_{\mathrm{C}}0_{\mathrm{X}}0_{\mathrm{Y}}\rangle + i\,\lvert 1_{\mathrm{C}}1_{\mathrm{X}}0_{\mathrm{Y}}\rangle)/\sqrt{2}$	$R_{\mathrm{X}}(\pi/2, -\pi/2)$
$\lvert 0_{\mathrm{C}}0_{\mathrm{X}}0_{\mathrm{Y}}\rangle \rightarrow (\lvert 0_{\mathrm{C}}0_{\mathrm{X}}1_{\mathrm{Y}}\rangle + i\,\lvert 1_{\mathrm{C}}1_{\mathrm{X}}0_{\mathrm{Y}}\rangle)/\sqrt{2}$	$R_{-\mathrm{Z}}(\pi/2, -\pi/2)$, $R_{\mathrm{Y}}(\pi, 0)$, $R_0(\pi, \pi/2)$, $R_{-\mathrm{Z}}(\pi, \pi/2)$, $R_{\mathrm{X}}(\pi, -\pi/2)$, $R_{-\mathrm{Z}}(\pi, -\pi/2)$
$\lvert 0_{\mathrm{C}}0_{\mathrm{X}}0_{\mathrm{Y}}\rangle \rightarrow (\lvert 0_{\mathrm{C}}0_{\mathrm{X}}1_{\mathrm{Y}}\rangle + i\,\lvert 1_{\mathrm{C}}1_{\mathrm{X}}1_{\mathrm{Y}}\rangle)/\sqrt{2}$	$R_{\mathrm{Y}}(\pi, 0)$, $R_0(\pi, \pi/2)$, $R_{\mathrm{X}}(\pi/2, -\pi/2)$
$\lvert 0_{\mathrm{C}}0_{\mathrm{X}}0_{\mathrm{Y}}\rangle \rightarrow (\lvert 0_{\mathrm{C}}1_{\mathrm{X}}0_{\mathrm{Y}}\rangle + i\,\lvert 1_{\mathrm{C}}0_{\mathrm{X}}1_{\mathrm{Y}}\rangle)/\sqrt{2}$	$R_{-\mathrm{Z}}(\pi/2, -\pi/2)$, $R_{\mathrm{X}}(\pi, 0)$, $R_0(\pi, \pi/2)$, $R_{-\mathrm{Z}}(\pi, \pi/2)$, $R_{\mathrm{Y}}(\pi, -\pi/2)$, $R_{-\mathrm{Z}}(\pi, -\pi/2)$
$\lvert 0_{\mathrm{C}}0_{\mathrm{X}}0_{\mathrm{Y}}\rangle \rightarrow (\lvert 0_{\mathrm{C}}1_{\mathrm{X}}0_{\mathrm{Y}}\rangle + i\,\lvert 1_{\mathrm{C}}1_{\mathrm{X}}1_{\mathrm{Y}}\rangle)/\sqrt{2}$	$R_{\mathrm{X}}(\pi, 0)$, $R_0(\pi, \pi/2)$, $R_{\mathrm{Y}}(\pi/2, -\pi/2)$
$\lvert 0_{\mathrm{C}}0_{\mathrm{X}}0_{\mathrm{Y}}\rangle \rightarrow (\lvert 0_{\mathrm{C}}1_{\mathrm{X}}1_{\mathrm{Y}}\rangle + i\,\lvert 1_{\mathrm{C}}1_{\mathrm{X}}1_{\mathrm{Y}}\rangle)/\sqrt{2}$	$R_{\mathrm{X}}(\pi, 0)$, $R_0(\pi, \pi/2)$, $R_{\mathrm{Y}}(\pi, -\pi/2)$, $R_0(\pi/2, 0)$

表 5.5　**Implementation of R_o.**

Operation	Sequence
$\lvert 0_C0_X0_Y\rangle \rightarrow \lvert 1_C1_X1_Y\rangle$	$S_X(\pi,0)$, $R_0(\pi,\pi/2)$, $S_Y(\pi,0)$
$\lvert 0_C0_X1_Y\rangle \rightarrow \lvert 1_C1_X1_Y\rangle$	$S_X(\pi,0)$
$\lvert 0_C1_X0_Y\rangle \rightarrow \lvert 1_C1_X1_Y\rangle$	$S_Y(\pi,0)$
$\lvert 0_C1_X1_Y\rangle \rightarrow \lvert 1_C1_X1_Y\rangle$	$R_0(\pi,-\pi/2)$
$\lvert 1_C0_X0_Y\rangle \rightarrow \lvert 1_C1_X1_Y\rangle$	$R_0(\pi,\pi/2)$, $S_X(\pi,0)$, $R_0(\pi,\pi/2)$, $S_Y(\pi,0)$
$\lvert 1_C0_X1_Y\rangle \rightarrow \lvert 1_C1_X1_Y\rangle$	$R_0(\pi,\pi/2)$, $S_X(\pi,0)$
$\lvert 1_C1_X0_Y\rangle \rightarrow \lvert 1_C1_X1_Y\rangle$	$R_0(\pi,\pi/2)$, $S_Y(\pi,0)$
$(\lvert 0_C0_X0_Y\rangle + \lvert 1_C0_X0_Y\rangle)/\sqrt{2} \rightarrow \lvert 1_C1_X1_Y\rangle$	$R_0(\pi/2,\pi/2)$, $S_X(\pi,0)$, $R_0(\pi,\pi/2)$, $S_Y(\pi,0)$
$(\lvert 0_C0_X0_Y\rangle + \lvert 1_C0_X1_Y\rangle)/\sqrt{2} \rightarrow \lvert 1_C1_X1_Y\rangle$	$S_Y(\pi/2,0)$, $R_0(\pi,\pi/2)$, $S_X(\pi,0)$
$(\lvert 0_C0_X0_Y\rangle + \lvert 1_C1_X0_Y\rangle)/\sqrt{2} \rightarrow \lvert 1_C1_X1_Y\rangle$	$S_X(\pi/2,0)$, $R_0(\pi,\pi/2)$, $S_Y(\pi,0)$
$(\lvert 0_C0_X1_Y\rangle + \lvert 1_C0_X1_Y\rangle)/\sqrt{2} \rightarrow \lvert 1_C1_X1_Y\rangle$	$R_0(\pi/2,\pi/2)$, $S_X(\pi,0)$
$(\lvert 0_C0_X1_Y\rangle + \lvert 1_C1_X1_Y\rangle)/\sqrt{2} \rightarrow \lvert 1_C1_X1_Y\rangle$	$S_X(\pi/2,0)$
$(\lvert 0_C1_X0_Y\rangle + \lvert 1_C1_X0_Y\rangle)/\sqrt{2} \rightarrow \lvert 1_C1_X1_Y\rangle$	$R_0(\pi/2,\pi/2)$, $S_Y(\pi,0)$
$(\lvert 0_C1_X0_Y\rangle + \lvert 1_C1_X1_Y\rangle)/\sqrt{2} \rightarrow \lvert 1_C1_X1_Y\rangle$	$S_Y(\pi/2,0)$
$(\lvert 0_C1_X1_Y\rangle + \lvert 1_C1_X1_Y\rangle)/\sqrt{2} \rightarrow \lvert 1_C1_X1_Y\rangle$	$R_0(\pi/2,-\pi/2)$
$(\lvert 0_C0_X0_Y\rangle + i\,\lvert 1_C0_X0_Y\rangle)/\sqrt{2} \rightarrow \lvert 1_C1_X1_Y\rangle$	$R_0(\pi/2,0)$, $S_X(\pi,0)$, $R_0(\pi,\pi/2)$, $S_Y(\pi,0)$
$(\lvert 0_C0_X0_Y\rangle + i\,\lvert 1_C0_X1_Y\rangle)/\sqrt{2} \rightarrow \lvert 1_C1_X1_Y\rangle$	$S_Y(\pi/2,-\pi/2)$, $R_0(\pi,\pi/2)$, $S_X(\pi,0)$
$(\lvert 0_C0_X0_Y\rangle + i\,\lvert 1_C1_X0_Y\rangle)/\sqrt{2} \rightarrow \lvert 1_C1_X1_Y\rangle$	$S_X(\pi/2,-\pi/2)$, $R_0(\pi,\pi/2)$, $S_Y(\pi,0)$
$(\lvert 0_C0_X1_Y\rangle + i\,\lvert 1_C0_X1_Y\rangle)/\sqrt{2} \rightarrow \lvert 1_C1_X1_Y\rangle$	$R_0(\pi/2,0)$, $S_X(\pi,0)$
$(\lvert 0_C0_X1_Y\rangle + i\,\lvert 1_C1_X1_Y\rangle)/\sqrt{2} \rightarrow \lvert 1_C1_X1_Y\rangle$	$S_X(\pi/2,-\pi/2)$
$(\lvert 0_C1_X0_Y\rangle + i\,\lvert 1_C1_X0_Y\rangle)/\sqrt{2} \rightarrow \lvert 1_C1_X1_Y\rangle$	$R_0(\pi/2,0)$, $S_Y(\pi,0)$
$(\lvert 0_C1_X0_Y\rangle + i\,\lvert 1_C1_X1_Y\rangle)/\sqrt{2} \rightarrow \lvert 1_C1_X1_Y\rangle$	$S_Y(\pi/2,-\pi/2)$
$(\lvert 0_C1_X1_Y\rangle + i\,\lvert 1_C1_X1_Y\rangle)/\sqrt{2} \rightarrow \lvert 1_C1_X1_Y\rangle$	$R_0(\pi/2,\pi)$

表 5.6　**Implementation of $\lvert 1_C1_X1_Y\rangle$ measurement.** Here $\lvert 1_C1_X1_Y\rangle \rightarrow \lvert 0_C\rangle$ stands for a operation that transforms only $\lvert 1_C1_X1_Y\rangle$ to $\lvert 0_C\rangle$, and all other 7 base states to $\lvert 1_C\rangle$.

Operation	Sequence
$P_X(\phi)$	$R_X(\pi/2,\phi)$, $R_X(\pi/\sqrt{2},\phi+\pi/2)$, $R_X(\pi/2,\phi)$
$P_Y(\phi)$	$R_Y(\pi/2,\phi)$, $R_Y(\pi/\sqrt{2},\phi+\pi/2)$, $R_Y(\pi/2,\phi)$
$\lvert 1_C1_X1_Y\rangle \rightarrow \lvert 0_C\rangle$	$P_X(0)$, $R_0(\pi,-\pi/2)$, $P_Y(0)$

consists of the foolowing 5 steps. First, we prepare $|0_C 0_X 0_Y\rangle$ by standard sideband cooling. Second, we conduct R_i, which prepares $|\psi\rangle$ from $|0_C 0_X 0_Y\rangle$ (see Tab. 5.4). Third is $F(0)$. Fourth is R_i, which transforms output $|\varphi\rangle$ to $|1_C 1_X 1_Y\rangle$ (see Tab. 5.5). And the last is the population measurement of $|1_C 1_X 1_Y\rangle$ (see Tab. 5.6).

To measure the population of $|1_C 1_X 1_Y\rangle$, we develop $P_X(\phi)$ operation that instigates π transitions for both $|0_C 0_X\rangle \leftrightarrow |1_C 1_X\rangle$ and $|0_C 1_X\rangle \leftrightarrow |1_C 2_X\rangle$, and $P_Y(\phi)$ operation which is defined similarly (see Tab. 5.6). By a proper sequence that involves $P_X(0)$ and $P_Y(0)$, we are able to transforms $|1_C 1_X 1_Y\rangle$ to $|0_C\rangle$, and $|0_C 0_X 0_Y\rangle, |0_C 0_X 1_Y\rangle, \cdots, |1_C 1_X 0_Y\rangle$ to $|1_C\rangle$ (see Tab. 5.6). After this sequence, $|1_C 1_X 1_Y\rangle$ population measurement can then be completed by measuring the population of $|0_C\rangle$, which is realized by standard fluorescence detection and detection error correction. We note that, our method of $|1_C 1_X 1_Y\rangle$ measurement works only for the state that not populates $|(l > 1)_X\rangle$ and $|(m > 1)_Y\rangle$. Our protocol naturally ensures that $F(0)|\psi\rangle$ fulfills this condition. To make $R_o F(0)|\psi\rangle$ still fulfills, we cannot use R_X and R_Y for the implementation of R_o. Instead, we use S_X (see Eq. (5-23)), and S_Y, which works on Y mode and qubit C similar to S_X.

In experiment, we first let $|\varphi\rangle$ and $|\psi\rangle$ traverse $|0_C 0_X 0_Y\rangle, |0_C 0_X 1_Y\rangle, \cdots, |1_C 1_X 1_Y\rangle$. Hence, we obtain the absolute value of each matrix element of $F(0)$ by square root. Then we obtain the phase of any element as follows. For any base states $|l\rangle$ and $|k\rangle$, by letting $|\varphi\rangle$ traverse $|l\rangle$, $|k\rangle$, $(|l\rangle + |k\rangle)/\sqrt{2}$ and $(|l\rangle + i|k\rangle)/\sqrt{2}$, we can obtain

$$\begin{aligned} & |(\langle l| + \langle k|) F(0) |\psi\rangle|^2 - \left(|\langle l| F(0) |\psi\rangle|^2 + |\langle k| F(0) |\psi\rangle|^2\right) \\ = \ & \langle l| F(0) |\psi\rangle \langle\psi| F(0) |k\rangle + \text{h.c.} \end{aligned} \tag{5-30}$$

$$\begin{aligned} & |(\langle l| - i\langle k|) F(0) |\psi\rangle|^2 - \left(|\langle l| F(0) |\psi\rangle|^2 + |\langle k| F(0) |\psi\rangle|^2\right) \\ = \ & i\langle l| F(0) |\psi\rangle \langle\psi| F(0) |k\rangle - \text{h.c.} \end{aligned} \tag{5-31}$$

Supposing $\langle l| F(0) |m\rangle$ and $\langle k| F(0) |q\rangle$ are matrix elements that satisfy $|\langle l| F(0) |m\rangle| = |\langle k| F(0) |q\rangle| = 1$ in theory, by letting $|\psi\rangle = (|m\rangle + e^{i\phi}|q\rangle)/\sqrt{2}$, we have

$$\arg \frac{\langle k| F(0) |q\rangle}{\langle l| F(0) |m\rangle} \approx \arg \frac{\langle k| F(0) |\psi\rangle}{\langle l| F(0) |\psi\rangle} = \arctan \frac{(5-31)}{(5-30)}. \tag{5-32}$$

In practice, we let $|\psi\rangle$ traverse $(|m\rangle + |q\rangle)/\sqrt{2}$ and $(|m\rangle + i|q\rangle)/\sqrt{2}$, and average their results of Eq. (5-32). We define the phase of $\langle 0_C 0_X 0_Y| F(0) |0_C 0_X 0_Y\rangle$ to be 0, and measure the relative phases between $\langle 0_C 0_X 0_Y| F(0) |0_C 0_X 0_Y\rangle$ and $\langle 1_C 0_X 0_Y| F(0) |1_C 0_X 0_Y\rangle$, $\langle 0_C 0_X 0_Y| F(0) |0_C 0_X 0_Y\rangle$ and $\langle 1_C 0_X 1_Y| F(0) |1_C 1_X 0_Y\rangle$, $\langle 0_C 0_X 0_Y| F(0) |0_C 0_X 0_Y\rangle$ and

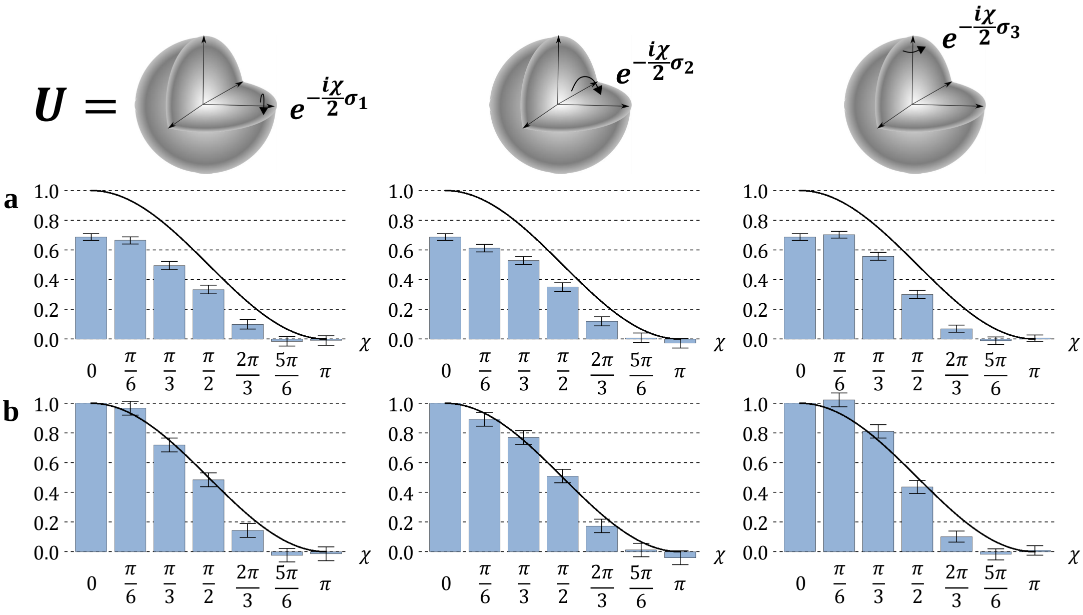

图 5.7 **Experimental results.** Benchmarking results for modular DQC1 with 19 different server supplied unitary operations $U_{k,\chi} = \exp(-i\chi\sigma_k/2)$, where χ ranges over $\{0, \pi/6, \pi/3, \pi/2, 2\pi/3, 5\pi/6, \pi\}$ and $\sigma_k = \sigma_1, \sigma_2, \sigma_3$ ranges over all three standard Pauli directions. (a) displays resulting experimental estimates of $T(U_{k,\chi})$ (blue bars), as compared theoretic predictions (black lines). The disparity is due to decoherence. (b) Calibrating to account for this decoherence enables agreement between theory and experiment.

$\langle 1_C 1_X 0_Y | F(0) | 1_C 0_X 1_Y \rangle$, $\langle 0_C 0_X 1_Y | F(0) | 0_C 0_X 1_Y \rangle$ and $\langle 1_C 0_X 1_Y | F(0) | 1_C 1_X 0_Y \rangle$, $\langle 0_C 0_X 1_Y | F(0) | 0_C 0_X 1_Y \rangle$ and $\langle 1_C 1_X 1_Y | F(0) | 1_C 1_X 1_Y \rangle$, $\langle 0_C 1_X 0_Y | F(0) | 0_C 1_X 0_Y \rangle$ and $\langle 1_C 1_X 0_Y | F(0) | 1_C 0_X 1_Y \rangle$, $\langle 0_C 1_X 0_Y | F(0) | 0_C 1_X 0_Y \rangle$ and $\langle 1_C 1_X 1_Y | F(0) | 1_C 1_X 1_Y \rangle$, $\langle 0_C 1_X 1_Y | F(0) | 0_C 1_X 1_Y \rangle$ and $\langle 1_C 1_X 1_Y | F(0) | 1_C 1_X 1_Y \rangle$. Thus we have the phases of all 8 major elements.

5.2.4 Experimental Benchmarks

Critically, we ensure that our experimental procedure for simulating Alice's modular DQC1 protocol in both *preprocessing* and *postprocessing* stages remain invariant regardless of which U is implemented. Thus, this approach illustrates the basic tenants of modularity – the modular DQC1 protocol itself does not need to change depending on U.

We assess the modular DQC1 protocol for a wide range of possible unitary operations. Specifically, these include the unitaries of the form $U_\sigma(\chi) = \exp(-i\chi\sigma/2)$, where $\sigma \in \{\sigma_1, \sigma_2, \sigma_3\}$ involving all three possible Pauli operators, and $\chi \in \{0, \pi/6, \pi/3, \pi/2, 2\pi/3, 5\pi/6, \pi\}$ as shown in Fig. 5.7. For each choice of U, the protocol was executed 1000 times to obtain an estimate of $|T(U)|^2$ – denoted $M(U)$ – with standard error of approximately 0.02.

We compare these experimental results to their theoretical predictions in Fig. 5.7(a). As we can see, the experimental estimates of $|T(U)|^2$ are significantly less than their true values. The primary causes of this is decoherence, in both the hyperfine and motional levels of the $^{171}\mathrm{Yb}^{+}$ ion. The former is caused by jittering in the Raman beam polzarization and the strength of the magnetic field; the latter by fluctuations in ion trap frequencies.

We can calibrate Alice's estimates of $|T(U)|^2$ to account for much of these errors via a simple model of white noise. Assume that in each run of the experiment, there is a probability λ that the expected output state just prior to measurement is replaced with a maximally mixed state. By linearity of quantum mechanics, Alice's resulting estimates M will then all be offset by a scaling factor of λ, i.e., $M(U) = \lambda|T(U)|^2$. We can thus test her system by acting on the 'identity server' that implements the identity, such that we evaluates $M(I)$ – knowing that this should give us 1 under ideal conditions. In our experiment, the value is $\lambda = 0.69 \pm 0.02$ to a confidence level of 95%. Therefore, We can scale our results by a factor of $1/\lambda$ to account for experimental noise. The re-calibrated estimates for $|T(U)|^2$ are plotted with theoretical predictions in Fig. 5.7(b). As we can see, the experimental results are in agreement with these theoretical predictions.

5.3 Discussion

Here, we experimentally demonstrated the first modular quantum protocol – a variation of the standard DQC1 protocol that allows a device to determine the normalize trace of a completely unknown unitary process U. The experiment illustrates how Alice can outsource part of the computation to Bob - namely the realization of U. Modular architecture has been critical in distributed classical computing. Alice needs no knowledge of how Bob chooses to realize U. The only information Alice and Bob need to share is a agreement on how to communicate quantum information to each other. Our experiment thus presents the first experimental realization of its analogue in the quantum regime.

Our implementation involved the design and realization a coherent quantum swap gate between two motional modes of a trapped ion, controlled on its internal hyperfine states. Our technique presents a more favourable means of scaling than encoding qubits only within the internal states of ions. We illustrate that our techniques can be used to efficiently swap two registers containing many motional modes, controlled on the hyperfine states of single ion. Meanwhile employing higher-energy excitations of the motional modes can enable potential coherent swaps of continuous variable degrees of freedom. These techniques provide possible means of realizing a number of important quantum protocols, including quantum anomaly detection, quantum machine learning on continuous variables[52].

第 6 章　Quantum simulation of fermion-antifermion scattering via boson exchange

Quantum field theories describe a variety of fundamental phenomena in physics. However, their study often involves cumbersome numerical simulations. Quantum simulators, on the other hand, may outperform classical computational capacities due to their potential scalability. Here, we report an experimental realization of a quantum simulation of fermion-antifermion scattering mediated by bosonic modes, using a multilevel trapped ion, which is a simplified model of fermion scattering in both perturbative and nonperturbative quantum electrodynamics. The simulated model exhibits prototypical features in quantum field theory including particle pair creation and annihilation, as well as self-energy interactions. These are experimentally observed by manipulating four internal levels of a $^{171}\mathrm{Yb}^{+}$ trapped ion, where we encode the fermionic modes, and two motional degrees of freedom that simulate the bosonic modes. Our experiment establishes an avenue towards the efficient implementation of field modes, which may prove useful in studies of quantum field theories including nonperturbative regimes.

6.1 Introduction

Quantum simulators are devices designed to predict the properties of physical models associated with target quantum systems[53,54]. Their intrinsic physical behaviors are fully governed by the laws of quantum mechanics, making it possible to efficiently study complex quantum systems that cannot be solved by classical computers[55,56]. Trapped ions and superconducting circuits have proved to be promising for experimentally simulating a variety of paradigmatic quantum models such as various spin models[57–61], relativistic Dirac equations[62–65], embedding quantum simulators[31,32,66–68] and fermionic models[69,70]. More recently, a digital quantum simulation of a fermionic lattice gauge theory has been performed in trapped ions[71]. However, it would be desirable to realize a quantum simulator that involves interacting fermionic and bosonic fields as described by quantum field theories (QFT)[72]. In this sense, fermionic modes could be mapped in the ion internal levels, while bosonic modes could be naturally encoded in the motional degrees of freedom.

Here, we report an experimental quantum simulation of interacting fermionic and bosonic quantum field modes, where fermions are encoded in four internal levels of an $^{171}\mathrm{Yb}^{+}$ ion and the bosonic modes in the motional degrees of freedom, following the proposal by Casanova et al.[73]. Therefore, this analog quantum simulation constitutes a step forward a digital-analog quantum simulator[69,74–77] of perturbative and nonperturbative QFTs. In this sense, a remarkable feature of our experiment is that it contains all orders in perturbation theory, which is equivalent to all Feynman diagrams for a finite number of fermionic and bosonic modes. Moreover, our approach could in principle be scaled up by progressively adding more ions allowing the codification of additional fermionic and bosonic field modes, which may lead to full quantum simulations of QFTs such as quantum electrodynamics (QED)[72].

6.2 Results

6.2.1 Hamiltonian for quantum simulation of quantum field theory

The common way to analyze QFTs is via a Dyson series expansion in perturbation theory and Feynman diagrams[72]. If we consider larger coupling parameters, standard perturbative methods become cumbersome for a finite-mode Dyson expansion, mainly because only a reduced number of perturbative Feynman diagrams can be calculated. On the other hand, a trapped-ion quantum simulator with its high degree of quantum control[17] could overcome these limitations and simulate QFTs more efficiently than classical computers[78]. Based on the proposal of Ref.[73], our experimental quantum simulation of finite-number interacting quantized field modes includes all terms of the Dyson expansion. We experimentally implement a fundamental QFT model in a single trapped-ion considering i) one fermionic and one antifermionic field mode, ii) one or two bosonic field modes, which already reveals interesting QFT features such as self-interactions, particle creation and annihilation, perturbative and nonperturbative regimes. The general Hamiltonian involving the continuum of fermionic and bosonic fields reads

$$\begin{aligned} H &= \int dp\, \omega_p (\hat{b}_p^{\dagger}\hat{b}_p + \hat{d}_p^{\dagger}\hat{d}_p) + \int dk\, \omega_k \hat{a}_k^{\dagger}\hat{a}_k \\ &\quad + g \int dx \psi^{\dagger}(x)\psi(x)A(x), \end{aligned} \tag{6-1}$$

where b_p and d_p are fermionic and antifermionic annihilation operators, respectively, while a_k are the bosonic annihilation operators. Here, ω (ω_k) is the fermion and antifermion free energy (boson free energy), while $\psi(x)$ denotes the fermionic and $A(x)$ the bosonic

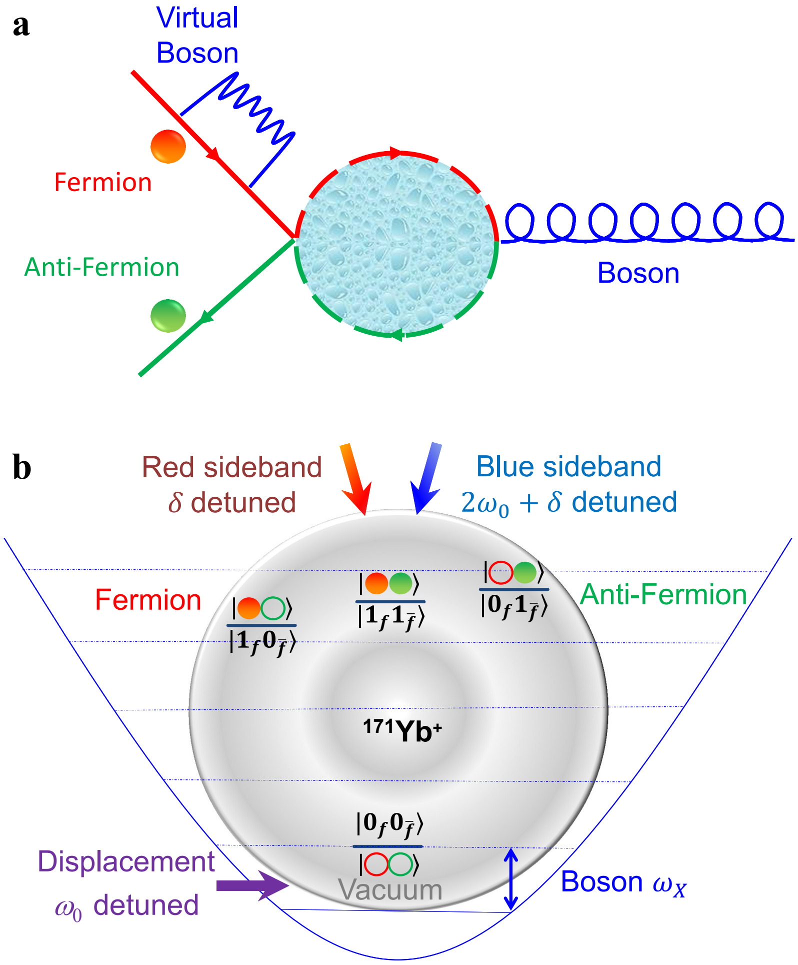
a
Virtual Boson
Fermion
Anti-Fermion
Boson
b
Red sideband
δ detuned
Blue sideband
$2\omega_0 + \delta$ detuned
Fermion
$|1_f0_{\bar{f}}\rangle$
$|1_f1_{\bar{f}}\rangle$
$|0_f1_{\bar{f}}\rangle$
Anti-Fermion
$^{171}\mathrm{Yb}^+$
$|0_f0_{\bar{f}}\rangle$
Vacuum
Displacement
ω_0 detuned
Boson ω_X

图 6.1　**Fermion-antifermion scattering process and its mapping to an $^{171}\mathrm{Yb}^+$ ion system.** (a) Diagram of the interactions between a fermion, an antifermion, and bosons. The fermion emits and absorbs virtual bosons through the self-interaction process. In the fermion-antifermion scattering process, the middle dashed loop represents the summation of all terms in a finite-mode Dyson series expansion. (b) Diagram of the encoding and operations to implement the interaction Hamiltonian H_I with an $^{171}\mathrm{Yb}^+$ trapped ion. The vacuum state and the fermionic states are mapped onto four internal states through the Jordan-Wigner mapping. The bosonic mode is directly implemented with the vibrational mode along the X radial direction. The self-interaction is implemented by a displacement operation, which shifts the center of the harmonic oscillator without changing the internal states. The fermion and anti-fermion scattering is simulated by the combination of the red- and the blue-sideband transitions, which change the internal states together with the vibrational mode.

fields[73].

As a stepped experimental demonstration, we first consider the simplest situation with only one bosonic mode, which can be implemented by a single vibrational mode of the ion. The fermion and antifermion modes are considered as two comoving modes describing incoming Gaussian wave packets, which are centered in the average momentum and have distant average initial positions[73]. These modes describe self-interacting dressed states by emission and absorption of virtual bosons. They also represent the lowest-order in perturbation theory of the scattering of the incoming wave packets that will collide in a certain region of spacetime. The pair creation and annihilation is local and takes place only when the two wave packets of the fermion and antifermion overlap, namely, when the particles scatter. A diagram of these interactions, in the spirit of a Feynman diagram, is shown in Fig. 6.1(a). Note that the loop of this diagram includes all terms in a finite-mode Dyson expansion, which is different from the standard perturbative approach with only a reduced number of Feynman diagrams. By considering slow massive bosons, as described in Ref.[73], the interaction Hamiltonian we would like to realize turns into

$$H_{\mathrm{I}} \;=\; g_1 e^{-i\omega_0 t}(\hat{b}^\dagger \hat{b}\hat{a}_0 + \hat{d}\hat{d}^\dagger \hat{a}_0) + g(t)(e^{i\delta t}\hat{b}^\dagger \hat{d}^\dagger \hat{a}_0 + e^{-i(2\omega_0+\delta)t}\hat{d}\,\hat{b}\,\hat{a}_0) + \mathrm{H.c.}, \tag{6-2}$$

where the associated time-dependent coupling strength is

$$g(t) = g_2 e^{-(t-T/2)^2/(2\sigma_t^2)}, \tag{6-3}$$

and $\delta = \omega_{\mathrm{f}} + \omega_{\bar{\mathrm{f}}} - \omega_0$. Here, ω_{f}, $\omega_{\bar{\mathrm{f}}}$, and ω_0 represent the energy of the fermionic field mode b, the antifermionic field mode d, and the bosonic field mode a_0, respectively. The ratio g_2/g_1 gives the relative strength between pair creation and self-interaction. T is the total time of the pair-creation process while σ_t is the temporal interval of the interaction region. Our formalism, explained in detail in Ref.[73], involves considering incoming comoving fermionic and antifermionic modes at lowest order in perturbation theory. The time dependence of the interaction of the incoming particles, as they collide, maps onto a time dependence of the interaction Hamiltonian coupling.

Applying a Jordan-Wigner mapping[73] from the fermionic modes to a 2 × 2 Hilbert space,

$$\hat{b}^\dagger = \hat{I} \otimes \hat{\sigma}^+, \hat{b} = \hat{I} \otimes \hat{\sigma}^-, \tag{6-4}$$

$$\hat{d}^{\dagger} = \hat{\sigma}^{+} \otimes \hat{\sigma}_z, \hat{d} = \hat{\sigma}^{-} \otimes \hat{\sigma}_z, \tag{6-5}$$

the vacuum state and fermionic states are represented by

$$|{\downarrow\downarrow}\rangle = |0_{\mathrm{f}}0_{\bar{\mathrm{f}}}\rangle, |{\downarrow\uparrow}\rangle = |1_{\mathrm{f}}0_{\bar{\mathrm{f}}}\rangle, |{\uparrow\downarrow}\rangle = -|0_{\mathrm{f}}1_{\bar{\mathrm{f}}}\rangle, |{\uparrow\uparrow}\rangle = -|1_{\mathrm{f}}1_{\bar{\mathrm{f}}}\rangle, \tag{6-6}$$

where $|1_{\mathrm{f}}1_{\bar{\mathrm{f}}}\rangle$ denotes the state containing one fermion and one antifermion. Thus, the interaction Hamiltonian reads

$$\begin{aligned} H_{\mathrm{I}} &= g_1(|0_{\mathrm{f}}0_{\bar{\mathrm{f}}}\rangle\langle 0_{\mathrm{f}}0_{\bar{\mathrm{f}}}| + 2|1_{\mathrm{f}}0_{\bar{\mathrm{f}}}\rangle\langle 1_{\mathrm{f}}0_{\bar{\mathrm{f}}}| + |1_{\mathrm{f}}1_{\bar{\mathrm{f}}}\rangle\langle 1_{\mathrm{f}}1_{\bar{\mathrm{f}}}|)\hat{a}_0 e^{-i\omega_0 t} \\ &- g(t)(|0_{\mathrm{f}}0_{\bar{\mathrm{f}}}\rangle\langle 1_{\mathrm{f}}1_{\bar{\mathrm{f}}}|\hat{a}_0^{\dagger} e^{-i\delta t} + |0_{\mathrm{f}}0_{\bar{\mathrm{f}}}\rangle\langle 1_{\mathrm{f}}1_{\bar{\mathrm{f}}}|\hat{a}_0 e^{-i(2\omega_0+\delta)t}) + \mathrm{H.c.} \end{aligned} \tag{6-7}$$

6.2.2 Trapped ion implementation

We point out that, due to the asymmetric role of fermionic annihilation and antifermionic creation operators in the fermionic field, the one-antifermion state is a dark state of the Hamiltonian in Eq. (2) and therefore the antifermion does not have self-energy at first order (it has, when considering more modes and higher orders). We implement the Hamiltonian on a single $^{171}\mathrm{Yb}^{+}$ ion trapped in a three-dimensional harmonic potential as shown in Fig. 6.1(b). The radial harmonic potential is generated by an oscillating electric field V_{RF} in the radial direction with the two trapping frequencies along X and Y directions being $(\omega_{\mathrm{X}}, \omega_{\mathrm{Y}}) = (2\pi)(2.4, 1.9)$ MHz. The bosonic modes are mapped onto these radial vibrational modes and we choose the X mode for experiments involving a single bosonic mode. The vacuum state $|0_{\mathrm{f}}0_{\bar{\mathrm{f}}}\rangle$ is mapped to the hyperfine state $|F = 0, m = 0\rangle$. Fermionic states are mapped onto Zeeman states as $|F = 1, m_F = -1\rangle \equiv |1_{\mathrm{f}}0_{\bar{\mathrm{f}}}\rangle$, $|F = 1, m_F = 1\rangle \equiv |0_{\mathrm{f}}1_{\bar{\mathrm{f}}}\rangle$ and $|F = 1, m_F = 0\rangle \equiv |1_{\mathrm{f}}1_{\bar{\mathrm{f}}}\rangle$. With the mapping of the bosonic mode and the fermionic states onto the $^{171}\mathrm{Yb}^{+}$ ion system, the Hamiltonian (6-7) is naturally divided into three parts: displacement, red-sideband and blue-sideband operations.

The operations of the self-interaction and scattering processes of the fermion and the anti-fermion are realized by σ_{+}-polarized Raman laser beams[79–81] counter-propagating along the direction of the magnetic field $\vec{B}$. The strength of the magnetic field at the position of the ion is around 7 G, which produces $\omega_{\mathrm{ZM}} = (2\pi)10$ MHz Zeeman splitting. The magnetic field is generated by a pair of Helmholtz coils and is aligned along the

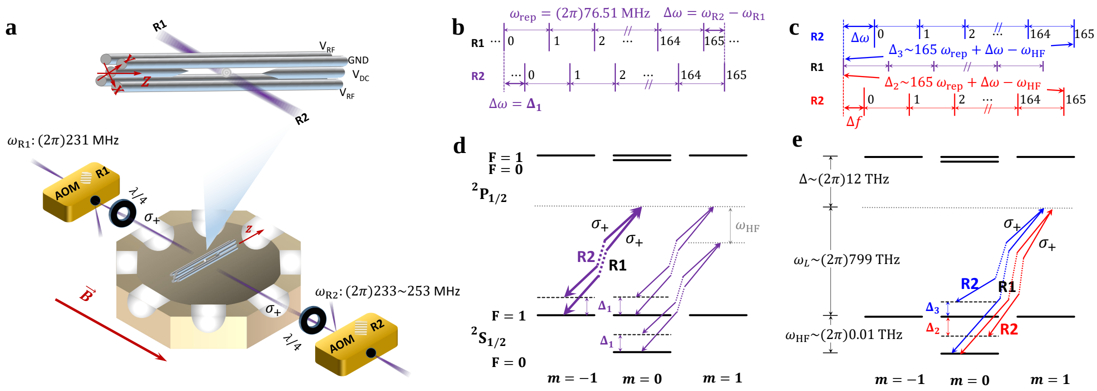
a
R1
V_RF
GND
V_DC
V_RF
R2
ω_R1: (2π)231 MHz
AOM R1
λ/4
σ+
z
B
σ+
λ/4
ω_R2: (2π)233~253 MHz
AOM R2
b
ω_rep = (2π)76.51 MHz   Δω = ω_R2 − ω_R1
R1 … 0 1 2 … 164 165 …
R2 … 0 1 2 … 164 165
Δω = Δ1
c
R2 Δω 0 1 2 … 164 165
Δ3~165 ω_rep + Δω − ω_HF
R1
Δ2~165 ω_rep + Δω − ω_HF
R2 0 1 2 … 164 165
Δf
d
F = 1
F = 0
2P1/2
σ+
σ+
R2
R1
ω_HF
Δ1
Δ1
F = 1
2S1/2
F = 0
m = −1
m = 0
m = 1
e
Δ~(2π)12 THz
ω_L~(2π)799 THz
ω_HF~(2π)0.01 THz
σ+
σ+
R2
R1
Δ3
Δ2
R2
m = −1
m = 0
m = 1

图 6.2　**Schematic of the experimental implementation.** (a) Experimental setup of the 4-rod ion trap inside an octagon vacuum chamber and the geometry of Raman laser beams through the acousto-optic modulators (AOM R1 and R2). The two AOMs are driven with different frequencies ω_{R1} and ω_{R2}, where ω_{R1} is fixed at $(2\pi)231$ MHz and ω_{R2} is adjusted in the range of $(2\pi)233 \sim 253$ MHz. Quarter-wave plates are used for polarization adjustment of the laser beams. (b,c) Frequency combs of the pico-second pulsed lasers and choice of the effective Raman beat-note frequency. The frequency interval of the “comb” is the repetition rate of the laser pulse, which is stabilized at $\omega_{\text{rep}} = (2\pi)76.51$ MHz. The frequency difference between the two AOMs is tuned near to the trap frequency ω_X (b) for the displacement operation or (c) to produce the hyperfine frequency with the addition of 165 intervals, ω_{HF}. (d,e) The basic level structure and transitions of $^{171}\text{Yb}^+$ system coupled by σ_+ polarized Raman laser beams. The beat-note frequency of the Raman beams (d) for the displacement operation is $\Delta_1 = \omega_X - \omega_0$, where $\omega_0 = (2\pi)0.01$ MHz. Thick lines represent the two times stronger displacement operation on state $|1_f 0_{\bar{f}}\rangle$. (e) The frequency difference between the carrier transition and the red-sideband (blue sideband) operation is $\Delta_2 = \omega_X - \delta$ ($\Delta_3 = \omega_X - (2\omega_0 + \delta)$).

angle bisector direction of the X and Y axes, which allows the laser beams to couple both of the vibrational modes, as shown in Fig. 6.2(a). The laser beams are modulated with acousto-optic modulators (AOMs), which are driven with different frequencies ω_{R1} and ω_{R2}.

For the Raman transitions, the mode-locked pico-second laser is used with a wavelength of 375 nm, which is $\Delta = (2\pi)12$ THz red detuned from the optical transition $^2S_{1/2} \leftrightarrow {}^2P_{1/2}$. The train of laser pulses in the time domain can be considered as an equally spaced frequency "comb"[82], which in our experiment had a repetition rate of $\omega_{\mathrm{rep}} = (2\pi)76.51$ MHz. As shown in Figs. 6.2(b)(c), we utilize the frequency "comb" to select a Raman beat-note frequency according to the relation $\omega_{\mathrm{R}} = \Delta\omega + n \times \omega_{\mathrm{rep}}$, where $\Delta\omega = \omega_{\mathrm{R2}} - \omega_{\mathrm{R1}}$, and $n = 0, \pm1, \pm2, \cdots$. For transitions between different motional levels of the same electronic state, we simply use $n = 0$ and make $\Delta\omega$ close to ω_{X} or ω_{Y}. For transitions between two different electronic states, we use $n = 165$.

Figure 6.2(d)(e) shows the Raman schemes needed to implement Hamiltonian (6-7), which are naturally divided into three parts, namely,

$$g_1(|0_f 0_{\bar f}\rangle\langle 0_f 0_{\bar f}| + 2\,|1_f 0_{\bar f}\rangle\langle 1_f 0_{\bar f}| + |1_f 1_{\bar f}\rangle\langle 1_f 1_{\bar f}|)a_0 e^{-i\omega_0 t} \tag{6-8}$$

$$-g(t)\,|0_f 0_{\bar f}\rangle\langle 1_f 1_{\bar f}|\,a_0^\dagger e^{-i\delta t} \tag{6-9}$$

$$-g(t)\,|0_f 0_{\bar f}\rangle\langle 1_f 1_{\bar f}|\,a_0 e^{-i(2\omega_0+\delta)t}. \tag{6-10}$$

Here, the first part is ω_0-detuned displacement operation, the second part is δ-detuned red-sideband operation between $|0_f 0_{\bar f}\rangle \leftrightarrow |1_f 1_{\bar f}\rangle$, and the last part is $(2\omega_0 + \delta)$-detuned blue-sideband operation between $|0_f 0_{\bar f}\rangle \leftrightarrow |1_f 1_{\bar f}\rangle$.

The first part corresponds to a displacement operation with 1 : 2 : 1 : 0 relative ratios among the strength coefficients of states $|0_{\mathrm{f}}0_{\bar{\mathrm{f}}}\rangle$, $|1_{\mathrm{f}}0_{\bar{\mathrm{f}}}\rangle$, $|1_{\mathrm{f}}1_{\bar{\mathrm{f}}}\rangle$ and $|0_{\mathrm{f}}1_{\bar{\mathrm{f}}}\rangle$. Figure 6.2(d) shows how to implement the displacement operation through the counter-propagating Raman laser beams shown in Fig. 6.2(a). The σ_+-polarized Raman beams produce the exact ratios in the strength of displacement operations since state $|1_{\mathrm{f}}0_{\bar{\mathrm{f}}}\rangle$ is coupled to two levels in the $^2P_{1/2}$ manifold, states $|0_{\mathrm{f}}0_{\bar{\mathrm{f}}}\rangle$ and $|1_{\mathrm{f}}1_{\bar{\mathrm{f}}}\rangle$ to one level, and state $|0_{\mathrm{f}}1_{\bar{\mathrm{f}}}\rangle$ to no level. The strength coefficient of a Raman path is given by $\Omega_{\mathrm{R}} = g_1 g_2/2\Delta_{\mathrm{R}}$, where g_1 and g_2 are Rabi frequencies of the two Raman beams coupled to the transition between $^2S_{1/2}$ and $^2P_{1/2}$ and the detuning $\Delta_{\mathrm{R}} \approx \Delta = (2\pi)12$ THz. The coefficients of all possible Raman paths are added since all optical transitions between $^2\mathrm{S}_{1/2} \leftrightarrow {}^2\mathrm{P}_{1/2}$ states have the same coefficients in absolute values. We note that the frequency difference $\omega_{\mathrm{HF}} = (2\pi)12.6$ GHz between states $|0_{\mathrm{f}}0_{\bar{\mathrm{f}}}\rangle$ and $|1_{\mathrm{f}}1_{\bar{\mathrm{f}}}\rangle$ is much smaller than the detuning Δ of the Raman laser beams acting on the manifold $^2P_{1/2}$, which produces around a 0.1% difference in the strength of the displacement operations. Finally we measure the strength of the displacement operations and observe the ratios (see Methods). In principle, we can also implement other ratios of displacement operations by applying additional σ_- and π-polarized Raman beams (see Methods).

The second and third parts are realized by the red- and the blue-sideband transitions as shown in Fig. 6.2(e). The time-dependent strength-coefficient $g(t)$ in Eq. (6-3) is implemented by the change of laser intensity, which is proportional to the RF power on the AOMs of Fig. 6.2(a). We generate the time-dependent RF signal from an arbitrary waveform generator (AWG) and apply it to the AOM R2. By using the AWG, we can generate all the necessary RF frequencies and powers, which realizes the full Hamiltonian (6-7) containing the displacement operation, red- and blue-sideband transitions.

6.2.3 Experimental procedure of the quantum simulation

In the experiment, we initialize the motional and internal state of the ion to the state $|0_{\mathrm{f}}0_{\bar{\mathrm{f}}}, n = 0\rangle$ by standard Doppler cooling, resolved sideband cooling and optical pumping[83,84]. The residual average phonon number and the heating rate are measured to be $\langle n\rangle$=0.016±0.025 and 3.8±1.2 quanta s^{-1}, respectively. The heating effect can be neglected in the typical duration of a single simulation, which is of less than 2 ms. Then we implement the target Hamiltonian (6-7) and let the system evolve for a time t. Finally, we measure the average boson number $\langle n\rangle$ and the populations of various fermionic states, as well as the correlation between the bosonic mode and the fermionic state. A detailed discussion of the measurement procedures can be found in the Methods section. We compare the experimental results with the ideal theoretical calculations. In our simple situation of single bosonic, fermion and anti-fermion modes, we are able to numerically calculate the exact evolution with the full Hamiltonian and find a perturbation method that works for a short time dynamics. The whole evolution is then computed by accumulation of the latter. We note that such numerical methods would not be allowed as the system size grows. Typically, one considers the size corresponding to 50 qubits to be intractable. For example, a realistic situation with 16 ions, 16 modes, and 8 considered levels per mode would be beyond the capabilities of classical computers.

6.2.4 Self-interaction and particle creation and annihilation

We first study the fermion self-interaction processes by setting $g_2 = 0$, starting from the initial state $|1_\mathrm{f}0_{\bar{\mathrm{f}}}, 0_b\rangle$. Then the self-interacting dynamics occurs via the couplings $|1_\mathrm{f}, 0_{\bar{\mathrm{f}}}, n_b\rangle \rightarrow |1_\mathrm{f}, 0_{\bar{\mathrm{f}}}, n_b \pm 1\rangle$. Fig. 6.3(a) shows experimental data for the time-dependent bosonic vacuum populations and the average boson numbers for different self-interaction strengths $g_1/\omega_0 = 0.1$, and 0.15, which quantitatively coincide with the theoretical calculations within experimental errors. We clearly observe the expected emission and reabsorption processes of virtual bosons and the growth of the average number of virtual bosons with the self-interaction strength g_1.

Subsequently we realize the annihilation of a fermion-antifermion pair and the creation of bosons with parameters $g_1 = 0.01\omega_0, g_2 = 0.21\omega_0, \sigma_t = 3/\omega_0$. We choose the initial state to be the state with a fermion-antifermion pair and no bosons: $|1_\mathrm{f}1_{\bar{\mathrm{f}}}, n = 0\rangle$. Fig. 6.3(b) shows the dynamics of the fermion-antifermion scattering process via the population of the fermionic-pair state and the average boson number. It can be clearly seen that the initial fermion-antifermion pair disappears, creating a single boson.

Next, we realize the process of scattering with parameters $g_1 = 0.1\omega_0, g_2 = \omega_0, \sigma_t = 4/\omega_0$, where $g_2 \geq \omega_0$. In this regime, the interaction Hamiltonian (6-2) cannot be regarded as a perturbation. In such a strong coupling situation, we cannot easily discriminate the contributions from the self-interaction and pair production processes. When the initial fermion-antifermion pair disappears, more than a single boson is created in the process as shown in Fig. 6.3(c), which is qualitatively different from the dynamics shown in Fig. 6.3(b). Since the size of the Hilbert space is not too large, we numerically calculate the dynamics of the Hamiltonian by direct numerical integration (see Methods), which is in agreement with the experimental results shown in Fig. 6.3(c). However, as the number of fermion-antifermion pairs and bosons increases, the exact numerical calculation will be intractable by classical means. We have also developed a perturbation method based on the observation that, for a reasonably small time $g_2 t \ll 1$, the effect of the coupling term g_2 does not produce a divergence in the dynamics. We divide the total time of the process by 100 and apply the perturbation method (see Methods) to the unitary evolution operator in each time slice. We find that after including terms up to the 7th order in the perturbation parameter, the deviation of the perturbative dynamics from the complete one is below 10^{-4}. However, even this approach, based on a perturbative expansion within time slices, would be difficult to use for large Hilbert space dimensions with more fermions

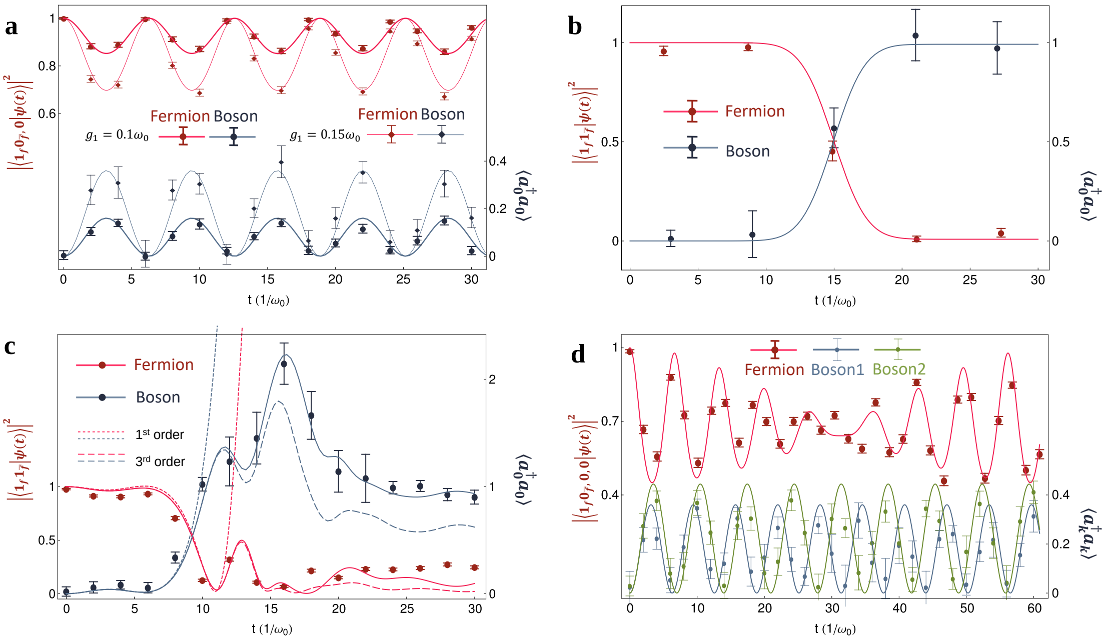

图 6.3　**Trapped-ion simulation results of QFTs.** Dots are experimental data and lines are numerical simulation curves. (a) Self-interaction process for parameters $g_1 = 0.1\omega_0, 0.15\omega_0$, $g_2 = 0$, $\delta = 0$ and $T = 30/\omega_0$, where $|\psi(t)\rangle$ is the state at time t, evolved from $|\psi(0)\rangle = |1_f 0_{\bar{f}}, n = 0\rangle$. Red curves and left axis are for the population of state $|1_f 0_{\bar{f}}, n = 0\rangle$. Blue curves and right axis are for the average number of virtual bosons $\left\langle a_0^\dagger a_0\right\rangle$. (b) Fermion and antifermion annihilation process for parameters $g_1 = 0.01\omega_0$, $g_2 = 0.21\omega_0$, $\sigma_t = 3/\omega_0$, where $|\psi(t)\rangle$ is the state evolved from $|\psi(0)\rangle = |1_f 1_{\bar{f}}, n = 0\rangle$. Red curves and left axis are for the population of state $|1_f 1_{\bar{f}}\rangle$. Blue curves and right axis are for the average number of bosons $\left\langle a_0^\dagger a_0\right\rangle$. (c) The process in the strong coupling, where both of self-interaction and pair production processes strongly influence on the dynamics. Parameters are $g_1 = 0.1\omega_0$, $g_2 = \omega_0$ and $\sigma_t = 4/\omega_0$, and the initial state the same as for **b**. Solid lines are obtained by exact numerical simulation using the built-in solver of the ordinary differential equation in Mathematica (see Methods). Dashed lines are computed by a Dyson series expansion with Feynman diagrams up to 1st and 3rd orders after dividing the whole time by 100 (see Methods). By including the Dyson series up to the 7th order, the deviations from the exact numerical calculation below 10^{-4} (see Methods and Fig. 6.4.). (d) Self-interaction process for two bosonic modes $\omega_1 = \omega_0$, $\omega_2 = 0.9\omega_0$, with parameters $g_1 = 0.15\omega_0$, $g_2 = 0$, $\delta = 0$ and $T = 30/\omega_0$, where $|\psi(t)\rangle$ is the evolved state from $|\psi(0)\rangle = |1_f 0_{\bar{f}}, n_1 = 0, n_2 = 0\rangle$. Red curves and left axis are for population of $|1_f 0_{\bar{f}}, n_1 = 0, n_2 = 0\rangle$. Blue, green curves and right axis are for average number of virtual bosons $\left\langle a_k^\dagger a_k\right\rangle$, $k = 1, 2$. All error bars in experimental data above represent the standard deviation of 100 measurements.

and bosons.

Finally, as a demonstration of scalability, we realize fermion self-interaction processes extended to 2 bosonic modes by using both X and Y phonon modes of a single trapped ion. We set $g_1 = 0.15\omega_0$, the first boson mode frequency $\omega_1 = \omega_0$ and the second boson mode frequency $\omega_2 = 0.9\omega_0$. We note that the g_1 (g_2) coupling to the mode Y (X) is negligible since the detuning to the mode Y (X) is larger by a factor of 50, which effectively suppresses the strength by the same amount. We choose the initial state to contain one fermion and no bosons, $|1_{\mathrm{f}}0_{\bar{\mathrm{f}}}, n_1 = 0, n_2 = 0\rangle$. Then the self-interacting dynamics is given by the transition $|1_{\mathrm{f}}0_{\bar{\mathrm{f}}}, n_1, n_2\rangle \leftrightarrow |1_{\mathrm{f}}0_{\bar{\mathrm{f}}}, n_1 \pm 1, n_2 \pm 1\rangle$. Since the bosonic modes have different frequencies, we observe that the considered fermion emits and reabsorbs bosons differently from the single-boson case. Instead of a sine curve, we see a clear beat-note behavior of the fermionic population as shown in Fig. 6.3(d). We also clearly observe the dynamics of both bosonic modes in a good agreement with the theoretical expectation. By increasing the number of bosonic modes, we would simulate the continuous regime of bosonic modes, which would be related to scattering experiments. In such large number of bosonic modes, the non-perturbative behavior of fermionic or antifermonic mode could be intractable. On the way of increasing bosonic modes, a technology of correlation measurement of multiple phonon modes could be applied[41,85].

6.3 Discussion

In conclusion, this work considers an experimental quantum simulation of interacting fermionic and bosonic quantum field modes. Our approach could be in principle scaled up by progressively incorporating more fermionic and bosonic field modes, which may lead to a full-fledged digital-analog quantum simulation of quantum field theories such as QED[72–74] or the Holstein model[86], where correlations between multiple fermions and phonons have critical relevance. In our current experimental system, an extension to multi-fermion and multi-phonon (bosonic) modes could in principle be implemented by loading a number of ions in a single trap, where the spins of ions map the fermionic modes through Jordan-Wigner transformation[74] and the vibrational modes of ions directly map the bosonic modes. The many-body operators or spin-spin interactions appearing after mapping of the fermionic modes onto spins can be efficiently implemented via a combination of two Mølmer-Sørensen gates and a local gate as shown in Ref.[74]. Other than the spin-spin interactions in the Holstein model, for example, the couplings between fermionic modes and bosonic modes can be implemented by the same Raman laser beams that are individually addressing single ions and tuned to specific mode frequencies. In this respect, it has been shown that the number of gates grows polynomially as the number of fermions and bosons[86]. Ref.[86] also discussed the estimated infidelities from the gate errors in realistic experimental decoherence condition up to four sites, which clearly showed the degree of control is more demanding when the coupling strengths between the modes increase. As demonstrated in our experiment, we do not observe any clear degradation of the simulation when using two modes, though here we do not have the technical problem of individual addressing. We may implement the model in a fully analogue way together with proper spin-spin interactions[87–89], which would allow us to study the pairing or polaron physics occurring in many unconventional superconducting systems[90,91] with the controls of various parameters. In particular, we remark that already with 16 two-level ions and 8 phononic levels per ion, one could perform quantum simulations of interacting quantum field modes that are beyond the reach of classical computations, that is, a Hilbert space dimension of $16^{16} \sim 2^{64}$, which would otherwise re-quire a lengthy quantum algorithm with 64 qubits[92,93]. This experiment opens an avenue that aims at out-performing the limitations of classical computers, with in principle scalable quantum simulations.

We also point out that there are no known efficient classical algorithms for simulating interacting fermionic models in arbitrary spatial dimensions, while with our approach, with a trapped-ion quantum simulator, fermionic models in arbitrary dimensions could be analyzed with polynomial resources[74]. The verification of our proposed scalable experiment requires polynomial resources, as for the detection of the number of bosonic excitations produced, or the population of the fermionic or antifermionic states, only a polynomial number of measurements is required.

6.4 Methods

6.4.1 Uniform red sideband

The “uniform red sideband”[94–96] is implemented as an adiabatic transition where the transfer speed between $|0_{\mathrm{f}}0_{\bar{\mathrm{f}}}, n\rangle$ and $|1_{\mathrm{f}}1_{\bar{\mathrm{f}}}, n-1\rangle$ is the same for all $n = 1, 2, \cdots$. It is realized by adding a time-dependent amplitude $A(t) = \sin(\pi t/d)$ and a time-dependent phase $\phi(t) = -1/\beta \sin(\pi t/d)$ to the normal red-sideband operation, and some additional terms to compensate for the AC Stark shift. Here $d = c\,\pi_{\mathrm{red}}$ is the duration of the transition,

$\beta = ((l+1)(h+1))^{-1/4}/c$ is an empiric parameter depending on the lower bound l and the upper bound h of the phonon number n. We typically choose c to be 10, such that the transition duration d is $c/2 = 5$ times the red-sideband operation period. Therefore, we achieve more than 99 % of theoretical fidelity for all phonon numbers between l and h.

6.4.2 Displacement strength adjustment

We experimentally measure several strength coefficients to check the strength ratios depending on the electronic states. We first prepare the initial state $|m, n=0\rangle$, where $|m\rangle$ is either $|0_\mathrm{f}0_{\bar{\mathrm{f}}}\rangle$ or $|1_\mathrm{f}0_{\bar{\mathrm{f}}}\rangle$. Then we apply the displacement operation for a small period τ. After this, we should obtain a coherent state $|m, \alpha\rangle$, $\alpha = \Omega\tau$, where Ω is the desired strength coefficient. Subsequently, with several different τ, we fit the parameter Ω by measuring each time the remaining population on state $|m, n=0\rangle$ with the "uniform red sideband" method, which should be $e^{-\alpha^2} = e^{-\Omega^2\tau^2}$. After careful beam alignment and quarter wave plate adjustment, the measured strength coefficients of $|0_\mathrm{f}0_{\bar{\mathrm{f}}}\rangle$ and $|1_\mathrm{f}0_{\bar{\mathrm{f}}}\rangle$ are $(2\pi)7.2$ kHz and $(2\pi)14.4$ kHz, respectively, which are consistent with the theory ratio $1:2$.

Since the magnetic quantum number is conserved during the displacement operation, two virtual optical transitions in a Raman path should have the same polarization. If both polarizations are purely σ_-, then the relative strength-coefficient ratio between states $|0_\mathrm{f}0_{\bar{\mathrm{f}}}\rangle$, $|1_\mathrm{f}0_{\bar{\mathrm{f}}}\rangle$, $|1_\mathrm{f}1_{\bar{\mathrm{f}}}\rangle$ and $|0_\mathrm{f}1_{\bar{\mathrm{f}}}\rangle$ is $1:0:1:2$. If both polarizations are purely π, then the relative strength-coefficient ratio between states $|0_\mathrm{f}0_{\bar{\mathrm{f}}}\rangle$, $|1_\mathrm{f}0_{\bar{\mathrm{f}}}\rangle$, $|1_\mathrm{f}1_{\bar{\mathrm{f}}}\rangle$ and $|0_\mathrm{f}1_{\bar{\mathrm{f}}}\rangle$ is $1:1:1:1$. In general, if the ratio between σ_+, σ_- and π polarization is $a:b:c$, then the relative strength-coefficient ratio between states $|0_\mathrm{f}0_{\bar{\mathrm{f}}}\rangle$, $|1_\mathrm{f}0_{\bar{\mathrm{f}}}\rangle$, $|1_\mathrm{f}1_{\bar{\mathrm{f}}}\rangle$ and $|0_\mathrm{f}1_{\bar{\mathrm{f}}}\rangle$ is $a+b+c : 2a+c : a+b+c : 2b+c$.

6.4.3 Fermionic state measurement

To measure $P(|1_\mathrm{f}1_{\bar{\mathrm{f}}}\rangle)$, we simply apply a π rotation between states $|0_\mathrm{f}0_{\bar{\mathrm{f}}}\rangle$ and $|1_\mathrm{f}1_{\bar{\mathrm{f}}}\rangle$ to swap their populations, with a microwave horn. Then the measured population of state $|0_\mathrm{f}0_{\bar{\mathrm{f}}}\rangle$ is equal to the original $P(|1_\mathrm{f}1_{\bar{\mathrm{f}}}\rangle)$.

To measure $P(|1_\mathrm{f}0_{\bar{\mathrm{f}}}, n=0\rangle)$, however, we need a phonon projective measurement[94–96]. Instead of using fluorescence detection together with a post-selection scheme, which may introduce significant heating errors because of photon scattering, here we use an auxiliary state as a swap buffer. Note that the interaction Hamiltonian (6-7) does not have terms related to state $|0_\mathrm{f}1_{\bar{\mathrm{f}}}\rangle$. Therefore, we employ state $|0_\mathrm{f}1_{\bar{\mathrm{f}}}\rangle$ as the auxiliary state and always initialize it to zero. We first apply three consecutive π swap gates between $|0_\mathrm{f}0_{\bar{\mathrm{f}}}\rangle$ and $|0_\mathrm{f}1_{\bar{\mathrm{f}}}\rangle$, $|1_\mathrm{f}1_{\bar{\mathrm{f}}}\rangle$ and $|1_\mathrm{f}0_{\bar{\mathrm{f}}}\rangle$. After these operations, $|1_\mathrm{f}1_{\bar{\mathrm{f}}}\rangle$ is swapped with $|1_\mathrm{f}0_{\bar{\mathrm{f}}}\rangle$, and $|0_\mathrm{f}1_{\bar{\mathrm{f}}}\rangle$ is swapped with $|0_\mathrm{f}0_{\bar{\mathrm{f}}}\rangle$. Then we apply a "uniform red sideband" π rotation to swap the population in $|0_\mathrm{f}0_{\bar{\mathrm{f}}}, n > 0\rangle$ with that of $|1_\mathrm{f}1_{\bar{\mathrm{f}}}, n-1\rangle$. Then, we measure the remaining vacuum-state population, $P(|0_\mathrm{f}0_{\bar{\mathrm{f}}}\rangle, n = 0)$, which is equal to the original population, $P(|1_\mathrm{f}0_{\bar{\mathrm{f}}}, n = 0\rangle)$. The uncertainty of the measurement mainly comes from the quantum projection noise of binary result of single measurements[97].

For the experiment involving two boson modes, we first measure $P(|1_\mathrm{f}0_{\bar{\mathrm{f}}}, n_1 = 0\rangle)$ using the same method as that of the single-boson case. Next we consecutively apply a "uniform red sideband" to the first mode and another "uniform red sideband" to the second mode. Then, we measure the population of the upper state, which should be $P(|1_\mathrm{f}0_{\bar{\mathrm{f}}}, n_1 = 0, n_2 > 0\rangle)$. Therefore, we obtain the desired population from the relation: $P(|1_\mathrm{f}0_{\bar{\mathrm{f}}}, n_1 = 0, n_2 = 0\rangle) = P(|1_\mathrm{f}0_{\bar{\mathrm{f}}}, n_1 = 0\rangle) - P(|1_\mathrm{f}0_{\bar{\mathrm{f}}}, n_1 = 0, n_2 > 0\rangle)$. Note that this scheme is clearly scalable in the number of bosonic modes.

6.4.4 Average boson number measurement

For the average boson number measurement, we first use optical pumping to trace out electronic states[96] and then apply a blue sideband time sweep from $t = 0$ to $t = 12\ \pi_{\mathrm{blue}}$[98]. We get the phonon number distribution by fitting the result signals through the maximum likelihood method with parameters of the Fock state populations[94,95]. The main uncertainty in the average phonon measurement comes from fitting and we include one standard deviation as an uncertainty throughout the manuscript.

6.4.5 Ideal theoretical calculations

The exact dynamics of the Hamiltonian (6-7) can be obtained by solving the time-dependent Schrödinger equation $i\hbar\frac{\partial}{\partial t}|\psi(t)\rangle = H_I(t)|\psi(t)\rangle$. We numerically solve the equation with the built-in function of Mathematica, ąőNDSolveąŕ, which finds a numerical solution to the ordinary differential equation mainly based on Runge-Kutta method. In the numerical calculation, we include 4 internal levels and up to 10 phonons per mode for the Hamiltonian (6-7), which changes the Schrödinger equation to the ordinary differential equation with 40 and 400 components for single mode and two modes of the state $|\psi\rangle$, respectively. With the option of infinite Maxsteps in Mathematica, the numerical

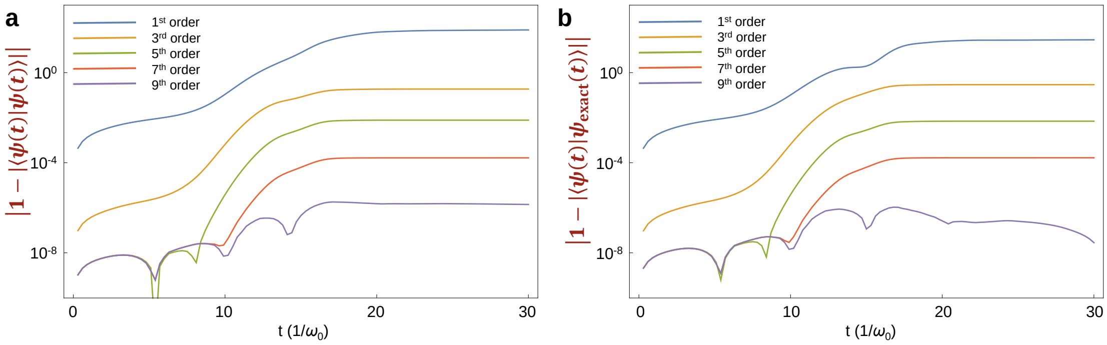

图 6.4 **Convergence of Dyson series.** In order to evaluate the validity of the perturbation calculations, we use **a,** the norm of the state from 1, $|1 - |\langle\psi(t)|\psi(t)\rangle||$ and **b,** the infidelity of the state, $|1 - |\langle\psi_{\mathrm{exact}}(t)|\psi(t)\rangle||$, where $\psi_{\mathrm{exact}}(t)$ is the result of the ideal numerical calculation, for the case shown in Fig. 6.3(c) with $M = 100$ divisions of time. After including up to 7th order perturbation, the deviation of the norm from 1 and the infidelity reduce to below 10^{-4}. We note that for the case of Fig. 6.3(b), even the first and the second order perturbations provide the deviation of the norm and infidelity below 5×10^{-2} and 2×10^{-4}, respectively.

calculations converge and do not show any error messages. We point out that all the parameters in the simulation are experimentally determined, not obtained via fitting. The main limitation of the numerical calculation would be the size of the Hilbert space when we scale up the system with multiple fermions and bosons.

6.4.6 Feynman diagram calculation

In the interaction picture, the evolution operator $U_I(t, t_0)$ satisfies the following differential equation

$$i\hbar\frac{\partial}{\partial t}U_{\mathrm{I}}(t, t_0) = H_{\mathrm{I}}(t)U_{\mathrm{I}}(t, t_0), \tag{6-11}$$

which can be exactly solved as the so-called Dyson series,

$$U_{\mathrm{I}}(t, t_0) = \sum_{n=0}^{\infty}\left(-\frac{i}{\hbar}\right)^n \int_{t_0}^{t} dt_1 \dots \int_{t_0}^{t_{n-1}} dt_n H_{\mathrm{I}}(t_1)\dots H_{\mathrm{I}}(t_n). \tag{6-12}$$

By introducing the time-ordering operator $\mathcal{T}$, the above solution can be written in a formally succinct way $U_{\mathrm{I}}(t, t_0) = \mathcal{T}\exp\left(-\frac{i}{\hbar}\int_{t_0}^{t} H_{\mathrm{I}}(s)ds\right)$.

Truncating at some finite N in Eq. (6-12) provides a straightforward perturbation treatment of the evolution operator $U_{\mathrm{I}}(t, t_0)$. However, when the evolution time increases, the unitarity of the perturbation expansion becomes difficult to guarantee, because the truncation error is proportional to $(t-t_0)^{N+1}$. In order to deal with the long-time dynamics, we make use of the composition property of the evolution operator and interleave $M-1$ equally spaced points between t_0 and t. Then the evolution operator $U_{\mathrm{I}}(t,t_0)$ is identically written as the product of M evolution operators, each of which governs the dynamical evolution over a short period of time,

$$U_{\mathrm{I}}(t_0,t)=\prod_{m=1}^{M}U_{\mathrm{I}}\left(t_m,t_{m-1}\right), \tag{6-13}$$

with $t_M\equiv t$. For any dynamics with finite duration, saying $t-t_0$ is finite, we can always assign a sufficiently large M so that $\Delta t\equiv t_m-t_{m-1}$ is a small but finite quantity. Consequently, $U_{\mathrm{I}}(t_m,t_{m-1})$ is readily to be treated perturbatively.

Denote the n-th order perturbation expansion of $U_{\mathrm{I}}(t_m,t_{m-1})$ as $U_{\mathrm{I}}^{(N)}(t_m,t_{m-1})$,

$$U_{\mathrm{I}}^{(N)}(t_m,t_{m-1})=\sum_{n=0}^{N}\left(-\frac{i}{\hbar}\right)^{n}\int_{t_{m-1}}^{t_m}ds_1\ldots\int_{t_{m-1}}^{s_{n-1}}ds_nH_{\mathrm{I}}(s_1)\ldots H_{\mathrm{I}}(s_n). \tag{6-14}$$

Then the whole dynamics can be treated perturbatively as follows,

$$U_{\mathrm{I}}(t,t_0)=\prod_{m=1}^{M}U_{\mathrm{I}}^{(N)}(t_m,t_{m-1})+O\left(\frac{(t-t_0)^{N+1}}{M^N}\right). \tag{6-15}$$

The deviations are related to the number of sliced sections M in time and the order of perturbations N. In our numerical calculations of the Dyson series, we divide the total time by $M=100$ and apply the perturbations up to $N=9$th order. Fig. 6.4 shows the deviations of the norm from 1, $|1-|U_{\mathrm{I}}(t,t_0)\,|\psi(t_0)\rangle\,|^2|$ and the infidelity $|1-|\,\langle\psi_{\mathrm{exact}}(t)|U_{\mathrm{I}}(t,t_0)|\psi(t_0)\rangle\,||$ depending on the order of the perturbations for the case of Fig. 6.3(c). Here $\psi_{\mathrm{exact}}(t)$ is the result by the ideal numerical calculation. From the 7th order, the deviations in the perturbation calculation are below 10^{-4} from the ideal norm of 1.

第 7 章 Entangling Ions through Multiple Transverse Modes in an Ion-Chain

We develop a multi-qubit gate, which entangles any selected ions in an ion-chain by simultaneously coupling them to multiple transverse collective motional modes. By using multi-segment phase-modulated Raman laser array, our gate decouples the internal states from all the motional modes in the end and provides correct geometric phases. Our gate is more scalable than the traditional Mølmer-Sørensen (MS) gate[99]. In MS gate, it is essential to use only one motional mode, which should be well isolated from all the other modes. However, as the number of ions increases, it becomes increasingly difficult to maintain the isolation requirement with reasonable trap frequencies, which leads to a drop of fidelity of MS gate. On the other hand, our gate in principle promises perfect fidelity regardless of the number of ions. We benchmark the performance of our multi-qubit gate by its ability of creating Greenberger-Horne-Zeilinger (GHZ) state. Experimentally, for the moment, we have made a progress of performing gate

$$\exp\left[-i\frac{\pi}{4}\left(\sigma_{\mathrm{x}}^{(0)}\sigma_{\mathrm{x}}^{(1)}+\sigma_{\mathrm{x}}^{(1)}\sigma_{\mathrm{x}}^{(2)}+\sigma_{\mathrm{x}}^{(2)}\sigma_{\mathrm{x}}^{(0)}\right)\right]$$

on 3 trapped $^{171}\mathrm{Yb}^{+}$ ions, and creating GHZ state $(|000\rangle+|111\rangle)/\sqrt{2}$ with fidelity of 91.21%. Our multi-qubit gate provides a scalable solution for trapped-ion quantum computation and simulation.

7.1 Introduction

In trapped-ion system, ions are coupled through their shared vibrational modes. Usually, we are aiming for a multi-qubit gate

$$U=\exp\left[-i\sum_{i,j=0}^{N-1}\chi_{i,j}\sigma_{\mathrm{x}}^{(i)}\sigma_{\mathrm{x}}^{(j)}\right], \tag{7-1}$$

where N is the number of ions, and $\chi_{i,j}$ is proportional to the coupling strength between ion i and ion j. Traditionally, such operation is implement by a approach proposed by Mølmer and Sørensen[99].

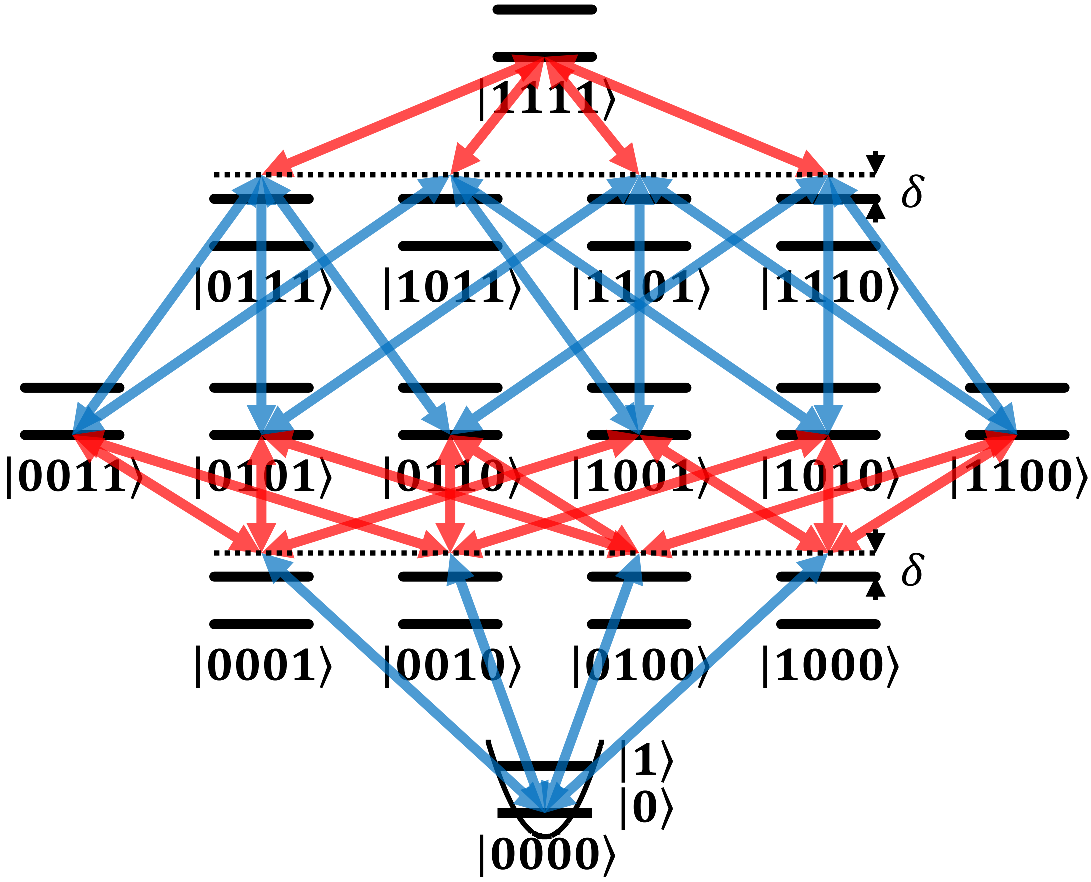

图 7.1　**4-qubit Mølmer-Sørensen (MS) gate.** An MS gate uses detuned red and blue sidebands to implement ion-ion couplings. If the number of ions N is an even number, a transition between $|00\cdots0\rangle$ and $|11\cdots1\rangle$ is eventually realized.

7.1.1　Mølmer-Sørensen (MS) gate

The principle of MS gate is to use Raman force to couple ions and motional modes. Usually, for the high fidelity of MS gate, only one mode is used[100]. By applying bichromatic beat notes, composed of a detuned (red-detuned by angular frequency δ) red sideband and a detuned (blue-detuned by angular frequency δ) blue sideband, Raman lasers generate state-dependent forces described by Hamiltonian

$$H = \hbar\Omega\frac{ae^{i\delta t} + a^{\dagger}e^{-i\delta t}}{2}\sum_{i=0}^{N-1}\eta_i\sigma_{\mathrm{x}}^{(i)}, \tag{7-2}$$

where Ω is the Rabi frequency of carrier transition of each ion, and η_i is the Lamb-Dicke parameter of ion i and the mode. At certain conditions (e.g. $\eta_i\Omega \ll \delta$), the effect of

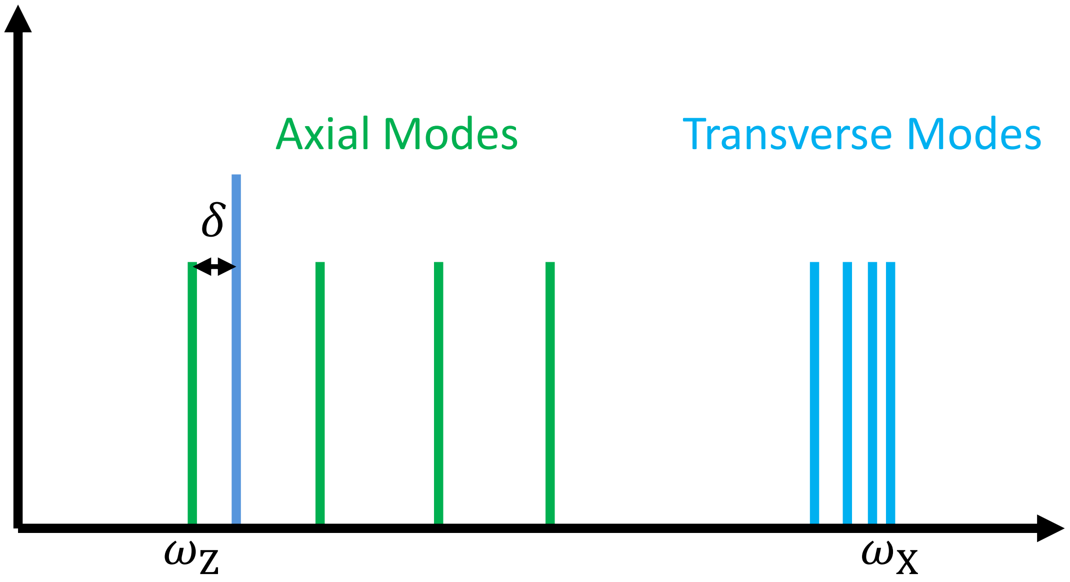

图 7.2　**Mode-frequency distribution in 4-ion case.**

state-dependent forces becomes ion-ion couplings, described by effective Hamiltonian

$$H_{\text{eff}} = \frac{\hbar\Omega^2}{4\delta}\sum_{i,j=0}^{N-1}\eta_i\eta_j\sigma_{\text{x}}^{(i)}\sigma_{\text{x}}^{(j)}. \tag{7-3}$$

A typical way of performing MS gate is to use only axial center-mass (CM) mode. The property of a CM mode is that it couples each ion with same strength, which results in same Lamb-Dicke parameter $\eta_i = \eta$. Therefore, the effective coupling strength of each ion-pair is identical (see Eq. (7-3)). With certain duration, the MS gate implements unitary operation

$$U = \exp\left[-i\frac{\pi}{8}\sum_{i,j=0}^{N-1}\sigma_{\text{x}}^{(i)}\sigma_{\text{x}}^{(j)}\right], \tag{7-4}$$

which can be used to create a Greenberger-Horne-Zeilinger (GHZ) state (see Fig. 7.1)

$$\frac{|00\cdots0\rangle + e^{i\phi}|11\cdots1\rangle}{\sqrt{2}} = U|00\cdots0\rangle. \tag{7-5}$$

The reason for using an axial mode is that axial modes have larger mode spacing than the transverse modes (see Fig. 7.2). So the axial CM mode can be well isolated from others.

Apart from the isolation condition, 2 other conditions must be fulfilled to implement the MS gate – the ion-chain condition and reasonable radial trap frequency. We note

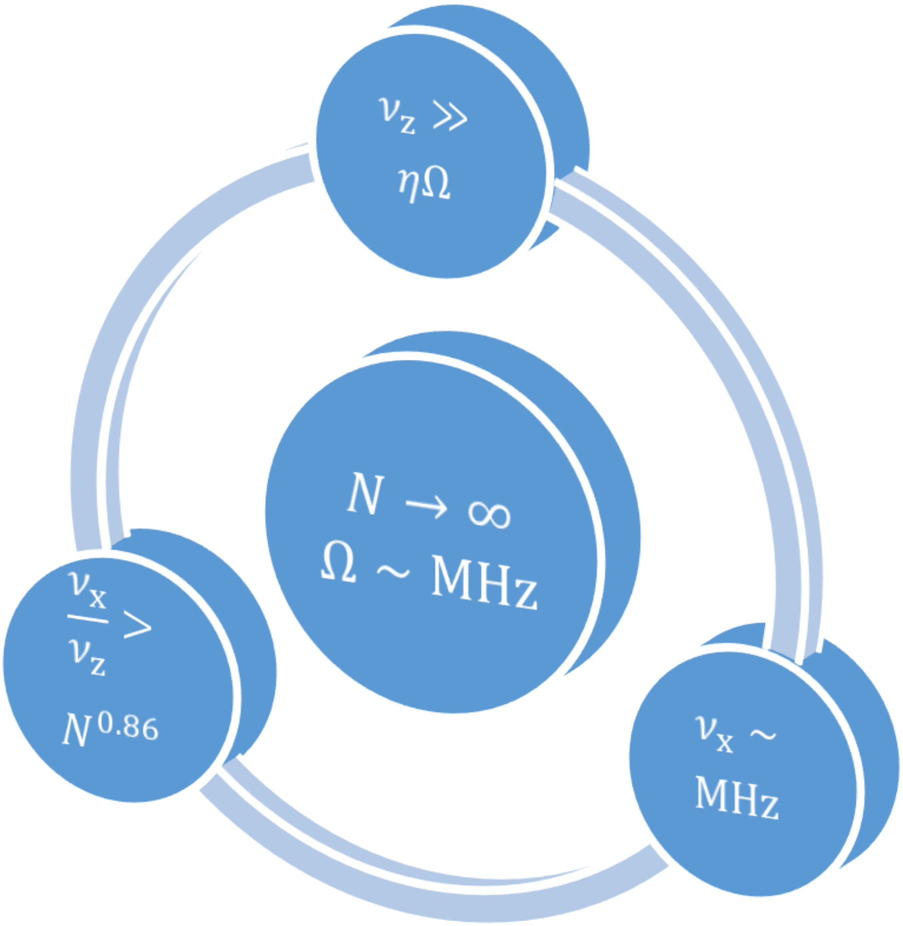
$\nu_z \gg \eta\Omega$
$N \to \infty$
$\Omega \sim \mathrm{MHz}$
$\frac{\nu_x}{\nu_z} > N^{0.86}$
$\nu_x \sim \mathrm{MHz}$

图 7.3 **Impossible trinity.** The isolation condition requires a big axial trap frequency ν_z relative to $\eta\Omega$, where Rabi frequency Ω is in the level of MHz. The ion-chain condition requires $\nu_x/\nu_z > N^{0.86}$. Otherwise, ions shape into a zig-zag or other phases. A reasonable radial trap frequency ν_x is in the level of MHz, due to technical restrictions. As the number of ions N increases, these 3 conditions become contradict to each other.

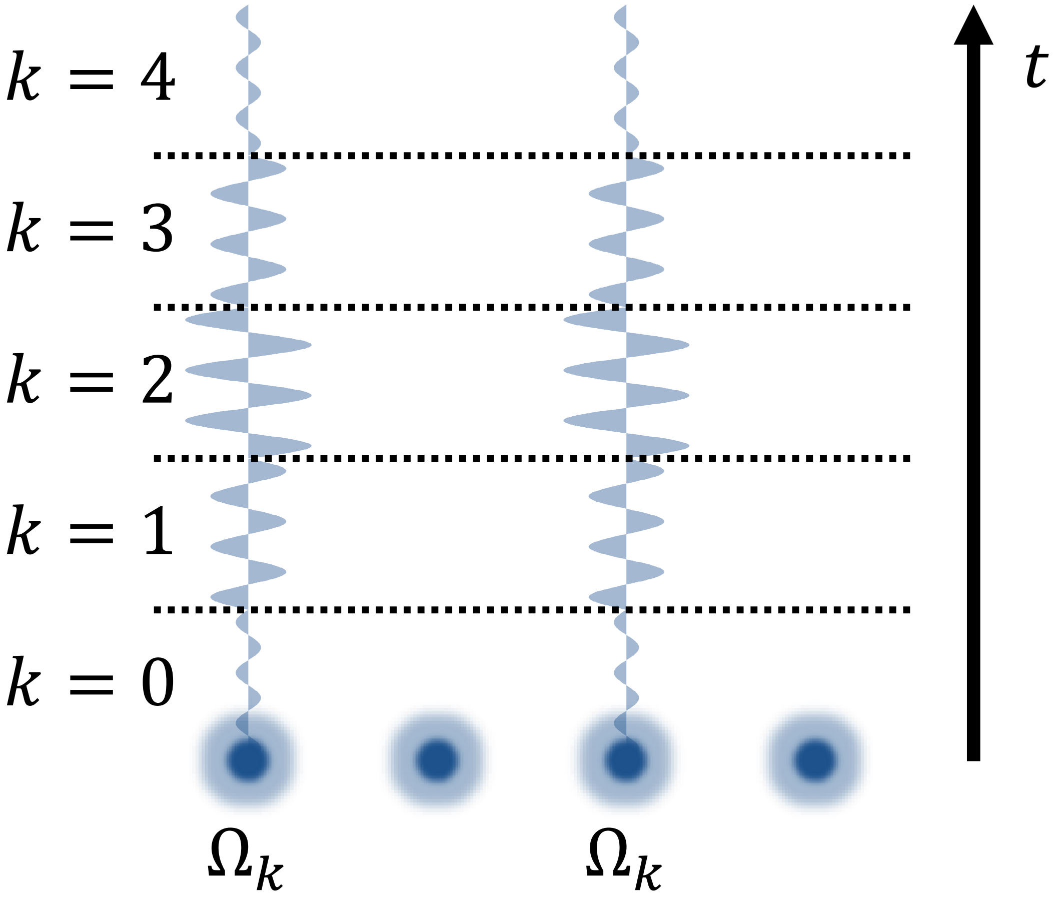

图 7.4　**5-segment Ising (XX) gate.** To couple 2 ions in an ion-chain, 5-segment Raman beams are used to address both ions. Both beams share the same frequency, amplitude and phase. Each segment, however, has its unique amplitude.

that, as N increases, these 3 conditions become contradict to each other. So the MS gate approach is not scalable.

7.1.2　5-segment Ising (XX) gate

A scalable multi-qubit gate must break 1 of 3 conditions. Then another scheme was proposed[101,102]. It uses multiple modes to couple ions instead of single mode. In this way, the isolation condition can be removed.

They use 5-segment Raman beams to address any 2 ions in an ion-chain, and perform Ising gate on them with high fidelity[101]. Both beams share the same frequency, amplitude and phase. Each segment, however, has its unique amplitude (see Fig. 7.4). Because the isolation condition no longer exists, the 5-segment gate uses transverse modes. Like MS gate, these Raman beams still generate state-dependent forces[103,104]. In each segment, the effect of state-dependent forces is described by Hamiltonian

$$H_k = \hbar\Omega_k \sum_l \left(\eta_{i,l}\sigma_{\mathrm{x}}^{(i)} + \eta_{j,l}\sigma_{\mathrm{x}}^{(j)}\right) \frac{a_l e^{i(\mu-\nu_l)t} + a_l^\dagger e^{-i(\mu-\nu_l)t}}{2}, \tag{7-6}$$

where μ is the frequency difference between detuned red (blue) sideband and carrier transition, and ν_l is the frequency of transverse mode l.

The total effect of this Hamiltonian is described by unitary operation

$$U = \exp\left[\sum_l \left(\left(\alpha_{i,l}\sigma_{\mathrm{x}}^{(i)} + \alpha_{j,l}\sigma_{\mathrm{x}}^{(j)}\right) a_l^\dagger - \mathrm{H.c.}\right) - i\chi\sigma_{\mathrm{x}}^{(i)}\sigma_{\mathrm{x}}^{(j)}\right], \tag{7-7}$$

where $\alpha_{i,l}$ ($\alpha_{j,l}$) stands for a state-dependent displacement of mode j caused by ion i (j), and χ is proportional to the coupling strength between ion i and ion j. By controlling μ and Ω_k, all α can be set to almost 0. It means the gate decouples ions from all the motional modes in the end. And only ion-ion coupling is left. Therefore, Eq. (7-1) is implemented in 2-qubit case.

Our work is to extend this approach to more than 2 qubits. In our gate, we still use the multi-segment scheme. But we use phase modulation instead of amplitude modulation. Because Ω_k, which are affected by many factors in our system, are always difficult to control.

7.2 Methods

Our gate uses multi-segment phase-modulated beams to address all ions in an ion-chain. In each segment, our gate uses state-dependent forces to implement ion-mode couplings

$$H_k = \hbar \sum_{i=0}^{N-1} \Omega_i \left(\sigma_{\mathrm{y}}^{(i)} \cos[\mu t + \phi] + \sigma_{\mathrm{x}}^{(i)} \sum_l \eta_{i,l} \frac{a_l e^{i((\mu-\nu_l)t+\phi_{i,k})} + \mathrm{H.c.}}{2}\right). \tag{7-8}$$

Here all beams in all segments share same μ. The Rabi frequency Ω_i of ion i is independent of segment-index k (amplitude of each beam is not modulated). Each beam in each segment has a unique phase $\phi_{i,k}$. Unlike 5-segment gate, we also consider term $\hbar\Omega_i\sigma_{\mathrm{y}}^{(i)} \cos[\mu t + \phi]$, which is the direct coupling of ion i and its corresponding Raman beam.

The total effect of this Hamiltonian is described by unitary operation

$$U = \exp\left[\sum_{i,l} \sigma_{\mathrm{x}}^{(i)} \left(\alpha_{i,l} a_l^{\dagger} - \mathrm{H.c.}\right) - i \sum_i \chi_i \sigma_{\mathrm{y}}^{(i)} - i \sum_{i,j} \chi_{i,j} \sigma_{\mathrm{x}}^{(i)} \sigma_{\mathrm{x}}^{(j)}\right], \tag{7-9}$$

where

$$\alpha_{i,l} = i\eta_{i,l} \frac{\Omega_i}{\mu - \nu_l} \sin\left[\frac{\mu - \nu_l}{2} d\right] \sum_k \exp\left[-i(k(\mu - \nu_l)d + \phi_{i,k})\right], \tag{7-10}$$

$$\chi_i = 2\frac{\Omega_i}{\mu} \sin\frac{\mu d}{2} \sum_k \cos[k\mu d + \phi_{i,k}], \tag{7-11}$$

$$\begin{aligned}\chi_{i,j} = \chi_{j,i} = & \frac{\Omega_i \Omega_j}{4} \left(d \sum_l \eta_{i,l}\eta_{j,l} \frac{1 - \mathrm{sinc}[(\mu - \nu_l)d]}{\mu - \nu_l} \sum_k \cos[\phi_{i,k} - \phi_{j,k}] + \right. \\ & \sum_j \eta_{i,l}\eta_{j,l} \frac{1 - \cos[(\mu - \nu_l)d]}{(\mu - \nu_l)^2} \\ & \left. \sum_{k<k'} \left(\sin\left[(k' - k)(\mu - \nu_l)d + \phi_{i,k'} - \phi_{j,k}\right] + \sin\left[(k' - k)(\mu - \nu_l)d + \phi_{j,k'} - \phi_{i,k}\right]\right) \right),\end{aligned} \tag{7-12}$$

and d is the duration of each segment. By setting μd to an integer multiple of 2π, we ensure that $\chi_i = 0$. Further more, by controlling Ω_i and $\phi_{i,k}$, we set all $\alpha_{i,l}$ to 0 and $\chi_{i,j}$ to expected values. Therefore, Eq. (7-1) is implemented. Like MS gate, our gate can also be used to create multi-qubit GHZ state by setting $\chi_{i,j} = \pi/8$ (see Eq. (7-4)(7-5)). We benchmark the performance of our gate by the fidelity of GHZ state.

7.3 Results

Experimentally, we perform our gate on 3 $^{171}\mathrm{Yb}^{+}$ ions with 4-segment Raman beams (see Fig. 7.5). We set $\mu = (2\pi)2.426\,\mathrm{MHz}$, which is near transverse CM mode $\nu_1 = (2\pi)2.443\,\mathrm{MHz}$. The total duration of our gate is $4d = 69.249\,\mu\mathrm{s}$.

During our gate, the motional part of each $\{\sigma_{\mathrm{x}}^{(i)}\}$ eigenstate $|\pm\pm\pm\rangle$ ($|\pm\rangle = (|0\rangle + |1\rangle)/\sqrt{2}$) is a coherent state $|\alpha_1(t)\rangle\,|\alpha_2(t)\rangle\,|\alpha_3(t)\rangle$, where

$$\alpha_l(t) = \sigma_{\mathrm{x}}^{(0)} \alpha_{0,l}(t) + \sigma_{\mathrm{x}}^{(1)} \alpha_{1,l}(t) + \sigma_{\mathrm{x}}^{(2)} \alpha_{2,l}(t). \tag{7-13}$$

The trajectory of $|\alpha_l(t)\rangle$ for each $|\pm\pm\pm\rangle$ is shown in Fig. 7.6. We can see that, at the end of the gate, each trajectory goes back to vacuum state. It means the decoupling of ions

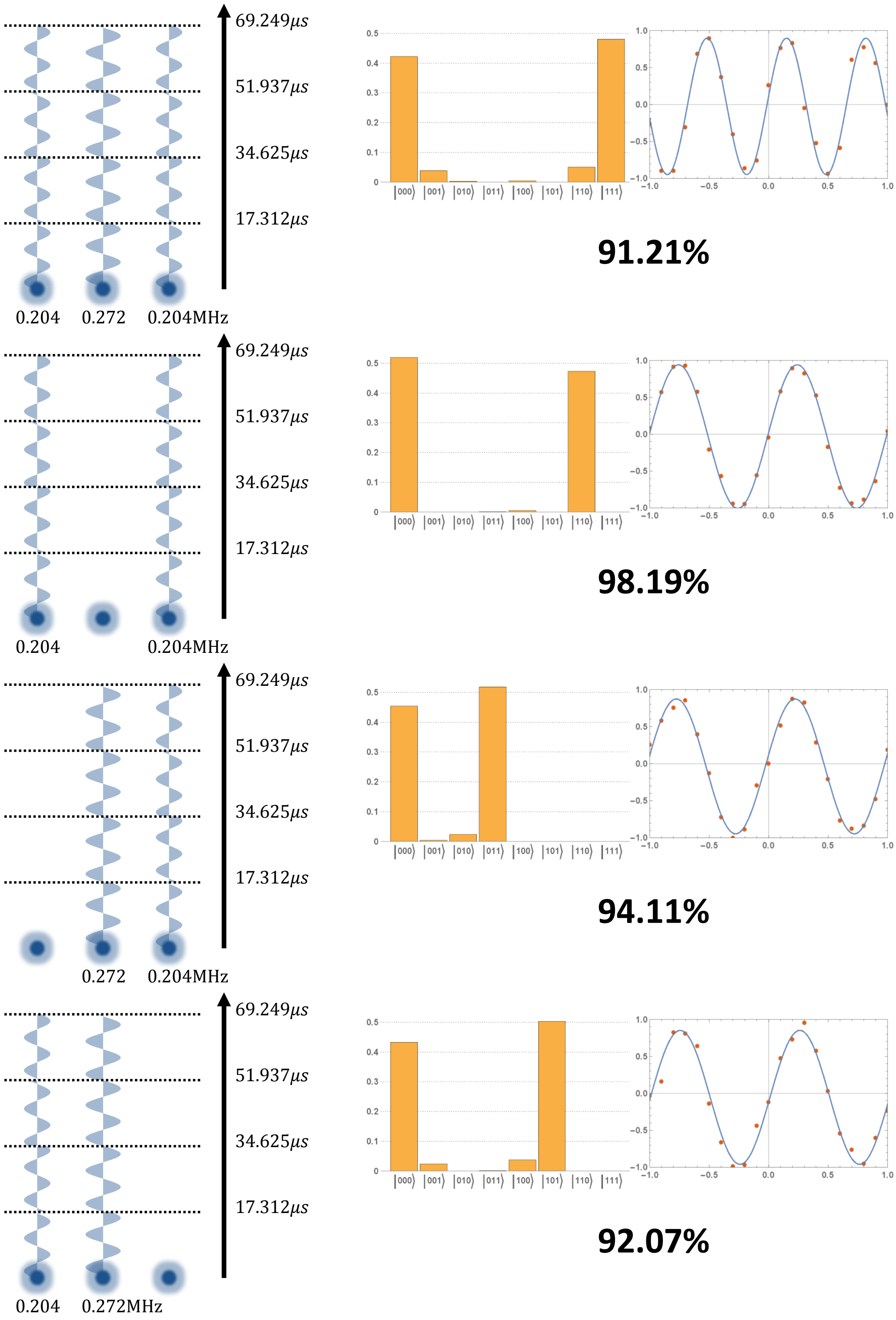

图 7.5 **Results of our multi-qubit gates.**

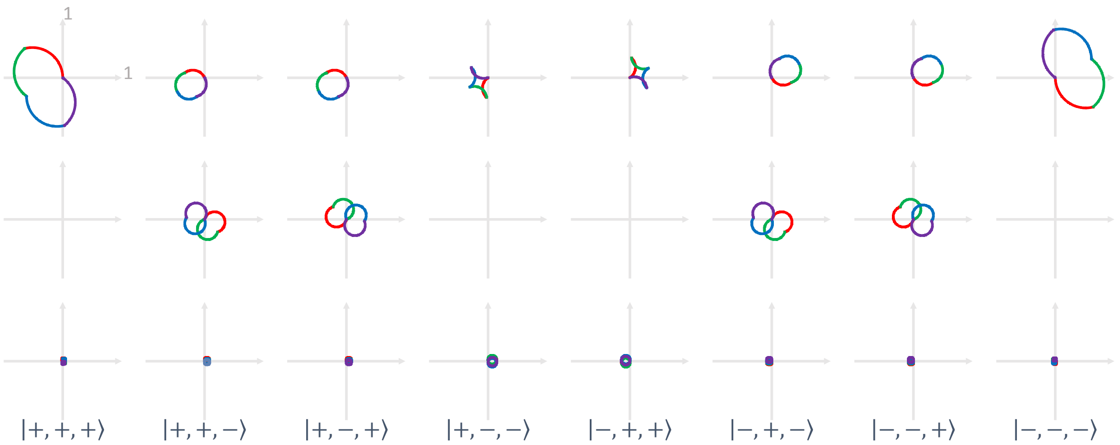

图 7.6 **Trajectory of motional states.** For each internal state $|\pm\pm\pm\rangle$, its part of mode 1 (2 or 3) is a coherent state. The trajectory of coherent state of each mode for each $|\pm\pm\pm\rangle$ is shown in the figure.

and modes.

The total effect of our 3-qubit gate is

$$\exp\left[-i\frac{\pi}{4}\left(\sigma_{\mathrm{x}}^{(0)}\sigma_{\mathrm{x}}^{(1)}+\sigma_{\mathrm{x}}^{(1)}\sigma_{\mathrm{x}}^{(2)}+\sigma_{\mathrm{x}}^{(2)}\sigma_{\mathrm{x}}^{(0)}\right)\right]. \tag{7-14}$$

We use it to create a 3-qubit GHZ state with a fidelity of 91.21% (see Fig. 7.5). An interesting phenomenon of our gate is that, when shutting off the addressing beam on one of the ions, the coupling strength among other ions remains the same. We use it to create 2-qubit GHZ states with fidelity of 98.19%, 94.11% and 92.07%.

7.4 Discussion and Conclusion

In our multi-qubit gate, the error sources are, the fluctuation of Rabi frequencies Ω_i caused by the power fluctuation of Raman lasers, and the decoherence of transverse modes caused by the fluctuation of radial trap frequency ν_{x}.

In our work, theoretically, we develop a multi-qubit gate, which entangles ions by multi-segment phase-modulated beams. Experimentally, we perform our gate on 3 ions and use it to create a 3-qubit GHZ state with fidelity of 91.21%.

In the future, we will experimentally extend our gate to more than 3 qubits. We theoretically prove that the minimal number of segments of our gate is $O(N)$, where N is the number of ions.

第 8 章　Conclusion

During my Ph.D. career, I have learned the physics required in trapped ions, especially the physics that helps implementing quantum gates and quantum algorithms. Now, I am proficient in applying linear algebra, quantum mechanics, atomic and molecular physics, quantum optics and other mathematical and physical knowledges to solve practical problems in experiments.

In project "Operational effects of the UNOT gate on classical and quantum correlations", the effects of the universal NOT (UNOT) gate on classical and quantum correlations between two qubits are explored theoretically and experimentally. A paper has been published in Science Bulletin[9]. I am the first author. In project "Implementation of modular DQC1 in a trapped ion system", the modular DQC1 is implemented in the case of 1-qubit registers. As a by-product, a method of implementing controlled-SWAP gate, which swaps 2 phonon qubits controlled by a ion qubit, is developed. In project "Experimental quantum simulation of fermion-antifermion scattering via boson exchange in a trapped ion", quantum simulation of a quantum field model is conducted. A paper has been published in Nature Communications. I am a joint first author[10]. In project "Entangling ions through multiple transverse modes in an ion-chain", a scalable multi-qubit gate, which creates any spin-spin couplings in an ion-chain, is theoretically developed and experimentally implemented. It is our first project on a multi-ion platform.

During my Ph.D. career, I have also participated in building a complete trapped-ion quantum computing platform, and led the team to build the trapped-ion Raman system, which is upgraded to a multi-ion addressable Raman system now. I know the construction of our platform with great extent. I have originally invented resonant frequency precise measurement, time difference between Raman pulses of different paths precise measurement, single ion qubit and multiple phonon qubits tomography and many other techniques. I have developed softwares for quantum computation in Mathematica, which are being used in our lab.

插图索引

图 2.1 **Detection operation.** A detection operation makes resonant transitions between $|F = 1, m_\mathrm{F} = 0, \pm 1\rangle$ of ${}^2\mathrm{S}_{1/2}$ manifold and $|F = 0, m_\mathrm{F} = 0\rangle$ of ${}^2\mathrm{P}_{1/2}$ manifold. 14

图 2.2 **Optical pumping operation.** A optical pumping operation makes resonant transitions between $|l = 0, F = 1, m_\mathrm{F} = -1\rangle$ and $|l = 1, F = 1, m_\mathrm{F} = -1, 0\rangle$, between $|l = 0, F = 1, m_\mathrm{F} = 0\rangle$ and $|l = 1, F = 1, m_\mathrm{F} = \pm 1\rangle$, and between $|l = 0, F = 1, m_\mathrm{F} = 1\rangle$ and $|l = 1, F = 1, m_\mathrm{F} = 0, 1\rangle$. Possible spontaneous radiations from ${}^2\mathrm{P}_{1/2}$ manifold to ${}^2\mathrm{S}_{1/2}$ manifold also happen during optical pumping. 16

图 3.1 **Main structure of our softwares.** 26

图 4.1 **UNOT gates on spin pairs.** (a) Local reversible operations leave classical correlations $J(\mathrm{B}|\mathrm{A})$ and quantum correlations $\delta(\mathrm{B}|\mathrm{A})$ unchanged, where A and B are two separable spins. A UNOT gate also preserves $J(\mathrm{B}|\mathrm{A})$, but can change $\delta(\mathrm{B}|\mathrm{A})$. (b) We simulate the effect of UNOT on $\rho_{\uparrow\uparrow}$ and $\rho_{\downarrow\uparrow}$, where the two spins are encoded in the internal and external degrees of freedom of a trapped ${}^{171}\mathrm{Yb}^{+}$ ion in a harmonic potential. Spin A is mapped to a 4-level system using Eq. (4-1), spanned by the basis $|0_\mathrm{A}\rangle = |F = 0, m_\mathrm{F} = 0\rangle$ and $|(n = 1, 2, 3)_\mathrm{A}\rangle = |F = 1, m_\mathrm{F} = n - 2\rangle$, where F and m_F characterize the total internal angular momentum of ${}^{171}\mathrm{Yb}^{+}$. The transition frequency from $|F = 0, m_\mathrm{F} = 0\rangle$ to $|F = 1, m_\mathrm{F}\rangle$ is $(2\pi)(12642.8 + 9.0 m_\mathrm{F})$ MHz. Spin B is mapped to the ground and first excited states of external motional mode, denoted by $|0_\mathrm{B}\rangle$ and $|1_\mathrm{B}\rangle$, which are separated by the trap frequency $(2\pi)2.44$ MHz. 43

图 4.2 **Simulation of UNOT Gate on encoded spin A.** While the UNOT gate is unphysical, it can be exactly simulated using a quantum 4-level system. To simulate UNOT acting on state $|\varphi\rangle = \alpha|\uparrow\rangle + \beta|\downarrow\rangle$, we initialize a suitable state $|\bar{\varphi}\rangle = \mathcal{M}|\varphi\rangle$ on the 4-level system (see Eq. (4-1)). The expected output state $|\varphi^{\perp}\rangle = \Theta_{\mathrm{UNOT}}|\varphi\rangle = -\beta^{*}|\uparrow\rangle + \alpha^{*}|\downarrow\rangle$ can then be simulated by applying $\bar{\Theta}_{\mathrm{UNOT}} = |1\rangle\langle 0| - |0\rangle\langle 1| - |3\rangle\langle 2| + |2\rangle\langle 3|$ on $|\bar{\varphi}\rangle$. It is easy to check that $\bar{\Theta}_{\mathrm{UNOT}}|\bar{\varphi}\rangle = \mathcal{M}|\varphi^{\perp}\rangle$. In the ion trap system, $\bar{\Theta}_{\mathrm{UNOT}}$ can be realized with 4 microwave pulses, where $R_n(\pi,\phi) = -i\left(e^{-i\phi}|n_{\mathrm{A}}\rangle\langle 0_{\mathrm{A}}| + \mathrm{h.c.}\right) + \sum_{m\neq 0,n}|m_{\mathrm{A}}\rangle\langle m_{\mathrm{A}}|$, $n = 1, 2, 3$. 47

图 4.3 **Effects of external levels involved operations.** (a)(b)(c) The effects of the red sideband, FLIP and SWAP operations on low motional energy levels. (d) The graphic description of transition $|0_{\mathrm{A}}1_{\mathrm{B}}\rangle \leftrightarrow |2_{\mathrm{A}}0_{\mathrm{B}}\rangle$ caused by $R_{-}(\chi,\phi)$ or $R_{\mathrm{SWAP}}(\chi,\phi)$. 49

图 4.4 **The comparison between theoretical and experimental results of 17 population measurements** for (a) the aligned spin $\rho_{\uparrow\uparrow}$ and (b) the anti-aligned spin $\rho_{\downarrow\uparrow}$. The error bar of each quantity is calculated with confidence level of 95%. 54

图 4.5 **Experimentally measured density operators compared with theoretical predictions.** (a) illustrates the theoretically predicted density operators for $\rho_{\uparrow\uparrow}$ and $\rho_{\downarrow\uparrow}$, where each vertical bar represents a corresponding matrix element. In the first experiment (b), $\rho_{\downarrow\uparrow}$ is prepared with a fidelity of 0.992 ± 0.004. After simulating the UNOT gate, we retrieve $\rho_{\uparrow\uparrow}$ with fidelity of 0.997 ± 0.007. In the second experiment (c), $\rho_{\uparrow\uparrow}$ is prepared with fidelity 0.998 ± 0.004, and the final state approximates $\rho_{\downarrow\uparrow}$ to fidelity 0.997 ± 0.002. The errors are estimated by Monte Carlo methods with a confidence level of 95%. 54

图 4.6 **The effect of UNOT gate on various types of correlations.** The theoretically predicted effect of UNOT gate (blue bars), together with experimentally measured effects when acting on $\rho_{\downarrow\uparrow}$ (purple bars) and $\rho_{\uparrow\uparrow}$ (red bars) are displayed for (a) classical correlations $J(\mathrm{B}|\mathrm{A})$ and (b) quantum correlations $\delta(\mathrm{B}|\mathrm{A})$. (a) Theory predicts that $J(\mathrm{B}|\mathrm{A}) = 0.082$ for both $\rho_{\uparrow\uparrow}$ and $\rho_{\downarrow\uparrow}$. Experimental results agree within experimental error. (b) Theory predicts that $\delta(\mathrm{B}|\mathrm{A})$ is 0.333 for $\rho_{\uparrow\uparrow}$ and 0.126 for $\rho_{\downarrow\uparrow}$ – a difference of 0.207. This agrees with the experiment, where we see respective increase and decrease of 0.22 ± 0.07 and 0.22 ± 0.05 when converting to and from $\rho_{\uparrow\uparrow}$. 55

图 5.1 **The DQC1 and the modular DQC1.** (a) The standard DQC1 algorithm operates by applying U on an n-qubit register controlled by a pure qubit initialized in state $|0\rangle$. Measuring the expectation values of this control qubit with respect to standard Pauli operators $\sigma_1 = |0\rangle\langle 1| + |1\rangle\langle 0|$ and $\sigma_2 = i(|0\rangle\langle 1| - |1\rangle\langle 0|)$ then allows estimation of the real and imaginary components of the normalized trace $T(U)$. The action of U cannot be outsourced to an external server in a modular fashion. (b) Modular DQC1 evaluates $|T(U)|$ instead of $T(U)$ in way in which implementation of U can be out-sourced. In this protocol, Alice introduces a second n-qubit register and prepares ρ_1. She then sends the server one of the n-qubit registers (for example this may be realized by first mapping this register into a medium suitable for communication via a SWAP Gate). On the proviso that the server applies U to the register, she is able to estimate $|T(U)|$ by performing a σ_1 measurement on the control qubit. 60

图 5.2 **Encoding methods.** The control qubit C is encoded within two hyperfine levels of the $\mathrm{S}_{1/2}$ manifold in the $^{171}\mathrm{Yb}^{+}$ ion. Denote these by $|0_{\mathrm{C}}\rangle = |F = 0, m_{\mathrm{F}} = 0\rangle$ and $|1_{\mathrm{C}}\rangle = |F = 1, m_{\mathrm{F}} = 0\rangle$, where F is the quantum number of total internal angular momentum and m_{F} is the magnetic quantum number. The transition frequency between $|0_{\mathrm{C}}\rangle$ and $|1_{\mathrm{C}}\rangle$ is 12642.826 MHz. Qubits X and Y are encoded within the ground and first excited states of two radial motional modes in $^{171}\mathrm{Yb}^{+}$, denoted as $|0_{\mathrm{X}}\rangle$, $|1_{\mathrm{X}}\rangle$ and $|0_{\mathrm{Y}}\rangle$, $|1_{\mathrm{Y}}\rangle$. The trap frequencies of modes X and Y are given by 2.53 MHz and 2.00 MHz. 62

图 5.3 **Conceptual circuits of implementating preprocessing.** In $n = 1$ modular DQC1, each pure state component of ρ_1 (see Eq. (5-5)) is created by each circuit shown in left column. Our implementation processes are conceptually represented by the circuits in right column, where the output of each circuit is the same as the corresponding circuit in left column. 64

图 5.4 **The implementation of control SWAP gate.** A CSWAP operation on X and Y represents coherently interchanging the populations of $|1_\mathrm{C}0_\mathrm{X}1_\mathrm{Y}\rangle$ and $|1_\mathrm{C}1_\mathrm{X}0_\mathrm{Y}\rangle$. In experiment this is achieved as follows: first, we temporarily shelve $|0_\mathrm{C}\rangle$ into an ancillary Zeeman level $|\pm\mathrm{Z_C}\rangle = |F = 1, m_\mathrm{F} = \pm 1\rangle$ by microwave pulses. The Two Zeeman levels $|\mathrm{Z_C}\rangle$ and $|-\mathrm{Z_C}\rangle$ are employed sequentially with equal duration, so that the AC stark shift and energy level jittering of both Zeeman levels cancel. The transition between $|0_\mathrm{C}\rangle$ and $|\pm\mathrm{Z_C}\rangle = |F = 1, m_\mathrm{F} = \pm 1\rangle$ is realized by a microwave pulse with frequency $12642.819 \pm 9.507 m_\mathrm{F}$ MHz. Meanwhile the SWAP operation that interchanges $|1_\mathrm{C}0_\mathrm{X}1_\mathrm{Y}\rangle$ and $|1_\mathrm{C}1_\mathrm{X}0_\mathrm{Y}\rangle$ is realized by 3 sequential Raman pulses. Subsequently, the shelved $|0_\mathrm{C}\rangle$ is restored by a second microwave pulse. 67

图 5.5 **Scalability of the CSWAP gate.** A CSWAP gate with n-qubit registers, as shown in left circuit, is equivalent to a combination of n CSWAP gates with 1-qubit registers, as shown in right circuit. 68

图 5.6 **The truth table of control SWAP gate.** Visual representation of relevant probabilities and the phases of the CSWAP gate in the computational basis. The area of orange disk on the l^{th} column and m^{th} row reflects the probability of obtaining corresponding output $|l\rangle$ given corresponding input $|m\rangle$, where l, m range over all binary representations of the 3 encoded qubits. So the radius of the disk is proportional to $|\langle l| F |m\rangle|$. Meanwhile, the orientation of each black arrow on the disk gives the phase information of corresponding element $\langle l| F |m\rangle$. The radius and orientation of the blue disk represents an amplitude of 1 and a phase of 0. Note that the negative phase $\langle 1_\mathrm{C}0_\mathrm{X}1_\mathrm{Y}| F |1_\mathrm{C}1_\mathrm{X}0_\mathrm{Y}\rangle = -1$ is consequence of the choice of physical realization, and does not affect computational output (see 5.2.2.5). 72

图 5.7 **Experimental results.** Benchmarking results for modular DQC1 with 19 different server supplied unitary operations $U_{k,\chi} = \exp(-i\chi\sigma_k/2)$, where χ ranges over $\{0, \pi/6, \pi/3, \pi/2, 2\pi/3, 5\pi/6, \pi\}$ and $\sigma_k = \sigma_1, \sigma_2, \sigma_3$ ranges over all three standard Pauli directions. (a) displays resulting experimental estimates of $T(U_{k,\chi})$ (blue bars), as compared theoretic predictions (black lines). The disparity is due to decoherence. (b) Calibrating to account for this decoherence enables agreement between theory and experiment. 76

图 6.1 **Fermion-antifermion scattering process and its mapping to an $^{171}\mathrm{Yb}^+$ ion system.** (a) Diagram of the interactions between a fermion, an antifermion, and bosons. The fermion emits and absorbs virtual bosons through the self-interaction process. In the fermion-antifermion scattering process, the middle dashed loop represents the summation of all terms in a finite-mode Dyson series expansion. (b) Diagram of the encoding and operations to implement the interaction Hamiltonian H_I with an $^{171}\mathrm{Yb}^+$ trapped ion. The vacuum state and the fermionic states are mapped onto four internal states through the Jordan-Wigner mapping. The bosonic mode is directly implemented with the vibrational mode along the X radial direction. The self-interaction is implemented by a displacement operation, which shifts the center of the harmonic oscillator without changing the internal states. The fermion and anti-fermion scattering is simulated by the combination of the red- and the blue-sideband transitions, which change the internal states together with the vibrational mode. 81

图 6.2 **Schematic of the experimental implementation.** (a) Experimental setup of the 4-rod ion trap inside an octagon vacuum chamber and the geometry of Raman laser beams through the acousto-optic modulators (AOM R1 and R2). The two AOMs are driven with different frequencies ω_{R1} and ω_{R2}, where ω_{R1} is fixed at $(2\pi)231$ MHz and ω_{R2} is adjusted in the range of $(2\pi)233 \sim 253$ MHz. Quarter-wave plates are used for polarization adjustment of the laser beams. (b,c) Frequency combs of the pico-second pulsed lasers and choice of the effective Raman beat-note frequency. The frequency interval of the “comb” is the repetition rate of the laser pulse, which is stabilized at $\omega_{\mathrm{rep}} = (2\pi)76.51$ MHz. The frequency difference between the two AOMs is tuned near to the trap frequency ω_{X} (b) for the displacement operation or (c) to produce the hyperfine frequency with the addition of 165 intervals, ω_{HF}. (d,e) The basic level structure and transitions of $^{171}\mathrm{Yb}^{+}$ system coupled by σ_{+} polarized Raman laser beams. The beat-note frequency of the Raman beams (d) for the displacement operation is $\Delta_1 = \omega_{\mathrm{X}} - \omega_0$, where $\omega_0 = (2\pi)0.01$ MHz. Thick lines represent the two times stronger displacement operation on state $|1_{\mathrm{f}}0_{\bar{\mathrm{f}}}\rangle$. (e) The frequency difference between the carrier transition and the red-sideband (blue sideband) operation is $\Delta_2 = \omega_{\mathrm{X}} - \delta$ ($\Delta_3 = \omega_{\mathrm{X}} - (2\omega_0 + \delta)$). 84

图 6.3 **Trapped-ion simulation results of QFTs.** Dots are experimental data and lines are numerical simulation curves. (a) Self-interaction process for parameters $g_1 = 0.1\omega_0, 0.15\omega_0, g_2 = 0, \delta = 0$ and $T = 30/\omega_0$, where $|\psi(t)\rangle$ is the state at time t, evolved from $|\psi(0)\rangle = |1_{\mathrm{f}}0_{\bar{\mathrm{f}}}, n = 0\rangle$. Red curves and left axis are for the population of state $|1_{\mathrm{f}}0_{\bar{\mathrm{f}}}, n = 0\rangle$. Blue curves and right axis are for the average number of virtual bosons $\left\langle a_0^\dagger a_0 \right\rangle$. (b) Fermion and antifermion annihilation process for parameters $g_1 = 0.01\omega_0$, $g_2 = 0.21\omega_0$, $\sigma_t = 3/\omega_0$, where $|\psi(t)\rangle$ is the state evolved from $|\psi(0)\rangle = |1_{\mathrm{f}}1_{\bar{\mathrm{f}}}, n = 0\rangle$. Red curves and left axis are for the population of state $|1_{\mathrm{f}}1_{\bar{\mathrm{f}}}\rangle$. Blue curves and right axis are for the average number of bosons $\left\langle a_0^\dagger a_0 \right\rangle$. (c) The process in the strong coupling, where both of self-interaction and pair production processes strongly influence on the dynamics. Parameters are $g_1 = 0.1\omega_0$, $g_2 = \omega_0$ and $\sigma_t = 4/\omega_0$, and the initial state the same as for **b**. Solid lines are obtained by exact numerical simulation using the built-in solver of the ordinary differential equation in Mathematica (see Methods). Dashed lines are computed by a Dyson series expansion with Feynman diagrams up to 1st and 3rd orders after dividing the whole time by 100 (see Methods). By including the Dyson series up to the 7th order, the deviations from the exact numerical calculation below 10^{-4} (see Methods and Fig. 6.4.). (d) Self-interaction process for two bosonic modes $\omega_1 = \omega_0, \omega_2 = 0.9\omega_0$, with parameters $g_1 = 0.15\omega_0, g_2 = 0, \delta = 0$ and $T = 30/\omega_0$, where $|\psi(t)\rangle$ is the evolved state from $|\psi(0)\rangle = |1_{\mathrm{f}}0_{\bar{\mathrm{f}}}, n_1 = 0, n_2 = 0\rangle$. Red curves and left axis are for population of $|1_{\mathrm{f}}0_{\bar{\mathrm{f}}}, n_1 = 0, n_2 = 0\rangle$. Blue, green curves and right axis are for average number of virtual bosons $\left\langle a_k^\dagger a_k \right\rangle$, $k = 1, 2$. All error bars in experimental data above represent the standard deviation of 100 measurements. 88

图 6.4 **Convergence of Dyson series.** In order to evaluate the validity of the perturbation calculations, we use **a,** the norm of the state from 1, $|1 - |\langle\psi(t)|\psi(t)\rangle||$ and **b,** the infidelity of the state, $|1 - |\langle\psi_{\text{exact}}(t)|\psi(t)\rangle||$, where $\psi_{\text{exact}}(t)$ is the result of the ideal numerical calculation, for the case shown in Fig. 6.3(c) with $M = 100$ divisions of time. After including up to 7th order perturbation, the deviation of the norm from 1 and the infidelity reduce to below 10^{-4}. We note that for the case of Fig. 6.3(b), even the first and the second order perturbations provide the deviation of the norm and infidelity below 5×10^{-2} and 2×10^{-4}, respectively. 93

图 7.1 **4-qubit Mølmer-Sørensen (MS) gate.** An MS gate uses detuned red and blue sidebands to implement ion-ion couplings. If the number of ions N is an even number, a transition between $|00\cdots0\rangle$ and $|11\cdots1\rangle$ is eventually realized. 96

图 7.2 **Mode-frequency distribution in 4-ion case.** 97

图 7.3 **Impossible trinity.** The isolation condition requires a big axial trap frequency ν_z relative to $\eta\Omega$, where Rabi frequency Ω is in the level of MHz. The ion-chain condition requires $\nu_{\text{x}}/\nu_{\text{z}} > N^{0.86}$. Otherwise, ions shape into a zig-zag or other phases. A reasonable radial trap frequency ν_{x} is in the level of MHz, due to technical restrictions. As the number of ions N increases, these 3 conditions become contradict to each other. 98

图 7.4 **5-segment Ising (XX) gate.** To couple 2 ions in an ion-chain, 5-segment Raman beams are used to address both ions. Both beams share the same frequency, amplitude and phase. Each segment, however, has its unique amplitude. 99

图 7.5 **Results of our multi-qubit gates.** 102

图 7.6 **Trajectory of motional states.** For each internal state $|\pm\pm\pm\rangle$, its part of mode 1 (2 or 3) is a coherent state. The trajectory of coherent state of each mode for each $|\pm\pm\pm\rangle$ is shown in the figure. 103

图 A.1 **Vacuum system** 131

表格索引

表 4.1 **Pulse sequences of FLIP and SWAP operations.** In the SWAP operation, $\alpha = \arccos\left[\csc(\pi/\sqrt{2})\sin(\chi/4)\right]$ and $\gamma = \phi - \arccos\left[\cot(\pi/\sqrt{2})\tan(\chi/4)\right]$. 49

表 4.2 **Preparation of aligned or anti-aligned spin pairs in 6 directions.** We obtain the 5th pair $|0_\mathrm{A}0_\mathrm{B}\rangle$ by standard sideband cooling process. Other 11 pairs are generated from $|0_\mathrm{A}0_\mathrm{B}\rangle$ with corresponding sequences in the right column. 51

表 4.3 **Information of the measurements in the tomography.** We measure each population $P = \langle\psi|\,\rho\,|\psi\rangle/2 = \langle\bar{\psi}|\,\bar{\rho}\,|\bar{\psi}\rangle$ (see Eq. (4-8)) in the left column, where $|\psi\rangle$ and $|\bar{\psi}\rangle$ are listed in the middle and right column respectively. .. 52

表 5.1 **Implementation of preprocessing.** Each sequence shown in the right column implements the corresponding operation shown in the left column. 65

表 5.2 **Implementation of postprocessing.** Here $\alpha = \arccos\left[\csc(\pi/\sqrt{2})/\sqrt{2}\right]$ and $\gamma = \phi - \arccos\left[\cot(\pi/\sqrt{2})\right]$. 67

表 5.3 **Implementation of outsourcing.** Here $\alpha = \arccos\left[\csc(\pi/\sqrt{2})\sin(\chi/4)\right]$ and $\gamma = \phi - \arccos\left[\cot(\pi/\sqrt{2})\tan(\chi/4)\right]$. 69

表 5.4 **Implementation of R_i.** 73

表 5.5 **Implementation of R_o.** 74

表 5.6 **Implementation of $|1_\mathrm{C}1_\mathrm{X}1_\mathrm{Y}\rangle$ measurement.** Here $|1_\mathrm{C}1_\mathrm{X}1_\mathrm{Y}\rangle \to |0_\mathrm{C}\rangle$ stands for a operation that transforms only $|1_\mathrm{C}1_\mathrm{X}1_\mathrm{Y}\rangle$ to $|0_\mathrm{C}\rangle$, and all other 7 base states to $|1_\mathrm{C}\rangle$. 74

表 A.1 **Vacuum system** 131

表 A.2 **Oven current supply system** 132

表 A.3 **Helical resonator** 132

表 A.4 **Radial trap frequency lock** 132

表 A.5 **High voltage system** 132

表 A.6 **Magnetic system** 133

表 A.7 **399 nm laser system** 133

表 A.8 **370 nm laser system** 133

表 A.9 **739 nm laser frequency cavity lock** 134

表 A.10 **739 nm laser frequency iodine lock** 134

表 A.11 **935 nm laser system** 135

表 A.12 **Imaging system** 135

表 A.13 **Horn system** 135

表 A.14 **Raman system** 136

表 A.15 **Raman laser repetition rate lock** 136

表 A.16 **Individual addressing system** 137

表 A.17 **Control system** 138

公式索引

公式 1-1 …… 1

公式 1-2 …… 1

公式 1-3 …… 2

公式 1-4 …… 2

公式 1-5 …… 2

公式 1-6 …… 2

公式 1-7 …… 3

公式 1-8 …… 5

公式 1-9 …… 5

公式 2-1 …… 7

公式 2-2 …… 7

公式 2-3 …… 8

公式 2-4 …… 8

公式 2-5 …… 8

公式 2-6 …… 8

公式 2-7 …… 8

公式 2-8 …… 9

公式 2-9 …… 9

公式 2-10 …… 9

公式 2-11 …… 9

公式 2-12 …… 9

公式 2-13 …… 9

公式 2-14 …… 9

公式 2-15 …… 9
公式 2-16 …… 10
公式 2-17 …… 10
公式 2-18 …… 10
公式 2-19 …… 10
公式 2-20 …… 10
公式 2-21 …… 10
公式 2-22 …… 10
公式 2-23 …… 10
公式 2-24 …… 11
公式 2-25 …… 11
公式 2-26 …… 11
公式 2-27 …… 11
公式 2-28 …… 11
公式 2-29 …… 12
公式 2-30 …… 12
公式 2-31 …… 12
公式 2-32 …… 12
公式 2-33 …… 12
公式 2-34 …… 13
公式 2-35 …… 13
公式 2-36 …… 13
公式 2-37 …… 13
公式 2-38 …… 13
公式 2-39 …… 14
公式 2-40 …… 15

公式 2-41 ……………………………………………………………………………17
公式 2-42 ……………………………………………………………………………17
公式 2-43 ……………………………………………………………………………18
公式 2-44 ……………………………………………………………………………18
公式 2-45 ……………………………………………………………………………19
公式 2-46 ……………………………………………………………………………19
公式 2-47 ……………………………………………………………………………19
公式 2-48 ……………………………………………………………………………19
公式 2-49 ……………………………………………………………………………19
公式 2-50 ……………………………………………………………………………19
公式 2-51 ……………………………………………………………………………20
公式 2-52 ……………………………………………………………………………20
公式 2-53 ……………………………………………………………………………20
公式 2-54 ……………………………………………………………………………20
公式 2-55 ……………………………………………………………………………20
公式 2-56 ……………………………………………………………………………21
公式 2-57 ……………………………………………………………………………21
公式 2-58 ……………………………………………………………………………21
公式 2-59 ……………………………………………………………………………21
公式 2-60 ……………………………………………………………………………21
公式 2-61 ……………………………………………………………………………22
公式 2-62 ……………………………………………………………………………22
公式 2-63 ……………………………………………………………………………22
公式 2-64 ……………………………………………………………………………23
公式 2-65 ……………………………………………………………………………23
公式 2-66 ……………………………………………………………………………23

公式 2-67 23
公式 2-68 23
公式 2-69 24
公式 2-70 24
公式 3-1 29
公式 3-2 29
公式 3-3 29
公式 3-4 29
公式 3-5 29
公式 3-6 30
公式 3-7 30
公式 3-8 31
公式 3-9 32
公式 3-10 33
公式 3-11 33
公式 3-12 33
公式 3-13 36
公式 3-14 36
公式 3-15 38
公式 3-16 39
公式 3-17 40
公式 3-18 40
公式 4-1 48
公式 4-2 48
公式 4-3 48
公式 4-4 50

公式 4-5 ……50
公式 4-6 ……51
公式 4-7 ……52
公式 4-8 ……52
公式 4-9 ……53
公式 4-10 ……53
公式 4-11 ……53
公式 5-1 ……63
公式 5-2 ……63
公式 5-3 ……63
公式 5-4 ……63
公式 5-5 ……63
公式 5-6 ……65
公式 5-7 ……65
公式 5-8 ……65
公式 5-9 ……65
公式 5-10 ……65
公式 5-11 ……65
公式 5-12 ……65
公式 5-13 ……65
公式 5-14 ……65
公式 5-15 ……66
公式 5-16 ……66
公式 5-17 ……66
公式 5-18 ……66
公式 5-19 ……68

公式 5-20 ……68
公式 5-21 ……70
公式 5-22 ……70
公式 5-23 ……70
公式 5-24 ……70
公式 5-25 ……70
公式 5-26 ……71
公式 5-27 ……71
公式 5-28 ……71
公式 5-29 ……72
公式 5-30 ……75
公式 5-31 ……75
公式 5-32 ……75
公式 6-1 ……80
公式 6-2 ……82
公式 6-3 ……82
公式 6-4 ……82
公式 6-5 ……83
公式 6-6 ……83
公式 6-7 ……83
公式 6-8 ……85
公式 6-9 ……85
公式 6-10 ……85
公式 6-11 ……93
公式 6-12 ……93
公式 6-13 ……94

公式 6-14 94
公式 6-15 94
公式 7-1 95
公式 7-2 96
公式 7-3 97
公式 7-4 97
公式 7-5 97
公式 7-6 100
公式 7-7 100
公式 7-8 100
公式 7-9 101
公式 7-10 101
公式 7-11 101
公式 7-12 101
公式 7-13 101
公式 7-14 103

参考文献

[1] Nielsen M A, Chuang I L. Quantum computation and quantum information: 10th anniversary edition[M]. Cambridge University Press, 2010

[2] Deutsch D, Jozsa R. Rapid solution of problems by quantum computation[J/OL]. Proceedings of the Royal Society of London A: Mathematical, Physical and Engineering Sciences, 1992, 439(1907): 553–558. http://rspa.royalsocietypublishing.org/content/439/1907/553.

[3] Grover L K. Quantum mechanics helps in searching for a needle in a haystack[J/OL]. Phys. Rev. Lett., 1997, 79: 325–328. https://link.aps.org/doi/10.1103/PhysRevLett.79.325.

[4] Shor P. Polynomial-time algorithms for prime factorization and discrete logarithms on a quantum computer[J/OL]. SIAM Review, 1999, 41(2): 303–332. https://doi.org/10.1137/S0036144598347011.

[5] DiVincenzo D P. The physical implementation of quantum computation[J/OL]. Fortschritte der Physik, 48(911): 771–783. https://onlinelibrary.wiley.com/doi/abs/10.1002/1521-3978%28200009%2948%3A9/11%3C771%3A%3AAID-PROP771%3E3.0.CO%3B2-E.

[6] Cirac J I, Zoller P. Quantum computations with cold trapped ions[J/OL]. Phys. Rev. Lett., 1995, 74: 4091–4094. https://link.aps.org/doi/10.1103/PhysRevLett.74.4091.

[7] Balzer C, Braun A, Hannemann T, et al. Electrodynamically trapped yb^+ ions for quantum information processing[J/OL]. Phys. Rev. A, 2006, 73: 041407. https://link.aps.org/doi/10.1103/PhysRevA.73.041407.

[8] Olmschenk S, Younge K C, Moehring D L, et al. Manipulation and detection of a trapped yb^+ hyperfine qubit[J/OL]. Phys. Rev. A, 2007, 76: 052314. https://link.aps.org/doi/10.1103/PhysRevA.76.052314.

[9] Kuan Z, Jiajun M, Xiang Z, et al. Operational effects of the unot gate on classical and quantum correlations[J/OL]. Science Bulletin, 2018, 63(12): 765–770. http://engine.scichina.com/publisher/ScienceChinaPress/journal/ScienceBulletin/63/12/10.1016/j.scib.2018.05.011.

[10] Zhang X, Zhang K, Shen Y, et al. Experimental quantum simulation of fermion-antifermion scattering via boson exchange in a trapped ion[J]. Nature communications, 2018, 9(1): 195.

[11] Paul W. Electromagnetic traps for charged and neutral particles[J/OL]. Rev. Mod. Phys., 1990, 62: 531–540. https://link.aps.org/doi/10.1103/RevModPhys.62.531.

[12] James D. Quantum dynamics of cold trapped ions with application to quantum computation [J/OL]. Applied Physics B, 1998, 66(2): 181–190. https://doi.org/10.1007/s003400050373.

[13] Sakurai J J, Napolitano J. Modern quantum mechanics[M]. 2nd ed. Cambridge University Press, 2017

[14] Foot C J, et al. Atomic physics: volume 7[M]. [S.l.]: Oxford University Press, 2005

[15] Fisk P T H, Sellars M J, Lawn M A, et al. Accurate measurement of the 12.6 ghz "clock" transition in trapped /sup 171/yb/sup +/ ions[J]. IEEE Transactions on Ultrasonics, Ferroelectrics, and Frequency Control, 1997, 44(2): 344–354.

[16] Berkeland D J, Boshier M G. Destabilization of dark states and optical spectroscopy in zeeman-degenerate atomic systems[J/OL]. Phys. Rev. A, 2002, 65: 033413. https://link.aps.org/doi/10.1103/PhysRevA.65.033413.

[17] Leibfried D, Blatt R, Monroe C, et al. Quantum dynamics of single trapped ions[J/OL]. Rev. Mod. Phys., 2003, 75: 281–324. https://link.aps.org/doi/10.1103/RevModPhys.75.281.

[18] Bell A S, Gill P, Klein H A, et al. Laser cooling of trapped ytterbium ions using a four-level optical-excitation scheme[J/OL]. Phys. Rev. A, 1991, 44: R20–R23. https://link.aps.org/doi/10.1103/PhysRevA.44.R20.

[19] James D F, Jerke J. Effective hamiltonian theory and its applications in quantum information [J/OL]. Canadian Journal of Physics, 2007, 85(6): 625–632. https://doi.org/10.1139/p07-060.

[20] Nagourney W G. Quantum electronics for atomic physics and telecommunication[M]. [S.l.]: Oxford University Press, USA, 2014

[21] Gisin N, Popescu S. Spin flips and quantum information for antiparallel spins[J/OL]. Phys. Rev. Lett., 1999, 83: 432–435. http://link.aps.org/doi/10.1103/PhysRevLett.83.432.

[22] Bechmann-Pasquinucci H, Gisin N. Incoherent and coherent eavesdropping in the six-state protocol of quantum cryptography[J/OL]. Phys. Rev. A, 1999, 59: 4238–4248. http://link.aps.org/doi/10.1103/PhysRevA.59.4238.

[23] Bužek V, Hillery M, Werner R F. Optimal manipulations with qubits: Universal-not gate[J/OL]. Phys. Rev. A, 1999, 60: R2626–R2629. http://link.aps.org/doi/10.1103/PhysRevA.60.R2626.

[24] Alvarez-Rodriguez U, Sanz M, Lamata L, et al. The forbidden quantum adder[J]. Scientific reports, 2015, 5: 11983.

[25] De Martini F, Bužek V, Sciarrino F, et al. Experimental realization of the quantum universal not gate[J]. Nature, 2002, 419(6909): 815–818.

[26] Ricci M, Sciarrino F, Sias C, et al. Teleportation scheme implementing the universal optimal quantum cloning machine and the universal not gate[J/OL]. Phys. Rev. Lett., 2004, 92: 047901. http://link.aps.org/doi/10.1103/PhysRevLett.92.047901.

[27] Scarani V, Iblisdir S, Gisin N, et al. Quantum cloning[J/OL]. Rev. Mod. Phys., 2005, 77: 1225–1256. http://link.aps.org/doi/10.1103/RevModPhys.77.1225.

[28] Ollivier H, Zurek W H. Quantum discord: A measure of the quantumness of correlations[J/OL]. Phys. Rev. Lett., 2001, 88: 017901. http://link.aps.org/doi/10.1103/PhysRevLett.88.017901.

[29] Henderson L, Vedral V. Classical, quantum and total correlations[J/OL]. Journal of Physics A: Mathematical and General, 2001, 34(35): 6899. http://stacks.iop.org/0305-4470/34/i=35/a=315.

[30] Gu M, Chrzanowski H M, Assad S M, et al. Observing the operational significance of discord consumption[J]. Nature Physics, 2012, 8(9): 671–675.

[31] Casanova J, Sabín C, León J, et al. Quantum simulation of the majorana equation and unphysical operations[J/OL]. Phys. Rev. X, 2011, 1: 021018. http://link.aps.org/doi/10.1103/PhysRevX.1.021018.

[32] Zhang X, Shen Y, Zhang J, et al. Time reversal and charge conjugation in an embedding quantum simulator[J]. Nature communications, 2015, 6: 7917.

[33] Cover T M, Thomas J A. Elements of information theory[M]. [S.l.]: John Wiley & Sons, 2012

[34] Wang Z, Zhang C, Huang Y F, et al. Experimental verification of genuine multipartite entanglement without shared reference frames[J/OL]. Science Bulletin, 2016, 61(9): 714–719. https://doi.org/10.1007/s11434-016-1063-5.

[35] Jin F, Chen H, Rong X, et al. Experimental simulation of the unruh effect on an nmr quantum simulator[J/OL]. Science China Physics, Mechanics & Astronomy, 2016, 59(3): 630302. https://doi.org/10.1007/s11433-016-5779-7.

[36] Zhao M, Ma T, Zhang T, et al. von neumann measurement-related matrices and the nullity condition for quantum correlation[J/OL]. Science China Physics, Mechanics & Astronomy, 2016, 59(12): 120313. https://doi.org/10.1007/s11433-016-0356-2.

[37] Shen Y, Zhang X, Zhang S, et al. Quantum implementation of the unitary coupled cluster for simulating molecular electronic structure[J/OL]. Phys. Rev. A, 2017, 95: 020501. http://link.aps.org/doi/10.1103/PhysRevA.95.020501.

[38] Shen C, Duan L M. Correcting detection errors in quantum state engineering through data processing[J/OL]. New Journal of Physics, 2012, 14(5): 053053. http://stacks.iop.org/1367-2630/14/i=5/a=053053.

[39] Gulde S, Riebe M, Lancaster G P, et al. Implementation of the deutsch–jozsa algorithm on an ion-trap quantum computer[J]. Nature, 2003, 421(6918): 48.

[40] Monz T, Kim K, Hänsel W, et al. Realization of the quantum toffoli gate with trapped ions[J/OL]. Phys. Rev. Lett., 2009, 102: 040501. http://link.aps.org/doi/10.1103/PhysRevLett.102.040501.

[41] Zhang J, Um M, Lv D, et al. Experimental Preparation of High NOON States for Phonons[J]. ArXiv e-prints, 2016.

[42] Holevo A S. Bounds for the quantity of information transmitted by a quantum communication channel[J]. Problemy Peredachi Informatsii, 1973, 9(3): 3–11.

[43] Modi K. A pedagogical overview of quantum discord[J/OL]. Open Systems & Information Dynamics, 2014, 21(01n02): 1440006. http://www.worldscientific.com/doi/abs/10.1142/S123016121440006X.

[44] Weedbrook C, Pirandola S, Thompson J, et al. How discord underlies the noise resilience of quantum illumination[J/OL]. New Journal of Physics, 2016, 18(4): 043027. http://stacks.iop.org/1367-2630/18/i=4/a=043027.

[45] Niset J, Acín A, Andersen U L, et al. Superiority of entangled measurements over all local strategies for the estimation of product coherent states[J/OL]. Phys. Rev. Lett., 2007, 98: 260404. https://link.aps.org/doi/10.1103/PhysRevLett.98.260404.

[46] Knill E, Laflamme R. Power of one bit of quantum information[J/OL]. Phys. Rev. Lett., 1998, 81: 5672–5675. https://link.aps.org/doi/10.1103/PhysRevLett.81.5672.

[47] Datta A, Flammia S T, Caves C M. Entanglement and the power of one qubit[J/OL]. Phys. Rev. A, 2005, 72: 042316. https://link.aps.org/doi/10.1103/PhysRevA.72.042316.

[48] Araújo M, Feix A, Costa F, et al. Quantum circuits cannot control unknown operations [J/OL]. New Journal of Physics, 2014, 16(9): 093026. http://stacks.iop.org/1367-2630/16/i=9/a=093026.

[49] Friis N, Dunjko V, Dür W, et al. Implementing quantum control for unknown subroutines[J/OL]. Phys. Rev. A, 2014, 89: 030303. https://link.aps.org/doi/10.1103/PhysRevA.89.030303.

[50] Thompson J, Modi K, Vedral V, et al. Quantum plug n’play: modular computation in the quantum regime[J/OL]. New Journal of Physics, 2018, 20(1): 013004. http://stacks.iop.org/1367-2630/20/i=1/a=013004.

[51] Patel R B, Ho J, Ferreyrol F, et al. A quantum fredkin gate[J/OL]. Science Advances, 2016, 2(3). http://advances.sciencemag.org/content/2/3/e1501531.

[52] Lau H K, Plenio M B. Universal quantum computing with arbitrary continuous-variable encoding[J/OL]. Phys. Rev. Lett., 2016, 117: 100501. https://link.aps.org/doi/10.1103/PhysRevLett.117.100501.

[53] Feynman R P. Simulating physics with computers[J]. International journal of theoretical physics, 1982, 21(6-7): 467–488.

[54] Lloyd S. Universal quantum simulators[J/OL]. Science, 1996, 273(5278): 1073–1078. http://www.jstor.org/stable/2899535.

[55] Cirac J I, Zoller P. Goals and opportunities in quantum simulation[J]. Nature Physics, 2012, 8(4): 264.

[56] Georgescu I M, Ashhab S, Nori F. Quantum simulation[J/OL]. Rev. Mod. Phys., 2014, 86: 153–185. https://link.aps.org/doi/10.1103/RevModPhys.86.153.

[57] Leibfried D, DeMarco B, Meyer V, et al. Trapped-ion quantum simulator: Experimental application to nonlinear interferometers[J/OL]. Phys. Rev. Lett., 2002, 89: 247901. https://link.aps.org/doi/10.1103/PhysRevLett.89.247901.

[58] Friedenauer A, Schmitz H, Glueckert J T, et al. Simulating a quantum magnet with trapped ions[J]. Nature Physics, 2008, 4(10): 757.

[59] Kim K, Chang M S, Korenblit S, et al. Quantum simulation of frustrated ising spins with trapped ions[J]. Nature, 2010, 465(7298): 590.

[60] Lanyon B P, Hempel C, Nigg D, et al. Universal digital quantum simulation with trapped ions[J/OL]. Science, 2011, 334(6052): 57–61. http://science.sciencemag.org/content/334/6052/57.

[61] Barends R, Shabani A, Lamata L, et al. Digitized adiabatic quantum computing with a superconducting circuit[J]. Nature, 2016, 534(7606): 222.

[62] Lamata L, León J, Schätz T, et al. Dirac equation and quantum relativistic effects in a single trapped ion[J/OL]. Phys. Rev. Lett., 2007, 98: 253005. https://link.aps.org/doi/10.1103/PhysRevLett.98.253005.

[63] Gerritsma R, Kirchmair G, Zähringer F, et al. Quantum simulation of the dirac equation[J]. Nature, 2010, 463(7277): 68.

[64] Casanova J, García-Ripoll J J, Gerritsma R, et al. Klein tunneling and dirac potentials in trapped ions[J/OL]. Phys. Rev. A, 2010, 82: 020101. https://link.aps.org/doi/10.1103/PhysRevA.82.020101.

[65] Gerritsma R, Lanyon B P, Kirchmair G, et al. Quantum simulation of the klein paradox with trapped ions[J/OL]. Phys. Rev. Lett., 2011, 106: 060503. https://link.aps.org/doi/10.1103/PhysRevLett.106.060503.

[66] Loredo J C, Almeida M P, Di Candia R, et al. Measuring entanglement in a photonic embedding quantum simulator[J/OL]. Phys. Rev. Lett., 2016, 116: 070503. https://link.aps.org/doi/10.1103/PhysRevLett.116.070503.

[67] Chen M C, Wu D, Su Z E, et al. Efficient measurement of multiparticle entanglement with embedding quantum simulator[J/OL]. Phys. Rev. Lett., 2016, 116: 070502. https://link.aps.org/doi/10.1103/PhysRevLett.116.070502.

[68] Di Candia R, Mejia B, Castillo H, et al. Embedding quantum simulators for quantum computation of entanglement[J/OL]. Phys. Rev. Lett., 2013, 111: 240502. https://link.aps.org/doi/10.1103/PhysRevLett.111.240502.

[69] García-Álvarez L, Casanova J, Mezzacapo A, et al. Fermion-fermion scattering in quantum field theory with superconducting circuits[J/OL]. Phys. Rev. Lett., 2015, 114: 070502. https://link.aps.org/doi/10.1103/PhysRevLett.114.070502.

[70] Barends R, Lamata L, Kelly J, et al. Digital quantum simulation of fermionic models with a superconducting circuit[J]. Nature communications, 2015, 6: 7654.

[71] Martinez E A, Muschik C A, Schindler P, et al. Real-time dynamics of lattice gauge theories with a few-qubit quantum computer[J]. Nature, 2016, 534(7608): 516–519.

[72] Peskin M E, Schroeder D V. An introduction to quantum field theory (frontiers in physics)[M]. [S.l.]: Westview Press Incorporated, 1995

[73] Casanova J, Lamata L, Egusquiza I L, et al. Quantum simulation of quantum field theories in trapped ions[J/OL]. Phys. Rev. Lett., 2011, 107: 260501. https://link.aps.org/doi/10.1103/PhysRevLett.107.260501.

[74] Casanova J, Mezzacapo A, Lamata L, et al. Quantum simulation of interacting fermion lattice models in trapped ions[J/OL]. Phys. Rev. Lett., 2012, 108: 190502. https://link.aps.org/doi/10.1103/PhysRevLett.108.190502.

[75] Mezzacapo A, Las Heras U, Pedernales J, et al. Digital quantum rabi and dicke models in superconducting circuits[J]. Scientific reports, 2014, 4: 7482.

[76] Arrazola I, Pedernales J S, Lamata L, et al. Digital-analog quantum simulation of spin models in trapped ions[J]. Scientific reports, 2016, 6: 30534.

[77] Lamata L. Digital-analog quantum simulation of generalized dicke models with superconducting circuits[J]. Scientific reports, 2017, 7: 43768.

[78] Jordan S P, Lee K S M, Preskill J. Quantum algorithms for quantum field theories[J/OL]. Science, 2012, 336(6085): 1130–1133. http://science.sciencemag.org/content/336/6085/1130.

[79] Monroe C, Meekhof D M, King B E, et al. Resolved-sideband raman cooling of a bound atom to the 3d zero-point energy[J/OL]. Phys. Rev. Lett., 1995, 75: 4011–4014. https://link.aps.org/doi/10.1103/PhysRevLett.75.4011.

[80] Roos C, Zeiger T, Rohde H, et al. Quantum state engineering on an optical transition and decoherence in a paul trap[J/OL]. Phys. Rev. Lett., 1999, 83: 4713–4716. https://link.aps.org/doi/10.1103/PhysRevLett.83.4713.

[81] King B E, Wood C S, Myatt C J, et al. Cooling the collective motion of trapped ions to initialize a quantum register[J/OL]. Phys. Rev. Lett., 1998, 81: 1525–1528. https://link.aps.org/doi/10.1103/PhysRevLett.81.1525.

[82] Diddams S A, Diels J C, Atherton B. Differential intracavity phase spectroscopy and its application to a three-level system in samarium[J/OL]. Phys. Rev. A, 1998, 58: 2252–2264. https://link.aps.org/doi/10.1103/PhysRevA.58.2252.

[83] Heinzen D J, Wineland D J. Quantum-limited cooling and detection of radio-frequency oscillations by laser-cooled ions[J/OL]. Phys. Rev. A, 1990, 42: 2977–2994. https://link.aps.org/doi/10.1103/PhysRevA.42.2977.

[84] Monroe C, Meekhof D M, King B E, et al. Demonstration of a fundamental quantum logic gate [J/OL]. Phys. Rev. Lett., 1995, 75: 4714–4717. https://link.aps.org/doi/10.1103/PhysRevLett.75.4714.

[85] Shen Y, Lu Y, Zhang K, et al. Quantum optical emulation of molecular vibronic spectroscopy using a trapped-ion device[J/OL]. Chem. Sci., 2018, 9: 836–840. http://dx.doi.org/10.1039/C7SC04602B.

[86] Mezzacapo A, Casanova J, Lamata L, et al. Digital quantum simulation of the holstein model in trapped ions[J/OL]. Phys. Rev. Lett., 2012, 109: 200501. https://link.aps.org/doi/10.1103/PhysRevLett.109.200501.

[87] Porras D, Cirac J I. Effective quantum spin systems with trapped ions[J/OL]. Phys. Rev. Lett., 2004, 92: 207901. https://link.aps.org/doi/10.1103/PhysRevLett.92.207901.

[88] Kim K, Roos C F, Aolita L, et al. Geometric phase gate on an optical transition for ion trap quantum computation[J/OL]. Phys. Rev. A, 2008, 77: 050303. https://link.aps.org/doi/10.1103/PhysRevA.77.050303.

[89] Kim K, Chang M S, Islam R, et al. Entanglement and tunable spin-spin couplings between trapped ions using multiple transverse modes[J/OL]. Phys. Rev. Lett., 2009, 103: 120502. https://link.aps.org/doi/10.1103/PhysRevLett.103.120502.

[90] Hague J P, MacCormick C. Bilayers of rydberg atoms as a quantum simulator for unconventional superconductors[J/OL]. Phys. Rev. Lett., 2012, 109: 223001. https://link.aps.org/doi/10.1103/PhysRevLett.109.223001.

[91] Stojanović V M, Shi T, Bruder C, et al. Quantum simulation of small-polaron formation with trapped ions[J/OL]. Phys. Rev. Lett., 2012, 109: 250501. https://link.aps.org/doi/10.1103/PhysRevLett.109.250501.

[92] Boixo S, Isakov S V, Smelyanskiy V N, et al. Characterizing Quantum Supremacy in Near-Term Devices[J]. ArXiv e-prints, 2016.

[93] Pednault E, Gunnels J A, Nannicini G, et al. Breaking the 49-Qubit Barrier in the Simulation of Quantum Circuits[J]. ArXiv e-prints, 2017.

[94] An S, Zhang J N, Um M, et al. Experimental test of the quantum jarzynski equality with a trapped-ion system[J]. Nature Physics, 2015, 11(2): 193.

[95] Um M, Zhang J, Lv D, et al. Phonon arithmetic in a trapped ion system[J]. Nature communications, 2016, 7: 11410.

[96] Lv D, An S, Um M, et al. Reconstruction of the jaynes-cummings field state of ionic motion in a harmonic trap[J/OL]. Phys. Rev. A, 2017, 95: 043813. https://link.aps.org/doi/10.1103/PhysRevA.95.043813.

[97] Itano W M, Bergquist J C, Bollinger J J, et al. Quantum projection noise: Population fluctuations in two-level systems[J/OL]. Phys. Rev. A, 1993, 47: 3554–3570. https://link.aps.org/doi/10.1103/PhysRevA.47.3554.

[98] Meekhof D M, Monroe C, King B E, et al. Generation of nonclassical motional states of a trapped atom[J/OL]. Phys. Rev. Lett., 1996, 76: 1796–1799. https://link.aps.org/doi/10.1103/PhysRevLett.76.1796.

[99] Mølmer K, Sørensen A. Multiparticle entanglement of hot trapped ions[J/OL]. Phys. Rev. Lett., 1999, 82: 1835–1838. https://link.aps.org/doi/10.1103/PhysRevLett.82.1835.

[100] Monz T, Schindler P, Barreiro J T, et al. 14-qubit entanglement: Creation and coherence[J/OL]. Phys. Rev. Lett., 2011, 106: 130506. https://link.aps.org/doi/10.1103/PhysRevLett.106.130506.

[101] Zhu S L, Monroe C, Duan L M. Arbitrary-speed quantum gates within large ion crystals through minimum control of laser beams[J/OL]. EPL (Europhysics Letters), 2006, 73(4): 485. http://stacks.iop.org/0295-5075/73/i=4/a=485.

[102] Zhu S L, Monroe C, Duan L M. Trapped ion quantum computation with transverse phonon modes[J/OL]. Phys. Rev. Lett., 2006, 97: 050505. https://link.aps.org/doi/10.1103/PhysRevLett.97.050505.

[103] Choi T, Debnath S, Manning T A, et al. Optimal quantum control of multimode couplings between trapped ion qubits for scalable entanglement[J/OL]. Phys. Rev. Lett., 2014, 112: 190502. https://link.aps.org/doi/10.1103/PhysRevLett.112.190502.

[104] Debnath S, Linke N M, Figgatt C, et al. Demonstration of a small programmable quantum computer with atomic qubits[J]. Nature, 2016, 536(7614): 63.

[105] Johnson K G, Wong-Campos J D, Restelli A, et al. Active stabilization of ion trap radiofrequency potentials[J/OL]. Review of Scientific Instruments, 2016, 87(5): 053110. https://doi.org/10.1063/1.4948734.

[106] Chew A. Doppler-free spectroscopy of iodine at 739nm[J]. undergraduate thesis, University of Maryland, 2008.

致 谢

衷心感谢导师 Kihwan Kim 副教授对本人的精心指导。初进实验室时，Kihwan 教会了我很多实验技巧，并帮助我入门科研。论文写作、口头报告和海报制作曾经是我的弱项，Kihwan 在这些方面授予了我大量的鱼和渔。在他的熏陶下，这些方面渐渐已不是我的短板，甚至成为强项。通过与 Kihwan 长时间的交流，我的英语口语也大有提升。

感谢理论合作者 Jayne Thompson 和 Mile Gu 在论文写作过程中，对我精神和实质上的帮助。感谢我的战友：汪野、张君华、沈杨超、张帅宁、路尧和陈文涛。他们与我并肩作战，共同建设实验平台。他们为实验室作出了不可磨灭的贡献。

尤其感谢师兄张翔。在我做首个项目时，是他带我了解实验硬件设备的点点滴滴，并为我提供了实验所需的软件。在他的熏陶下，我也成长为一代 Mathematica 大师，并在他毕业后接替他编写实验室软件。在他的主导下，我们还合作完成了一个量子模拟的实验，并以共同一作的名义发表了高质量的论文。

感谢 ThuThesis，它的存在让我的论文写作轻松自在了许多，让我的论文格式规整漂亮了许多。

声 明

本人郑重声明：所呈交的学位论文，是本人在导师指导下，独立进行研究工作所取得的成果。尽我所知，除文中已经注明引用的内容外，本学位论文的研究成果不包含任何他人享有著作权的内容。对本论文所涉及的研究工作做出贡献的其他个人和集体，均已在文中以明确方式标明。

签 名：____________ 日 期：____________

附录 A Hardwares of a trapped ion system

A.1 Vacuum system

表 A.1 **Vacuum system**

Name	Purpose	Brand	Model
Ion Pump	Pump ions	Agilent	VacIon Plus 20
Ion Pump Controller	Control Ion Pump	Agilent	4UHV
Titanium Sublimation Pump	Pump hydrogen molecules	Lesker	
Vacuum Chamber	Contain trap and ovens	KPI	MCF450-SphOct-E2A8
Trap	Trap ions		Designed by Shuaining Zhang
Oven 171	Provide ^{171}Yb atoms		
Oven 174	Provide ^{174}Yb atoms		

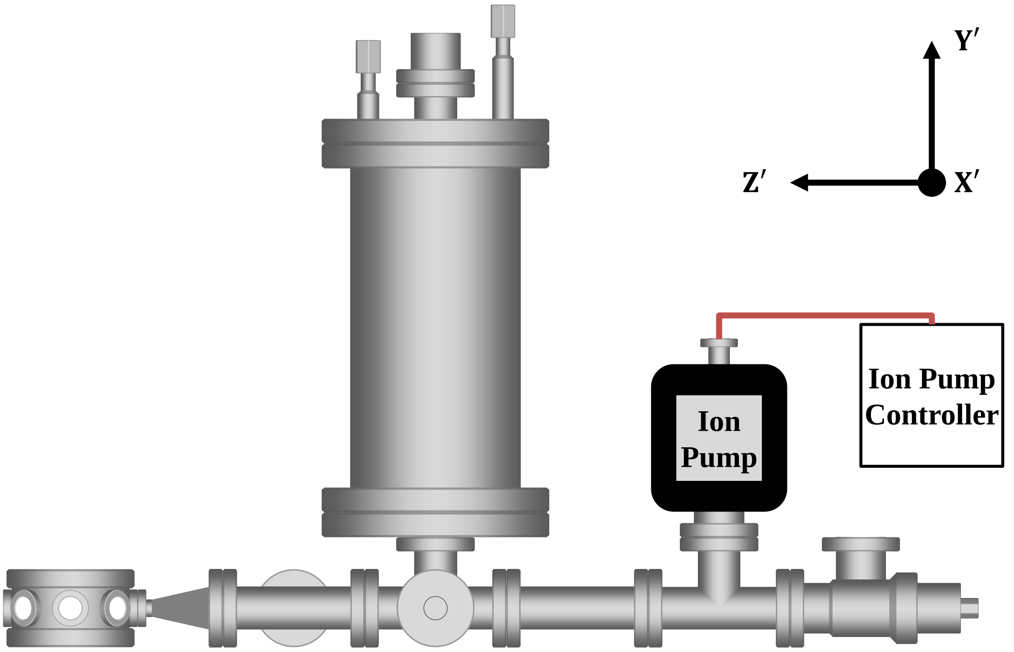

图 A.1 **Vacuum system**

A.2　Oven current supply system

表 A.2　**Oven current supply system**

Name	Purpose	Brand	Model
DC Power Supply 0	Supply power for Oven 171/174	Agilent	E3632A

A.3　Radio frequency (RF) system

A.3.1　Helical resonator

表 A.3　**Helical resonator**

Name	Purpose	Brand	Model
Helical Resonator	Amplify RF power	Homemade	
Dual Directional Coupler	Couple RF signal to Helical Resonator	上海华湘	DDTO-1-30B
Power Meter	Measure RF transmission power	Diamond	SX-200

A.3.2　Radial trap frequency lock

表 A.4　**Radial trap frequency lock**

Name	Purpose	Brand	Model
Signal Generator RF	Generate 20.9 MHz, -10.8 dBm RF signal	R&S	SMB100A
Mixer RF	Modulate RF power	Mini-Circuits	ZAD-1-1+
Amplifier RF	Amplify RF power	Mini-Circuits	ZHL-5W-1
Rectifier	Convert RF to DC		SHX-803-S-4G
PID RF	Stabilize RF power	Newport	LB1005-S

See Ref.[105].

A.4　High voltage system

表 A.5　**High voltage system**

Name	Purpose	Brand	Model
High Voltage Power Supply	Supply DC power for Trap	W-Ie-Ne-R	Mpod-Minicrate HV/LV
Low Pass Filters	Filter DC signals	中发	Designed by Kuan Zhang

A.5 Magnetic system

表 A.6　**Magnetic system**

Name	Purpose	Brand	Model
Coil-pair 1	Provide horizontal magnetic field	Homemade	
Coil-pair 2	Provide horizontal magnetic field	Homemade	
Coil-pair 3	Provide vertical magnetic field	Homemade	
DC Power Supply 1	Supply power for Coil-pair 1	Agilent	E3614A
DC Power Supply 2	Supply power for Coil-pair 2	Agilent	E3614A
DC Power Supply 3	Supply power for Coil-pair 3	Agilent	U8001A

A.6 399 nm laser system

表 A.7　**399 nm laser system**

Name	Purpose	Brand	Model
Laser 399	Provide 399 nm CW laser	Toptica	DL pro
Laser Controller 399	Control Laser 399	Toptica	DLC pro
Dichroic Mirror 399/370	Reflect 399 nm laser and transmit 370 nm laser	Thorlabs	

A.7 370 nm laser system

表 A.8　**370 nm laser system**

Name	Purpose	Brand	Model
Laser 739/370	Provide 739 nm and 370 nm CW laser	Toptica	TA-SHG pro
Lens 370	Focus 399 nm and 370 nm laser		
Stage 370	Provide XYZ travel for Lens 370	Newport	M-461-XYZ-M
AOM D	Turn on/off detection beam	Brimrose	
AOM P	Turn on/off optical pumping beam	Brimrose	
AOM C	Turn on/off Doppler cooling beam	Brimrose	
EOM P	Add sideband for optical pumping beam	New Focus	4431
EOM C	Add sideband for Doppler cooling beam	Qubig	EO-WG14.7M2
Amplifier D	Amplify signal for AOM D	Mini-Circuits	ZHL-03-5WF+
Amplifier P	Amplify signal for AOM P	Mini-Circuits	ZHL-03-5WF+
Amplifier C	Amplify signal for AOM C	Mini-Circuits	ZHL-03-5WF+
Amplifier P1	Amplify signal for EOM P	Mini-Circuits	ZHL-5W-2G-S+
Amplifier C1	Amplify signal for EOM C	Microsemi	L0707-38-T629
Signal Generator C1	Generate 14.7478 GHz, 4 dBm signal for EOM C	Keysight	N5183B

A.8　739 nm laser system

A.8.1　739 nm laser frequency cavity lock

表 A.9　**739 nm laser frequency cavity lock**

Name	Purpose	Brand	Model
Cavity 739	Provide frequency standard	Homemade	Designed by Yao Lu
PD 739	Detect signal of Cavity 739	Thorlabs	PDA10A-EC
PDD 739	Process error signal	Toptica	PDD 110
PID 739	Lock 739 nm laser frequency to Cavity 739	中发	

A.8.2　739 nm laser frequency iodine lock

表 A.10　**739 nm laser frequency iodine lock**

Name	Purpose	Brand	Model
Iodine	Provide frequency standard		
EOM I	Add sideband for iodine lock		EOSpace
AOM I	Generate pump beam	Crystal Technology	3080-122
PD I	Detect probe beam power to reference beam	New Focus	2007
Amplifier I	Amplify signal for AOM I	Mini-Circuits	ZHL-03-5WF+
Amplifier I1	Amplify signal for EOM I	Mini-Circuits	ZVA-183-S+
VCO I	Scan the frequency of AOM I	Mini-Circuits	ZX95-100-S+
Signal Generator I	Generate 15.5 kHz, 4 V-6 V for VCO I	Tektronix	AFG3102C
Lock-in Amplifier I	Measure phase of PD I to Signal Generator I	SRS	SR510
PID I	Lock length of Cavity 739 to Iodine	中发	
HV I	Amplify DC signal of PID I for Cavity 739	中发	

See Ref.[106].

A.9　935 nm laser system

表 A.11　**935 nm laser system**

Name	Purpose	Brand	Model
Laser 935	Provide 935 nm CW laser	Toptica	DL pro
Lens 935	Focus 935 nm laser		
Stage 935	Provide XYZ travel for Lens 935	Newport	M-461-XYZ-M
EOM 935	Add sideband for 935 nm laser		EOSpace
Amplifier 935	Amplify signal for EOM 935	Mini-Circuits	ZVA-183-S+

A.10　Imaging system

表 A.12　**Imaging system**

Name	Purpose	Brand	Model
Lens M	Image ions	Photon Gear	
Stage M	Provide XYZ travel for Lens M	Newport	M-562-XYZ-LH
Stage PMT	Provide XYZ travel for PMT	Newport	M-561D-XYZ-LH
Actuator M	Provide vertical travel for Lens M	Newport	TRB12CC
BPF M	Filter 370 nm fluorescence	Semrock	FF01-356/30-25
Flip Mirror M	Reflect for Camara and transmit for PMT	Newport	9891-M

A.11　Horn system

表 A.13　**Horn system**

Name	Purpose	Brand	Model
Horn	Generate microwave for ions	Ainfomw	LB-62-15-C-SF
Signal Generator H	Generate 12.462812 GHz, 8 dBm signal	R&S	SMB100A
Mixer H	Mix AWG signal to Signal Generator H	Mini-Circuits	ZX05-153-S+
Amplifier H0	Amplify signal for Horn	Mini-Circuits	ZX60-14012L-S+
Amplifier H	Amplify signal for Horn	Mini-Circuits	LZY-22+

A.12 Raman system

表 A.14 **Raman system**

Name	Purpose	Brand	Model
Laser R	Provide 375 nm pulse-laser	Coherent	Mira-HP
Lens R0	Focus global beam in horizontal direction		
Lens R	Focus global beam		
Stage R	Provide XYZ travel for Lens R	Newport	M-461-XYZ-LH-M
AOM R	Turn on/off global beam	Brimrose	
Amplifier -1	Amplify signal for AOM R	Mini-Circuits	ZHL-03-5WF+

A.12.1 Raman laser repetition rate lock

表 A.15 **Raman laser repetition rate lock**

Name	Purpose	Brand	Model
Signal Generator R	Generate 6.311906 GHz, 0 dBm signal	R&S	SMB100A
PD R	Detect the envelope of Raman laser	EOT	ET-4000
BPF R	Filter signal of PD R	Coleman Microwave	140-0523-001
Amplifier R0	Amplify output of BPF R	Mini-Circuits	ZVA-183-S+
Amplifier R	Amplify output of BPF R	Mini-Circuits	ZVE-3W-183+
Mixer R	Mix 6 G sideband to reference	Mini-Circuits	ZMX-7GR
LPF R	Filter output of Mixer R	Mini-Circuits	SLP-1.9+
PID R	Stabilize Raman laser repetition rate	Newport	LB1005-S

A.13　Individual addressing system

表 A.16　**Individual addressing system**

Name	Purpose	Brand	Model
Beam Splitter	Split 1 Raman beam into 5	Holoor	
Lens A	Focus addressing beams	Wavelength	355nmFL47Q
Stage A	Provide XYZ travel for Lens A	Newport	M-562-XYZ
Actuator A1	Provide horizontal travel for Lens A	Thorlabs	PIA13
Actuator A2	Provide horizontal travel for Lens A	Thorlabs	PIA13
Actuator A3	Provide vertical travel for Lens A	Thorlabs	PIA13
AOM A	Turn on/off addressing beams	Gooch & Housego	AOMC 220-5
Splitter 0	Combine DDS and AWG signals	Mini-Circuits	ZFSC-2-1-75+
Splitter 1	Combine DDS and AWG signals	Mini-Circuits	ZFSC-2-1-75+
Splitter 2	Combine DDS and AWG signals	Mini-Circuits	ZFSC-2-1-75+
Splitter 3	Combine DDS and AWG signals	Mini-Circuits	ZFSC-2-1-75+
Splitter 4	Combine DDS and AWG signals	Mini-Circuits	ZFSC-2-1-75+
Amplifier 0	Amplify signal for AOM A	Mini-Circuits	ZHL-03-5WF+
Amplifier 1	Amplify signal for AOM A	Mini-Circuits	ZHL-03-5WF+
Amplifier 2	Amplify signal for AOM A	Mini-Circuits	ZHL-03-5WF+
Amplifier 3	Amplify signal for AOM A	Mini-Circuits	ZHL-03-5WF+
Amplifier 4	Amplify signal for AOM A	Mini-Circuits	ZHL-03-5WF+

A.14　Control system

表 A.17　**Control system**

Name	Purpose	Brand	Model
Sequencer	Generate timing sequence	Homemade	
Switch Box	Turn on/off/TTL for signals	Mini-Circuits	ZASW-2-50DR+
Signal Generator C	Generate 200 MHz, -7 dBm for AOM C	南京盛普	SP2461
Signal Generator P	Generate 220 MHz, -20 dBm for AOM P	南京盛普	SP1461
Signal Generator D	Generate 220 MHz, -22 dBm for AOM D	南京盛普	SP1461
Lab Brick I	Generate 13.277 GHz, -7 dBm for EOM P	Vaunix	LMS-602
Lab Brick P	Generate 2.105 GHz, -8.5 dBm for EOM P	Vaunix	LSG-402
Lab Brick 935	Generate 3.0695 GHz, -19.5 dBm for EOM I	Vaunix	LSG-402
DDS -1	Generate signal for AOM R	Analog Device	AD9910
DDS 0	Generate signal for AOM A	Analog Device	AD9910
DDS 1	Generate signal for AOM A	Analog Device	AD9910
DDS 2	Generate signal for AOM A	Analog Device	AD9910
DDS 3	Generate signal for AOM A	Analog Device	AD9910
DDS 4	Generate signal for AOM A	Analog Device	AD9910
AWG	Generate signal for AOM A and Horn	Spectrum	DN2.662-08
PMT	Collect data	Hamamatsu	H10682-210
Camara	Collect data	Andor	iXon Ultra

个人简历、在学期间发表的学术论文与研究成果

个人简历

1991 年 8 月 28 日出生于湖北省武汉市。

2009 年 9 月考入清华大学物理系物理学专业，2013 年 7 月本科毕业并获得理学学士学位。

2013 年 9 月免试进入清华大学大学交叉信息研究院攻读理学博士学位至今。

发表的学术论文

[1] Kuan Zhang, Jiajun Ma, Xiang Zhang, Jayne Thompson, Vlatko Vedral, Kihwan Kim, Mile Gu. Operational effects of the UNOT gate on classical and quantum correlations. Science Bulletin, 2018, 63(12):765-770.

[2] Xiang Zhang, Kuan Zhang, Yangchao Shen, Shuaining Zhang, Jing-Ning Zhang, Man-Hong Yung, Jorge Casanova, Julen S. Pedernales, Lucas Lamata, Enrique Solano, Kihwan Kim. Experimental quantum simulation of fermion-antifermion scattering via boson exchange in a trapped ion. Nature Communications, 2018, 9(1):195.

[3] Yangchao Shen, Yao Lu, Kuan Zhang, Junhua Zhang, Shuaining Zhang, Joonsuk Huh, Kihwan Kim. Quantum optical emulation of molecular vibronic spectroscopy using a trapped-ion device. Chemical Science, 2018, 9(4):836-840.

[4] Jiyong Park, Yao Lu, Jaehak Lee, Yangchao Shen, Kuan Zhang, Shuaining Zhang, Muhammad Suhail Zubairy, Kihwan Kim, Hyunchul Nha. Revealing nonclassicality beyond Gaussian states via a single marginal distribution. Proceedings of the National Academy of Sciences of the United States of America, 2017, 114(5):891-896.